EFFECTS OF RED BLOOD CELLS AND SHEAR RATE ON THROMBUS GROWTH

A Thesis
Presented to
The Academic Faculty

by

Marmar Mehrabadi

In Partial Fulfillment
of the Requirements for the Degree
Doctor of Philosophy in the
School of Mechanical Engineering

Georgia Institute of Technology
December 2014

EFFECTS OF RED BLOOD CELLS AND SHEAR RATE ON THROMBUS GROWTH

Approved by:

Professor David N. Ku, Advisor
School of Mechanical Engineering
Georgia Institute of Technology

Professor Cyrus K. Aidun, Advisor
School of Mechanical Engineering
Georgia Institute of Technology

Professor S. Mostafa Ghiaasiaan
School of Mechanical Engineering
Georgia Institute of Technology

Professor Julie A. Champion
School of Chemical & Biomolecular Engineering
Georgia Institute of Technology

Professor Kenichi Tanaka
Department of Anesthesiology
University of Pittsburgh

Date Approved: 14 Novermber 2014

ACKNOWLEDGEMENTS

I would like to express my gratitude to my co-advisor, Dr. David Ku, for his outstanding knowledge, support, guidance, and patience. I will always be grateful for having the opportunity to learn from someone I respect so greatly. I am also grateful to my co-advisor, Dr. Cyrus Aidun, for his wisdom, guidance, support and for giving me the freedom to explore on my own. I would also like to thank my thesis committee members for their valuable time and suggestions.

I would also like to thank my first advisor at Georgia Tech, Dr. Andrei Fedorov, for his knowledge, many valuable discussions, and his continuous support. Special thanks go to Dr. Peter Kottke for his outstanding knowledge, and for his friendship and great advices whenever needed.

I am grateful for the support of my friends and colleagues that I had the opportunity to work with while at Georgia Tech. These include members of Dr. Aidun's lab, Dr. Fedorov's lab and Dr. Ku's lab. Special acknowledgments also go to Lauren Casa, Susan Hastings, Jane Kang, Andrea Para, Daniel Reasor, B. Min Yun, for fruitful discussions, and for their support and friendship. Additionally, I'd like to thank past and present members of Wing 2A, especially Gregory Holst, Melissa Li, Jaeho Oh, Christopher Phaneuf and Swetha Rathan.

I would like to thank the National Science Foundation's support through Extreme Science and Engineering Discovery Environment (XSEDE).

Finally, I would like to thank my family for their unconditional love, encouragement, and support during my studies.

TABLE OF CONTENTS

LIST OF TABLES

LIST OF FIGURES

SUMMARY

Thrombosis formation upon rupture or erosion of an atherosclerotic plaque can lead to occlusion of arteries. An occlusive thrombus is the most common cause of clinical events such as angina, myocardial infarction, ischemic attacks and strokes. Occlusive thrombi can cause ischemic cardiac arrest in less than an hour. Thrombosis formation requires rapid platelet accumulation rates exceeding thrombosis lysis and embolization rates. Hemodynamics greatly affects platelet accumulation rate through affecting platelet transport to the surface of a growing thrombus. The presence of red blood cells (RBCs) in blood increases platelet transport rate by several orders of magnitude compared to transport due to Brownian motion. Margination of platelets towards the vessel walls also results in higher platelet concentration at the RBC-depleted layer relative to the bulk. In this thesis, we studied the effects of hemodynamics on thrombus growth. We investigated the effects of important flow and particle properties on margination of particles in RBC suspensions by direct numerical simulation (DNS) of cellar blood flow. We derived a scaling law for margination length. Based on this scaling law, margination length increases cubically with channel height and is independent of shear rate. Using DNS, we verified the proposed scaling law for margination length in straight channels. We also showed that rigidity and size both lead to particle margination. We show that platelet margination can be explained by RBC-enhanced shear-induced diffusion of platelets in the RBC-filled region combined with platelet trapping in the RBC-free region. A simple continuum model is introduced based on the proposed mechanism. Using an experimental correlation for effective diffusivity in blood, the continuum model can recover experimental results from the literature over a wide range of tube diameters. We created an *in vitro* experimental model of thrombosis with and without RBCs. Surprisingly, we found that rapid thrombus growth does not require enhanced platelet transport in the presence of RBCs at high shear. Instead, our results suggest that thrombus growth rate at high shear is dependent on the availability of vWF-A1 domains as opposed to convective transport of platelets. Finally, we obtained empirical correlations for thrombus growth and lag time based on flow parameters by using an *in vitro* model of thrombosis. We developed a simple model for predicting thrombus formation using the obtained empirical correlations. We demonstrated the capability of the model in predicting thrombus formation over a wide range of experimental geometries. This model may be useful for designing blood-contacting devices to avoid unwanted thrombosis.

CHAPTER I

INTRODUCTION

Upon rupture or erosion of a plaque, a platelet-rich thrombus can rapidly grow and may occlude an artery. An occlusive thrombus is the most common cause of clinical events such as angina, myocardial infarction, ischemic attacks and strokes [51, 129, 152]. Occlusive thrombi can cause ischemic cardiac arrest in less than an hour [35, 36]. This unpredictable and sudden event makes atherosclerosis a potentially life-threatening disease. Determining the predominant rate limiting processes governing thrombosis growth rate can guide us in identifying patients at high risk of occlusive thrombosis and developing methods for preventing occlusive arterial thrombosis. In addition to atherosclerosis, prevention of unwanted thrombosis in cardiovascular devices imposes one of the greatest design challenges [8, 117]. Determining the rate limiting processes in thrombus formation could aid manufacturers in designing safer cardiovascular devices while reducing development times and costs.

Platelets play an important role in thrombus formation at high shear. Platelet transport to the surface of a growing thrombus is suggested to limit thrombus growth rate at high pathophysiological shear rates [11, 79, 162]. Transport of platelets in blood is greatly affected by the presence of red blood cells (RBCs). Hydrodynamic interactions due to RBC motions in flowing blood results in the fluctuating motion of RBCs and platelets. In non-dilute suspension of particles in shear flow, particles do not follow straight paths. Particles fluctuate while interacting with neighboring particles and the fluctuations result in a random walk or shear-enhanced diffusion of the particles. RBCs occupy $\sim 40\%$ of the volume of whole blood, and RBC-RBC and RBC-platelet interactions can increase the rate of platelet transport in flowing blood by orders of magnitude compared to Brownian diffusion [53, 175]. The diffusion-like spreading in the platelets motion is referred here as "RBC-enhanced shear-induced diffusion" (RESID).

In addition to RESID, under arterial flow conditions, RBCs migrate away from the walls, and platelets marginate to the RBC-free layer formed near the walls. Platelet margination increases the near-wall platelet concentration compared to the bulk platelet concentration [3, 14, 106, 141, 142]. *In vitro* studies on the rate of platelet adhesion on subendothelium have shown that platelet adhesion is minimal without RBCs and increases with increasing hematocrit, ϕ [1, 2, 147, 150]. Anemic patients may show a prolonged bleeding time [18].

Identifying rate limiting processes in arterial thrombus growth rate helps in preventing pathological vascular occlusion. Based on computational models of thrombus formation [11, 79, 162] and *in vitro* experiments of platelet adhesion on subendothelium [1, 2, 147, 150], we hypothesize that thrombus formation at high shear is limited by platelet transport and therefore requires the presence of RBCs.

In Chapter 2, we quantify the effect of varying hemodynamic parameters within physiologically and pathophysiologically relevant ranges on platelet transport and dynamics by performing direct numerical simulation (DNS) of blood flow. Our hypothesis is that platelet margination in blood flow is due to their smaller deformability and size compared to RBCs. We investigate the effects of platelet and RBC deformability, size, channel size and shear rate on platelet diffusion and margination rate.

In Chapter 3, we investigate the mechanics of platelet margination by DNS of cellular blood flow. From observations of the DNS solutions of platelet margination, we hypothesize that platelet margination is driven by RESID of platelets in the RBC-filled region combined with platelet trapping in the RBC-free region. Based on this hypothesis, we introduce a simple continuum model (DFEB) for platelet transport in flowing blood. We compare platelet margination rates from the continuum model and the rates predicted by the DNS. We then validate the continuum model by comparing the results of the continuum model with experimental results from the literature over a wide range of tube diameters.

In Chapter 4, we experimentally investigate the effect of RBCs on rapid thrombus growth at high shear. We use an *in vitro* model for thrombus growth in stenosed vessels. We investigate whether upstream margination affects rapid thrombus growth. We compare thrombus growth rate in stenoses with entrance length to those with no entrance length. We also, investigate whether RBCs are required for rapid thrombus growth by comparing growth rate in whole blood *vs.* platelet-rich plasma.

In Chapter 5, we investigate the correlation between wall shear rate and thrombus formation rate. We extend the study of Bark et al. [12] by obtaining correlations for thrombus growth and lag time based on flow parameters by using an *in vitro* model of thrombosis. By extending a model introduced by Bark [9] we develop a simple model for predicting thrombus formation using the obtained empirical correlations. We then use this model to predict occlusion times in a platelet function analyzer (PFA-100$^{\mathrm{TM}}$), a microfluidic device with rectangular cross sections [85, 86], and a glass capillary stenosis [22].

CHAPTER II

EFFECTS OF SHEAR RATE, CONFINEMENT AND PARTICLE PARAMETERS ON MARGINATION IN BLOOD FLOW

2.1 Introduction

When a dense suspension of uniformly distributed particles flows under confinement, the particle-particle and particle-wall interactions may lead to the development of a nonuniform concentration profile. Flow of binary suspensions under confinement may increase the concentration of one particle type at the wall. Mild segregation of particles can occur in binary suspensions of rigid spheres [60, 68, 89, 125]. Segregation also occurs in liquid foams of bidisperse and polydisperse bubbles [93, 94]. In suspensions of deformable particles, a high degree of segregation may occur and result in several fold increase in concentration of one particle type at the wall.

A physiologically relevant example of particle segregation in binary suspensions is margination of platelets in blood flow. Blood is a complex fluid consisting of 40% red blood cells (RBCs) by volume. Platelets are small blood cells (with volume of $\approx 10\ \mu\text{m}^3$) that form white clots to stop blood loss upon injury to arterial walls. Under arterial flow conditions, red blood cells (RBCs) migrate away from the walls, and platelets marginate to the RBC-free layer formed near the walls. Platelet margination increases the near-wall platelet concentration compared to the bulk platelet concentration [3, 14, 106, 141, 142]. This increased platelet concentration may contribute to the rapid formation of white clots which is essential for preventing excessive blood loss. Platelet margination occurs in the presence of RBCs (i.e., above a threshold hematocrit of $\phi \approx 0.07$ [41]), and its rate increases with hematocrit

[3, 41, 42, 145, 156, 168, 173] and RBC deformability [72, 73, 74, 98]. In addition to platelets, leukocytes [49, 54], stiff Malaria-infected RBCs [58] and circulating cancer cells [140] may marginate under blood flow conditions.

Due to the particulate nature of margination, numerical investigation of this phenomenon requires a model that captures particle-particle and particle-fluid interactions. With advances in computer hardware and high performance computing, performing the direct numerical simulation (DNS) of the flow of suspensions of several hundreds particles is possible [29, 78]. Several recent studies have investigated the mechanism of margination in suspensions of deformable particles (for a recent review see [73]). Crowl and Fogelson [33] investigated platelet margination by performing two-dimensional simulations of flow of RBC and platelet suspension. They estimated platelet margination using a drift-diffusion equation similar to the approach of [39]. With the drift and diffusion functions estimated from platelet trajectories, the drift-diffusion model underestimated the platelet margination rate by their cellular (DNS) blood flow simulations. To recover the results of the DNS cellular flow simulations, an additional drift term localized at the edge of the RBC-free was required. The authors hypothesized that the orientation angle of tank-treading RBCs at the edge of RBC-free layer may influence the motion of platelets at this region leading to a localized drift.

Numerical studies of Crowl and Fogelson [33] and Zhao et al. [172] suggest that, in contrast to blood flow in capillaries, volume exclusion due to RBC migration is insufficient for platelet margination in arterioles. Kumar et al. [74] studied segregation by stiffness in dilute suspensions of deformable capsules [72, 74], and suggested that pair collisions between capsules of contrasting stiffness contributes to the segregation in such suspensions. In addition to stiffness, Kumar et al. [75] studied segregation by capsule size in suspensions of dilute and semi-dilute suspensions. To analyze their results, they used an idealized master equation that included the effect of heterogeneous collisions and migration velocity from wall. They found that in semi-dilute suspensions of capsules of differing deformability, segregation is both due to the differences in wall-induced migration velocity and heterogeneous collisions between such particles. In suspensions of unequal-sized capsules, segregation was mainly attributed to differences in wall-induced migration velocity. Both of these mechanisms may dominate particle migration across a large portion of the channel in semi-dilute suspensions flowing in relatively small channels; however, these mechanisms may only affect the dynamics in the near-wall region in the flow of dense suspensions in larger channels. Vahidkhah et al. [151] suggested that platelet margination is due to formation of local clusters and cavities in RBC distribution. They proposed that once platelets enter these cavities, they rapidly marginate towards the wall.

In addition to investigating the mechanism of margination with model systems, numerical experiments using DNS can help identify important parameters that affect this process [97, 115]. Identifying parameters affecting margination can help in design and optimization of devices that employ margination for separation of particles and cells from blood, such as Malaria-infected RBCs [58], leukocytes [128], and circulating cancer cells [140]. Furthermore; identifying particle properties that affect margination are important for design of more effective vascular-targeted nano- and micro-carriers [24, 25, 100, 138, 144].

In this study, we focus on margination of particles in the flow of moderately dense suspensions of RBCs flowing under strong to weak confinements. The wall-induced lift force on RBCs and marginating particles strongly depends on the proprieties of these particles particularly their size and deformability. The difference in the wall-induced lift force results in faster migration of RBCs compared to marginating particles. In dilute and semi-dilute suspensions flowing under strong confinements (i.e., with high ratio of particle size to the channel size), this difference in wall migration velocity may strongly affect margination rate. However, in flow of moderately dense suspensions, RBC motions dominate the local hemodynamics in the RBC-laden region and could screen the effect of the wall on RBCs and marginating particles. Thus, we hypothesize that margination rate is mainly driven by the RBC-enhanced diffusion of marginating particles in the RBC-laden region. Based on this hypothesis, we derive a scaling law to identify important parameters affecting margination length L_D. We perform DNS of flowing RBC and marginating particles to verify our proposed scaling law for margination length.

2.2 Scaling relation for margination length

We start by a simple analysis to estimate margination development length. We follow the analysis of Nott and Brady [103] for deriving the timescale for migration in suspensions of rigid spheres. To obtain a scaling relation for margination length, we consider a suspension of RBCs and marginating particles flowing between two parallel plates with separation distance of H. We base our scaling analysis on the hypothesis that shear-induced diffusivity governs particle margination rate. Shear-induced diffusion coefficient in a monodispersed suspension of particles scales as

$$D_{yy} = K\dot{\gamma}a^2, \tag{1}$$

where D_{yy} is shear-induced diffusion coefficient in the lateral direction y, $\dot{\gamma}$ is shear rate, a is particle radius, and K is a nondimensional constant [40, 80, 81]. In suspensions of rigid spheres, K is a function of suspension volume fraction, ϕ. In the binary suspensions of RBC and marginating particles considered here, marginating particles often interact with RBCs because of their lower volume fraction compared to RBCs. Therefor, we use the term RBC-enhanced shear-induced diffusion (RESID) to describe the diffusion of marginating particles due to hydrodynamic effects. The value of diffusion constant K for RESID coefficient depends on RBC volume fraction ϕ, and both RBC and marginating particle properties such as particle deformability and shape.

Assuming that RESID governs lateral displacement of particles in the RBC-filled region, we can estimate the average lateral displacement of marginating particles, $\Delta\overline{w}$, at time t as

$$\Delta\overline{w} \sim 2\sqrt{\overline{D_{yy}}t}, \tag{2}$$

where $\overline{D_{yy}}$ is the average coefficient of RBC-enhanced shear induced diffusivity in the channel. The average relative distance of platelets from wall is defined by $\Delta\overline{w}(t) = \overline{w}(t) - \overline{w}(0)$ where $\overline{w}(t)$ denotes the average distance of platelets from wall $\overline{w}(t) = H/2 - \overline{|y(t) - H/2|}$. Combining (1) and (2), $\Delta\overline{w}$ at time t is given by

$$\Delta\overline{w} \sim 2\sqrt{K\bar{\dot{\gamma}}a^2t}, \tag{3}$$

where $\bar{\dot{\gamma}}$ is the average shear rate across the channel. To express $\Delta\overline{w}$ in terms of average distance traveled in the flow direction, $\bar{x}$, we can write $t = \bar{x}/U$, where U is the average velocity in the flow direction. Assuming that the velocity profile of the suspension in the channel is parabolic everywhere, the average velocity U can be estimated as $U = H\bar{\dot{\gamma}}/3$, yielding $t = 3\bar{x}/(H\bar{\dot{\gamma}})$. Substituting this expression in (3) , we can write $\Delta\overline{w}$ as a function of $\bar{x}$,

$$\left(\frac{\Delta\overline{w}}{H}\right)^2 \sim 12K\frac{a^2\bar{x}}{H^3}. \tag{4}$$

We define the margination development length, L_D, as the length over which the average relative distance of particles from wall is $\sim H$, i.e. $L_D = \bar{x}|_{\Delta\overline{w}\sim H}$. Using this and (4), we can derive an expression for margination length scale

$$L_D \sim \frac{H^3}{12Ka^2} \tag{5}$$

From this scaling relation, margination length L_D scales cubically with channel height H and is not an explicit function of shear rate $\bar{\dot{\gamma}}$. Margination length depends on $\bar{\dot{\gamma}}$ only through the weak change of K with $\bar{\dot{\gamma}}$. In addition to H and $\bar{\dot{\gamma}}$, (5) implies that margination rate depends on the relative size of the marginating particles. We will test the validity of the above scaling law in §2.4.

2.3 Methods

The suspensions of RBCs and marginating particles are directly simulated with a coupled lattice-Boltzmann/spectrin-link (LB-SL) method [113, 115]. In the LB-SL method, a lattice-Boltzmann (LB) solver for the fluid phase (i.e., blood plasma and RBC cytoplasm) is coupled to a coarse-grained spectrin-link (SL) model for the RBC membranes and a rigid dynamic solver for the platelets. Reasor et al. developed the LB-SL method based on the on the initial hybrid lattice-Boltzmann/finite element implementation of MacMeccan et al.[90]. The SL method for modeling the dynamics of the RBC membrane improves on the linear finite element model of [90] by enabling simulation of larger deformations of RBC membrane at higher Capillary numbers at no additional computational cost. In addition, the SL method captures tank-treading dynamics. The LB-SL solver is parallelized using the message interfacing protocol (MPI) to enabled simulation of $O(10^5)$ particles [29].

The SL-LB method has been validated by comparison of mechanical response of individual RBCs with experiments and other computational approaches, such as the deformation of RBC stretched by optical tweezers, deformation of isolated RBCs under high shear, and parachuting RBC in Hagen–Poiseuille flow [113]. The numerical tests performed show good agreement with experimental results and use of less computational resources compared to previous methods used for modeling suspensions. In addition, the SL-LB method has been validated for large scale simulations performed to predict the rheological properties of blood in unbounded shear conditions showed good agreement with rotational viscometer results from literature [114].

2.3.1 Lattice-Boltzmann method

The method used to solve for the fluid phase (i.e., blood plasma and RBC cytoplasm) is based on the D3Q19 single-relaxation-time LB implementation of [7] and [38]. Using Chapman–Enskog expansion (e.g. see [26]), it can be shown that the LB equations converge to the Navier-Stokes equations. The LB method is favorable for simulating suspensions due to several factors. The computational expense of this method scales linearly with the number of particles since particle interactions are propagated on time scales below time scales of particle motions [76, 77]. In addition, the time evolution of the fluid particle distribution at each node only requires the knowledge of particle distribution functions at neighboring nodes, making all calculations localized in space which makes the LB method optimal for parallel computing. Detailed description of the LB method can be found in [6, 26, 136].

The LB method is a mesoscopic approach based on discretization of Boltzmann equation in velocity space in terms of a chosen set of velocity vectors, $\boldsymbol{e}_i$ where $i = 1 \cdots Q$. This chosen velocity vector set results in a discrete lattice space denoted by $\boldsymbol{x}$. Particle distribution function f_i existing at each node can be thought of as the density of mesoscopic particles restricted to flow with velocities of $\boldsymbol{e}_i$. At each time step, the evolution of f_i is governed by the streaming and collision operators. Using the single-relaxation-time collision operator of Bhatnagar-Gross-Krook [16], the time evolution of particle distribution function can be written as:

$$f_i(\boldsymbol{x} + \boldsymbol{e}_i, t + 1) = f_i(\boldsymbol{x}, t) - \frac{1}{\tau} \left[f_i(\boldsymbol{x}, t) - f_i^{(eq)}(\boldsymbol{x}, t) \right] \tag{6}$$

where τ is the Bhatnagar-Gross-Krook relaxation time parameter determining the rate of relaxation to a local equilibrium distribution function $f_i^{(eq)}$. The macroscopic flow kinematic viscosity, ν is related to the relaxation time by $\nu = c_s^2(\tau - 1/2)$ where c_s is the LB pseudo sound speed. At low Mach numbers, i.e., small u/c_s, the local equilibrium distribution can be approximated in terms of local macroscopic variables as

$$f_i^{(eq)}(\boldsymbol{x}, t) = w_i \rho \left[1 + \frac{1}{c_s^2}(\boldsymbol{e}_i \cdot \boldsymbol{u}) + \frac{1}{2c_s^4}(\boldsymbol{e}_i \cdot \boldsymbol{u})^2 - \frac{1}{2c_s^2}(\boldsymbol{u} \cdot \boldsymbol{u}) \right], \tag{7}$$

where ρ and $\boldsymbol{u}$ are macroscopic density and velocity, and w_i denote lattice constants which depend on the LB stencil used. For the D3Q19 stencil used in this study, w_i are

1/3, 1/18, and 1/36 for the rest, non-diagonal and diagonal directions, respectively. The LB pseudo sound speed is $c_s = \sqrt{1/3}$. By definition, the first and second momentum of the discrete distribution functions provide the macroscopic density $\rho(\boldsymbol{x}, t) = \sum_i f_i(\boldsymbol{x}, t)$ and momentum $\rho(\boldsymbol{x}, t)\mathrm{u}(\boldsymbol{x}, t) = \sum_i f_i(\boldsymbol{x}, t)\mathrm{e}_i$.

2.3.2 Coarse-Grained Spectrin Link RBC Membrane Model

The SL model for deformable RBC membranes is inspired by the physiological construction of RBC membrane itself which consists of a cytoskeleton mainly formed by a network of spectrin proteins attached to the RBC membrane lipid bilayer. In the SL approach, the RBC membrane is modeled as a 2D triangular network on the RBC surface. Modeling RBC membrane using spectrin link lengths of $\sim \mathcal{O}(100\text{nm})$, i.e., on the order of protein lengths in an actual RBC requires >25,000 vertices per RBC triangulation [34, 83]. Such a high resolution for modeling each RBC is impractical for simulation of blood flow with $\mathcal{O}(10^3)$ RBCs. Using a coarse-grained SL approach developed by Pivkin and Karniadakis [111] and further improved by Fedosov et al.[46, 47], the RBC membrane can be modeled by a much smaller number of nodes (250-300) while still accurately capturing the membrane elastic response both at small and large deformations.

In the SL model used in this study, the RBC membrane is modeled by a triangulated network. The vertices of the mesh located at $\{\boldsymbol{x}_i\}$, $i \in 1 \cdots N_v$ are connected with N_s springs with lengths of l_i, $i \in 1 \cdots N_s$ forming N_t triangles with areas of $A_k, k \in 1 \cdots N_t$. The Helmholtz free energy of the spectrin network, F, includes in-plane energy $F_{\text{in-plane}}$, bending energy F_κ, volume conservation constraint F_V and area conservation constraint F_A

$$F(\{\boldsymbol{x}_i\}) = F_{\text{in-plane}} + F_\kappa + F_V + F_A. \tag{8}$$

The in-plane free energy, $F_{\text{in-plane}}$, includes the contributions of elastic energy stored in spectrin proteins and hydrostatic elastic energy stored in the membrane

$$F_{\text{in-plane}} = \sum_{i\in 1\cdots N_s} U_{\text{WLC}}(l_i) + \sum_{k\in 1\cdots N_t} \frac{C_q}{A_k^q}. \tag{9}$$

The first sum in (9) represents the elastic energy stored in spectrin links described in terms of the wormlike chain (WLC) model [19, 91]

$$U_{\text{WLC}}(l_i) = \frac{k_B T l_m}{4p} \frac{3x_i^2 - 2x_i^3}{1 - x_i} \tag{10}$$

where k_B is the Boltzmann constant, T is absolute temperature, p is persistence length and $x = l_i/l_m \in [0, 1)$ where l_m is the maximum length of the spectrin links. The attractive potential from the WLC spring forces is balanced by a repulsive potential represented by the second sum in (9). This term represents the hydrostatic energy in stored in the membrane patches. The constant C_q can be derived applying virial theorem and setting the obtained Cauchy stress to zero [45, 46, 47]

$$C_q = \frac{\sqrt{3} A_{l_0}^{q+1} k_B T (4x_0^2 - 9x_0 + 6)}{4pql_m(1 - x_0)^2} \tag{11}$$

where $x_0 = l_0/l_m$, l_0 is the average length of the links at equilibrium and $A_{l_0} = \sqrt{3} l_0^2/4$. We use $q = 1$ in this study.

The bending energy is defined as

$$F_\kappa = \sum_{j\in 1\cdots N_s} \tilde{\kappa}[1 - \cos(\theta_j - \theta_0)] \tag{12}$$

where $\tilde{\kappa}$ is the discrete bending constant, θ_j is the instantaneous angle between adjacent triangles sharing the link j, and θ_0 is the spontaneous angle. The discrete bending modulus $\tilde{\kappa}$ is related to the average bending modulus, κ, by $\tilde{\kappa} = 2\kappa/\sqrt{3}$ [47, 88].

Volume conservation constraint is a nonphysical energy implemented to impose the incompressibility of RBC cytoplasm

$$F_V = \frac{k_v (V - V_0^t)^2}{2V_0^t} \tag{13}$$

where V is the instantaneous volume of RBC and V_0^t is the total desired volume of RBC. Similarly, area conservation constraint is a nonphysical energy implemented to account for the membrane inextensibility

$$F_A = \frac{k_a(A^t - A_0^t)^2}{2A_0^t} \tag{14}$$

where A^t is the total instantaneous area of the membrane, $A^t = \sum_{i\in 1\cdots N_t} A_i$ and A_0^t is the desired membrane area.

The forces on the network vertices resulting from the above energies are derived by

$$\boldsymbol{f}_i^m = \frac{\partial F(\{\boldsymbol{x}_i\})}{\partial \boldsymbol{x}_i}. \tag{15}$$

The expressions for the force expressions can be derived analytically (see Appendix A of [45]).

The location of each vertex $\boldsymbol{x}_i$ is updated by applying the total force $\boldsymbol{f}_i^t$ on each vertex

$$\frac{\mathrm{d}\boldsymbol{x}_i}{\mathrm{d}t} = \boldsymbol{v}_i; \qquad \boldsymbol{f}_i^t = \boldsymbol{f}_i^m + \boldsymbol{f}_i^{\mathrm{fs}} + \boldsymbol{f}_i^{\mathrm{PP}}, \tag{16}$$

where $\boldsymbol{f}_i^{\mathrm{fs}}$ is the force due to fluid-solid coupling, $\boldsymbol{f}_i^{\mathrm{PP}}$ is the force due to particle-particle interactions. The calculation of contact forces due to particle-particle interactions are discussed in detail by [30] and [90]. The location of the vertices are updated via Newton's equations of motion using a first-order accurate forward Euler scheme.

Platelets are modeled as rigid particles. A triangular mesh represents the platelet membrane. A Newtonian solver updates platelet dynamics using the fluid-solid forces on the triangular elements on the platelet surface.

2.3.3 Calculation of RBC-enhanced diffusion of platelets from DNS

The diffusivity of particles is estimated by analyzing single particle trajectories from the DNS model. The shear-induced diffusivity can be estimated from mean square displacements of platelets as a function of time (e.g. see [33, 73, 131, 172]). Here, we estimate diffusion coefficient from step sizes and wait times between successive particle collisions from platelet trajectories. Calculating the step size of particle jumps $\Delta y(y)$ and wait times between successive jumps $\tau(y)$ from particle trajectories, the diffusivity in the y direction can be estimated as

$$D_{yy}(y) = \frac{\langle \delta y^2(y) \rangle}{2\langle \tau(y) \rangle}, \tag{17}$$

where $\langle \delta y^2(y) \rangle$ is the time average of variance of the jump step sizes and $\langle \tau(y) \rangle$ is the time average of wait times τ. The calculated values of $\tau(y)$ and $\Delta y(y)$ depend on the time step, Δt, for resolving the particle trajectories. Resolving particle trajectories with a time step of the same order as the DNS time step resolves the actual fluctuations of the particles within the accuracy of the DNS model. If the time step for particle trajectories, Δt, is much larger than the actual wait times between jumps, τ, then the estimated $\langle \tau(y) \rangle$ approaches the time step used for resolving the trajectories. Therefore, if particle trajectories are resolved with relatively large time steps, calculating the diffusion coefficient from (20) is equivalent to calculating it from a linear growth of mean square lateral displacements of particles with time $\langle y^2(t) \rangle = 2tD_{yy}$. We used $\Delta t \sim 1/\dot{\gamma}$ for resolving particle trajectories.

2.3.4 Setup

We consider the flow of RBC and platelet suspensions between two parallel plates with distances of $H = 40,\ 80$ and $160\ \mu$m. The flow is driven by a constant body force in the axial direction x. The direction normal to the walls is denoted by y with walls located at $y = 0$ and $y = H$. Periodic boundary conditions are applied in the flow direction x and the z direction normal to both x and y directions. A domain length of $L = 80\ \mu$m was chosen for the channels of height $H = 40\ \mu$m. For channels of height $H = 80$ and $160\ \mu$m, domain length of $L = 40\ \mu$m was chosen to lower computation cost. We investigated the effect of domain length L in the flow direction on RBC migration and platelet margination rates. Comparison of margination rates between domains of length $L = 40$ and 80 μm showed negligible differences for channels of height $H = 80$ and 160 μm. In all cases, the channel depth in the z direction was set to 40 μm.

The RBC membrane is resolved by a triangular mesh with 6×10^2 nodes. At equilibrium, the RBCs are biconcave shaped with 8 μm in diameter. The ratio of RBC cytoplasm to plasma viscosity is set to the physiological viscosity ratio of $\lambda = 5$. The mechanical properties of normal RBCs are set as the following: The RBC membrane bending modulus $\tilde{\kappa} = 4.7 \times 10^{-18}$J, the RBC membrane shear modulus $G = 6.3 \times 10^{-6}$J/m^2, the RBC area constraint coefficient $k_a = 1.7 \times 10^{-5}$J/m^2, and the RBC volume constraint coefficient $k_v = 50.9$ J/m^3. The above values of G, k_a, and λ lie within the range of experimentally measured values of RBC mechanical properties [20]. The bending modulus is about an order of magnitude larger compared to the experimental consensus values for $\tilde{\kappa}$. This relatively larger value for $\tilde{\kappa}$ is needed for stabilizing the biconcave shape of the RBCs at low shear rates [83].

Tube hematocrit, hereafter referred to as hematocrit, is defined by the volume fraction of RBCs in the channel at any instant of time. Hematocrit, $\phi(y)$, as a function of distance in the cross flow direction y is calculated as the volume fraction of RBCs along the flow direction x at any point y. The average hematocrit value for a channel, $\bar{\phi}$, represents $\bar{\phi} = \int_{y=0}^{y=H} \phi(y)\mathrm{d}y/H$. Discharge hematocrit $\phi_d(y)$ is the RBC volume fraction in blood flowing out of a channel. Under physiological conditions, the value of the discharge hematocrit is close to the systemic hematocrit. Due to migration of RBCs to the channel center (Fahraeus effect), the average tube hematocrit in micro channels is smaller than the average discharge hematocrit, $\bar{\phi}_d$. We set the average tube hematocrit $\bar{\phi} = 0.20$ in all simulations. The volume fraction of marginating particles (0.018-0.037) is chosen higher than physiological values for platelet volume fraction in blood (~ 0.002) to provide more samples for analysis of margination. To place RBCs

Table 1: DNS parameters of test cases for studying the effect of shear rate on margination. The domain size is $80 \times 40 \times 40\ \mu\mathrm{m}^3$, and the RBC volume fraction is $\phi = 0.20$.

Simulation	$\dot{\gamma}_w$ ($\times 10^3$ s^{-1})	Ca$_G$	Re	Re_{RBC}
1	1	0.23	1.6	0.004
2	5	1.2	8	0.02
3	10	2.3	16	0.04
4	20	4.7	32	0.09

and marginpar particles, initially, a large number of particles was distributed in the domain with random locations and orientations. Marginating particles were selected from the pool of particles such that they are distributed evenly in the y direction (but not necessarily in the x and z directions). RBCs were randomly picked from the remaining pool of particles.

2.4 Results

In this section, we report the effects of shear rate, channel size, particle size and deformability and particle aspect ratio on margination.

2.4.1 Effect of shear rate

We studied the effect of shear rate on platelet margination by simulating the flow of RBC and platelet suspensions in channels of height $H = 40\ \mu$m and varying $\dot{\gamma}_w$ from 10^3 s^{-1} to 2×10^4 s^{-1}. The wall shear rates $\dot{\gamma}_w$ are based on matching channel Reynolds number, $Re = \rho\dot{\gamma}_w H^2/\mu$, and RBC shear Capillary number, $\mathrm{Ca}_G = a_{\mathrm{RBC}}\bar{\dot{\gamma}}\mu/G$, where ρ is plasma density, μ is plasma viscosity and a_{RBC} is the RBC effective radius ($a_{\mathrm{RBC}} = (0.75V_{\mathrm{RBC}}/\pi)^{1/3}$, with V_{RBC} is RBC volume). The RBC Reynolds number is defined as $Re_{\mathrm{RBC}} = \rho\bar{\dot{\gamma}}a_{\mathrm{RBC}}^2/\mu$. The simulation parameter details are given in table 1. The RBCs have an effective radius $a_{\mathrm{RBC}} = 2.9\ \mu$m, resulting in a confinement ratio of $2a_{\mathrm{RBC}}/H = 0.145$. A total number of 240 RBCs results in $\phi = 0.20$. The platelets are modeled as rigid oblate spheroids with a major axis of 2.3 μm and aspect ratio of 2.3. A total number of 100 platelets are used in each simulation. The initial randomly

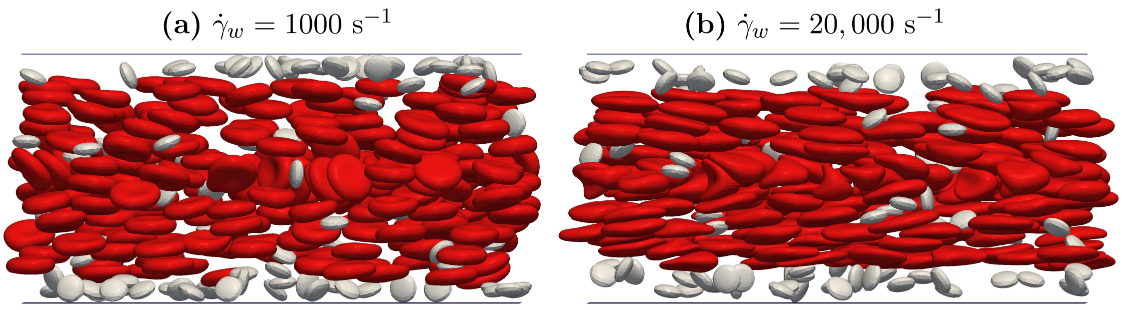
(a) $\dot{\gamma}_w = 1000\ \mathrm{s}^{-1}$ **(b)** $\dot{\gamma}_w = 20,000\ \mathrm{s}^{-1}$

Figure 1: Simulation snapshots of RBC and platelet suspensions flowing in channels of height $H = 40\ \mu$m at shear rates of (a) $\dot{\gamma}_w = 1000\ \mathrm{s}^{-1}$ and (b) $\dot{\gamma}_w = 20,000\ \mathrm{s}^{-1}$.

distributed locations of RBCs and platelets are identical in all cases.

Figure 1 shows snapshots from simulations at $\dot{\gamma}_w = 10^3\ \mathrm{s}^{-1}$ and $2 \times 10^4\ \mathrm{s}^{-1}$ at average traveled distance of $\bar{x} = 9$ mm (i.e., $\bar{x}/H = 225$). At both shear rates, an RBC-free layer forms at wall and platelets concentration increases in this region. At higher shear rate of $\dot{\gamma}_w = 2 \times 10^4\ \mathrm{s}^{-1}$, RBCs are more stretched and elongated along the flow direction compared to $\dot{\gamma}_w = 1 \times 10^3\ \mathrm{s}^{-1}$. This larger deformation of RBCs and higher lift force from the wall at $\dot{\gamma}_w = 20 \times 10^3$ leads to larger RBC-free layer δ compared to $\dot{\gamma}_w = 1 \times 10^3$. To quantify the effect of $\dot{\gamma}_w$ on δ, we defined δ from the RBC hematocrit profiles after reaching equilibrium such that $\phi(\delta) = 0.005$ (figure 2). In channels of height $H = 40\ \mu$m, we found $\delta = 3.0$, 3.8, 4.6 and 5.2 μm at wall shear rates of $\dot{\gamma}_w = 10^3$, $5{\times}10^3$, 10^4 and $2{\times}10^4\ \mathrm{s}^{-1}$, respectively. The RBC-free layer thickness follows a power-law relation of $\delta \propto \mathrm{Ca}_G^{0.2}$. *In vitro* experiments of [62] in 100 μm square channels, showed that the δ of RBC suspensions with $\phi = 0.20$ follows a similar power-law trend over a range of shear rates of $\dot{\gamma}_w \sim 1.5 \times 10^3 - 7 \times 10^4$.

To quantify the effect of $\dot{\gamma}_w$ on margination length, we calculated the average relative distance of platelets from wall $\Delta\overline{w}(t) = \overline{w}(t) - \overline{w}(0)$. Figure 3(a) shows $\Delta\overline{w}$ as a function of time for various $\dot{\gamma}_w$ values. The average distance of platelets from wall decreases as they marginate to the RBC-free layer. As expected, platelets approach the wall faster with increasing shear rate. Plotting $\Delta\overline{w}$ as a function of average

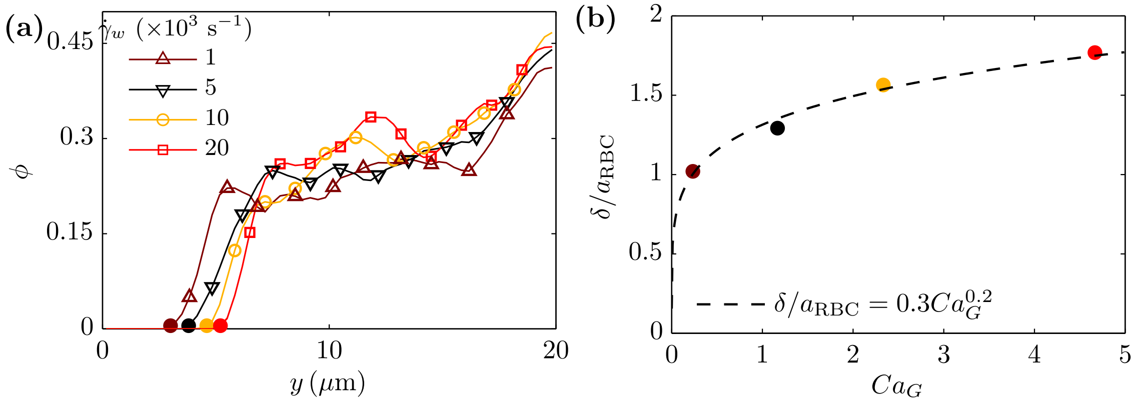

Figure 2: Effect of wall shear rate on RBC-free layer thickness ,δ. (a) Profiles of hematocrit ϕ at wall shear rates of $\dot{\gamma}_w = 10^3$, 5×10^3, 10^4 and 2×10^4 s^{-1} in channels of height $H = 40$ μm. Hematocrit profiles are plotted in the cross-channel direction, y. The edge of the RBC-free layer is defined as $\phi(\delta) = 0.005$ (denoted by filled circles). (b) The thickness of the RBC-free layer (denoted by filled circles) increases with increasing wall shear rate.

distance traveled $\bar{x}$ (figure 3(b)), shows that the variation of $\Delta\overline{w}$ as a function of $\bar{x}$ is almost independent of $\dot{\gamma}_w$. This result verifies the scaling relation for margination length introduced in (5). At higher shear rates, the values of $\Delta\overline{w}$ is slightly lower. This effect is likely due to the larger RBC-free layer δ.

The effect of shear rate on margination rate is unclear due to disparities among experimental results from the literature. In rectangular channels with 30, 50 and 100 μm width, near wall platelet concentration was observed above sufficiently large shear rates of 210 s^{-1}, and further increases in shear rate increased the near wall to core concentration ratio [41]. However, the dependence of the near-wall to core concentration ratio was different between 30, 50 and 100 μm channels. The near wall to core ratio increased more uniformly at 100 μm compared to 50 and 30μm channels [41]. Results of [3] also showed a nearly uniform increase in the near wall to core concentration ratio of platelets with an increase of shear rate from 240 s^{-1} to 1200 s^{-1}. However, this behavior was contrasted by the results of [168] where in tubes of 200 μm diameter at hematocrit of 40%, the rate of lateral transport of platelets was

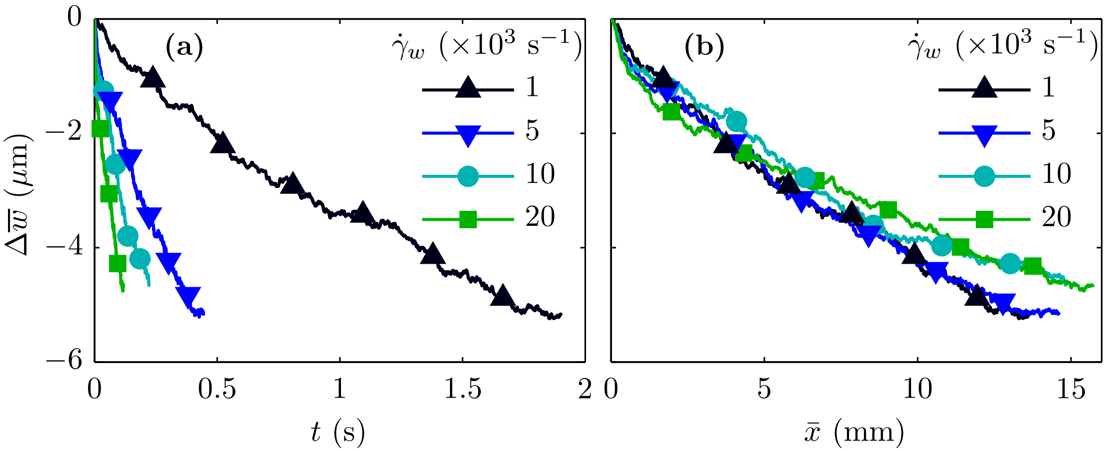

Figure 3: Average relative distance of platelets from the channel wall at wall shear rates of $\dot{\gamma}_w = 10^3$, 5×10^3, 10^4 and 2×10^4 s^{-1} plotted as a function of (a) time and (b) average distance traveled along the flow direction $\bar{x}$. The channel height is $H = 40$ μm. The average relative distance of platelets from wall is defined by $\Delta\overline{w}(t) = \overline{w}(t) - \overline{w}(0)$ where $w(t)$ denotes the distance of platelets from wall $w(t) = H/2 - |y(t) - H/2|$.

found to be less at wall shear rates of 250 s^{-1} or 1220 s^{-1} compared to 560 s^{-1}. Results of [174] showed a small increase of platelet near wall excess when shear rate was increased five times from 3000 s^{-1} to 15000 s^{-1}.

In our analysis for deriving margination length, we assumed that suspensions of deformable RBCs exhibit shear-induced diffusivity with the same functional form as shear-induced diffusivity in suspensions of rigid spheres, i.e., $D_{yy} = K\dot{\gamma}a^2$. In suspensions of rigid spheres, the nondimensional parameter K depends on hematocrit ϕ. We calculated the RESID of platelets in the cross flow direction from platelet trajectories at various wall shear rates. As expected, RESID of platelets is lowest in the RBC-free region (figure 4(a)). The maximum of $D_{yy}(y)/\dot{\gamma}_w$ occurs at $y \sim 8$ μm, collocated with the first peak of the hematocrit profile (figure 2(a)). Despite the vanishing (time-averaged) shear rate in the channel center, the value of $D_{yy}/\dot{\gamma}_w$ in the channel center is nonzero. This nonzero value is due to the finite size of RBCs and platelets. Figure 4(b) shows that similar to suspensions of rigid particles, the nondimensional parameter $K = D_{yy}/(\dot{\gamma}a^2)$ in RBC suspensions increases with increasing hematocrit ϕ. In addition to ϕ, the value of K also depends on $\dot{\gamma}$. Figure 4

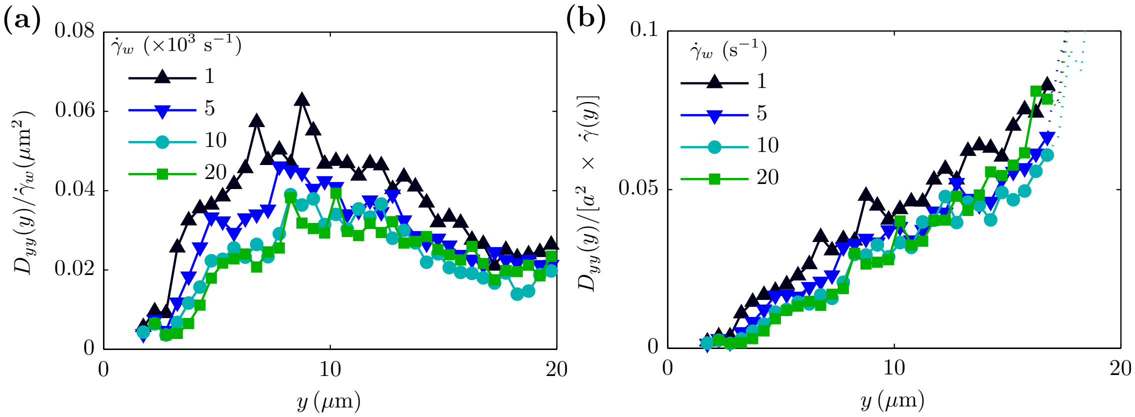

Figure 4: Cross-channel profiles of platelet effective diffusivity D_{yy} calculated from DNS platelet trajectories at various shear rate rates in channels of height $H = 40$ μm. Effective diffusivity is normalized by (a) wall shear rate $\dot{\gamma}_w$ and (b) by $a^2 \times \dot{\gamma}(y)$ where a is platelet effective radius and $\dot{\gamma}(y)$ is local shear rate in the cross flow direction, y.

shows that D_{yy} normalized by shear rate is a weak function of shear rate, and the value of K decreases with increasing $\dot{\gamma}_w$. While effective diffusivity of rigid spheres in non-colloidal suspensions scales linearly with $\dot{\gamma}$ [81, 103, 131], RESID scales sublinearly with $\dot{\gamma}$. The decrease of $D_{yy}/(\dot{\gamma}a^2)$ with increasing $\dot{\gamma}$ is consistent with the results of numerical studies of Zhao et al. [172] who found that the nondimensional self-diffusivity of platelets decreases with Ca in suspensions of platelets and RBCs flowing in microchannels of $H = 34$ μm. Pranay et al. [112] found that the nondimensional short-time self-diffusivity $D_{yy}/(\dot{\gamma}a^2)$ of elastic capsules is a non-monotonic function of Ca over a range of $0.08 \leq \text{Ca} \leq 0.6$ with maximum value of $D_{yy}/(\dot{\gamma}a^2)$ occurring at $\text{Ca} \approx 0.14$.

2.4.2 Effect of channel size

We investigated the effect of channel height H on RBC migration and platelet margination rate by simulating the flow of RBC and platelet suspensions in channels of height $H = 40$, 80 and 160 μm. The RBCs have an effective radius $a_{\text{RBC}} = 2.9$ μm. Simulations were performed at hematocrit of $\phi = 0.20$. The simulation parameter details are given in table 2. The wall shear rates $\dot{\gamma}_w$ are based on matching RBC shear Capillary

Table 2: DNS parameters of test cases for studying the effect of channel size on margination. In all cases, the channel depth in the z direction is 40 μm, and the RBC volume fraction is ϕ=0.20.

H (μm)	L (μm)	RBCs	Platelets	$\dot{\gamma}_w$ (s^{-1})	Ca$_G$
40	80	240	100	503	0.28
80	40	240	100	242	0.14
160	40	480	400	100	0.07

number, Ca$_G$. The platelets are modeled as oblate spheroids with a major axis of 2.3 μm and aspect ratio of 2.3.

The average lateral displacement of RBCs and platelets relative to the channel wall $\Delta\overline{w}$ as a function of the average traveled distance $\overline{x}$ for various H values is shown in figure 5(a). Margination developing length L_D is much shorter for smaller channels. Also, RBC migration occurs over a much shorter length compared to platelet margination. This large difference in developing scales shows that platelet margination cannot be explained by passive advection of platelets by plasma as RBCs migrate towards channel center. If $\Delta\overline{w}$ is normalized by height H and $\overline{x}$ is normalized by a^2/H^3, RBC and platelet average trajectories collapse for all cases (figure 5(b)). This result verifies the scaling relation for margination length introduced in (5). Also, when $\overline{x}$ of RBCs and platelets is scaled by the square of their equivalent radii a^2 , the development-length of RBC migration and platelet margination appears to occur on closer length scales both of which are of the order of $\mathcal{O}(1)$.

In most experimental studies, concentration of marginating particles are measured at large entrance lengths such that variations in concentration are not detectable. We are not aware of an experimental study specifically designed to measure the effect of channel size on margination developing length, yet comparison of margination developing length from different studies performed at various channel sizes supports our results that margination development length greatly increases with the increase of channel size. Xu and Wootton [165] found that near-wall platelet concentration in tubes of D = 3 mm perfused with whole porcine blood is doubled in steady flow

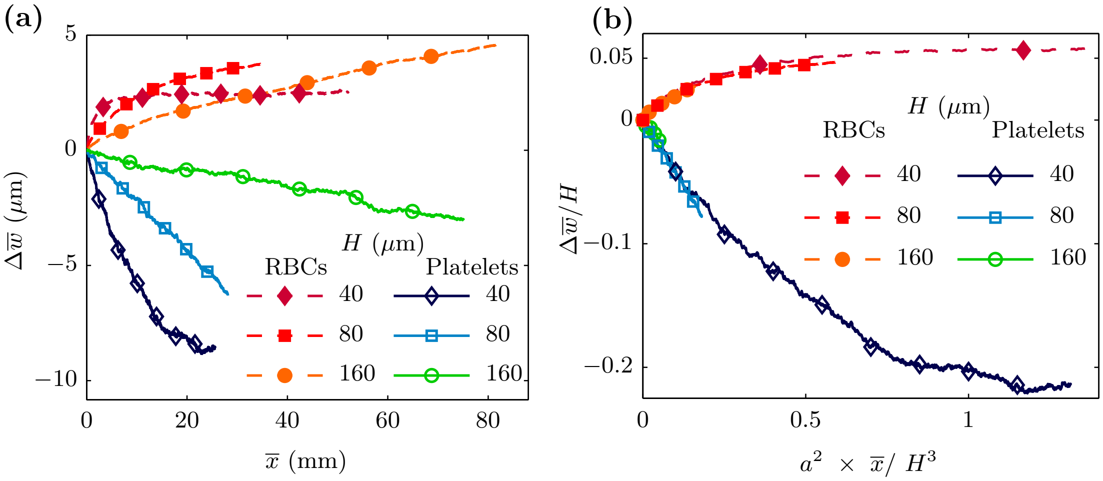

Figure 5: Effect of channel size H on RBC migration and platelet margination rate. (a) Average relative distance of RBCs and platelets $\Delta\overline{w}$ is plotted as a function of average distance traveled $\overline{w}$ in channels of height H = 40, 80 and 160 μm. (b) Normalizing $\Delta\overline{w}$ by channel height H and normalizing $\bar{x}$ by a^2/H^3 results in a collapse of the curves.

at $L = 50$ cm from the blood reservoir, but only increased by ≈ 1.5-fold at $L = 10$ cm. While the near-wall platelet concentration is approximately doubled in tubes of $D = 3$ mm over $L = 50$ cm ($L/D \approx 167$), the near-wall concentration of platelet-sized beads is doubled over $L \lesssim 5$ mm in tube of $D = 200\mu$m ($L/D \approx 25$) perfused with RBC suspension of $\phi = 0.30$ [156]. Zhao et al. [173] reported margination development length of $\lesssim 2.5$ mm in 100 μm ($L/H \lesssim 25$) square channels perfused with 40% hematocrit RBC suspensions. They measured a near-wall excess of 7-9 fold at $L = 2.5$ mm in RBC suspensions of $\phi = 0.40$.

2.4.3 Effect of particle size and deformability

To study the effect of particle size and deformability on margination, we varied the size and deformability of marginating particles in the presence of RBCs. We considered the flow of RBC suspensions in channels of height $H = 40$ μm at wall shear rate of $\dot{\gamma}_w = 10 \times 10^3$ s^{-1}. The wall shear rate $\dot{\gamma}_w$ is based on matching channel Reynolds number, Re, and RBC shear Capillary number, Ca$_G$. The RBCs have an effective

Table 3: Properties of marginating particles in test cases for studying the effect of size and deformability on margination. Domain size is 80×40×40 μm ^{3}.

Simulation	Size of marginating particles (r^*)	Ca*
Small rigid RBCs	0.5	0
Small soft RBCs	0.5	1
Rigid RBCs	1.0	0

radius $a_{\text{RBC}} = 2.8\ \mu$m, resulting in a confinement ratio of $2a_{\text{RBC}}/H = 0.14$. A total number of 272 RBCs results in an average hematocrit of $\phi = 0.20$.

To compare the effect of size vs deformability on margination, we varied the size and deformability of the marginating particles. The relative size of marginating particles compared to the RBCs is denoted by $r^* = a_m/a_{\text{RBC}}$, where a_m is the effective radius of the marginating particle. We compared the margination rate of rigid RBCs to the margination rate of small soft RBCs and small rigid RBCs. The mechanical properties of the small soft RBCs (i.e., membrane shear modulus G, bending modulus $\tilde{\kappa}$, area constraint coefficient k_a, and volume constraint coefficient k_v) were scaled by matching the nondimensional parameters $\text{Ca}_G = \dot{\gamma}a\mu/G$, $\text{Ca}_\kappa = \dot{\gamma}a^3\mu/\tilde{\kappa}$, $\text{Ca}_a = \dot{\gamma}a\mu/k_a$ and $\text{Ca}_v = \dot{\gamma}\mu/k_v$. The relative deformability of marginating particles compared to the RBCs is denoted by $\text{Ca}^* = \text{Ca}_m/\text{Ca}_{\text{RBC}}$, where Ca_m and Ca_{RBC} are any of the above nondimensional parameters (i.e. Ca_G, Ca_κ, etc.). By comparing the dynamics of single RBCs of $r^* = 1$ and 0.5, we have verified that the above scaling of the RBC membrane mechanical properties results in similar dynamics. A total number of 100 small marginating particles are used. To reduce the effect of rigid RBCs on the flow, two simulations with a total number of 50 rigid RBCs were performed for rigid RBCs. The initial locations of RBCs and marginating particles are identical in all cases. The properties of marginating particles for different cases are listed in Table 3.

Figure 6 shows the average trajectories of RBCs and marginating particles. Smaller size and less deformability both lead to particle margination. Comparison of average

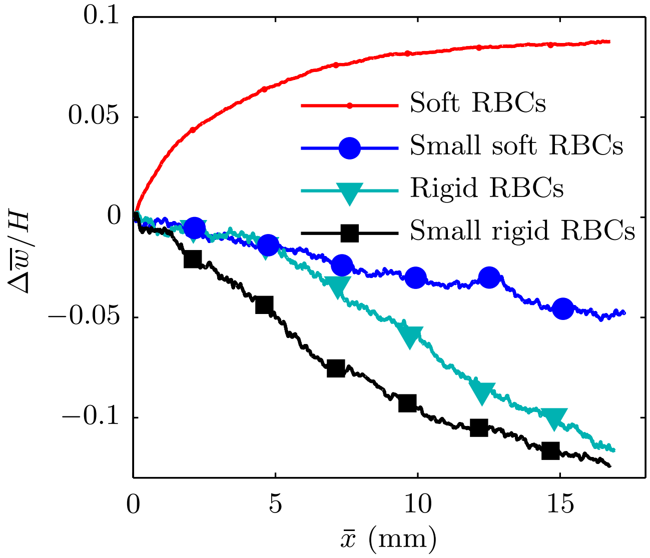

Figure 6: Average relative distance of platelets of various size and deformability from the channel wall. The channel height is $H = 40$ μm.

trajectories of rigid RBCs with the average trajectories of soft small RBCs shows rigidity has a more significant effect compared to size within the range of parameters in this study. When both effects are combined,i.e. small rigid RBCs, margination rate is the most rapid.

In monodispersed suspensions of rigid spheres, shear-induced diffusion depends on the size of the particles, since the displacement of the particles upon collision is of the order of particle size. We calculated the RESID of marginating particles in the cross flow direction from particle trajectories. As expected, RESID of small particles (i.e., RESID of small rigid RBCs and small soft RBCs) is smaller compared to the RESID of rigid RBCs (figure 7(a)). In the binary suspension of RBCs and marginating particles, RESID depends on the size of both RBCs and the marginating particle. If the volume fraction of the marginating particles are small relative to the volume fraction of RBCs, we may assume that the marginating particles are often interacting with RBCs. The smaller RESID of smaller marginating particles (figure 7(a)) suggests that the displacement of marginating particles upon collision with RBCs is smaller compared to those of large particles. In addition, RESID of small

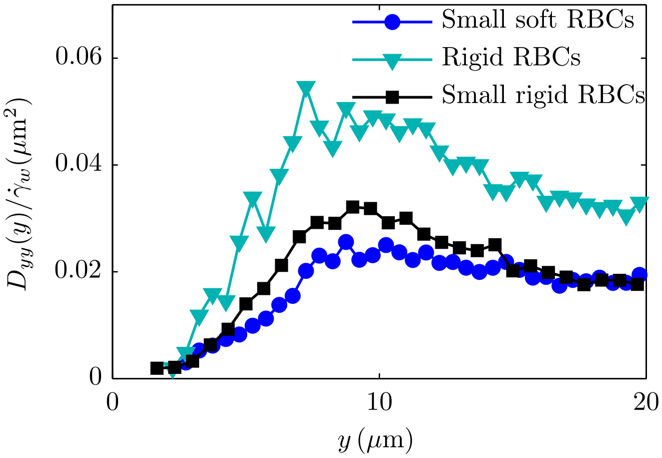

Figure 7: Cross-channel profiles of effective diffusivity of marginating particles D_{yy} calculated from DNS platelet trajectories in channels of height $H = 40$ μm. Effective diffusivity is normalized by wall shear rate $\dot{\gamma}_w$.

particles is not a strong function of their deformability. RESID of small soft RBCs is slightly smaller compared to the RESID of small rigid RBCs.

Kumar et al. [75] analyzed cross-stream displacement of colliding particles of varying size and deformabilities. They found that the cross-stream displacement of small particles upon colliding with large particles (with size ratio of 0.8) is larger compared to the cross-stream displacement of two large particle of the same size. This contrasting result may be due to the difference between the size ratio of colliding particles considered in the two studies (i.e. 0.5 in this study *vs.* 0.8 in [75]).

2.4.4 Effect of particle shape on margination rate

We studied the effect of shear rate on platelet margination by simulating the flow of RBC and platelet suspensions in channels of height $H = 40$ μm at $\dot{\gamma}_w = 10 \times 10^3$ s^{-1}. The wall shear rate $\dot{\gamma}_w$ is based on matching channel Reynolds number, Re, and RBC shear Capillary number, Ca_G. The RBCs have an effective radius $a_{\mathrm{RBC}} = 2.8$ μm, resulting in a confinement ratio of $2a_{\mathrm{RBC}}/H = 0.14$. A total number of 272 RBCs results in $\phi = 0.20$. The marginating particles are modeled as rigid spheroids with aspect ratios of $AR = 0.5$, 1, 2 and 4 and volume $V = 8$ μm^3. A total number of

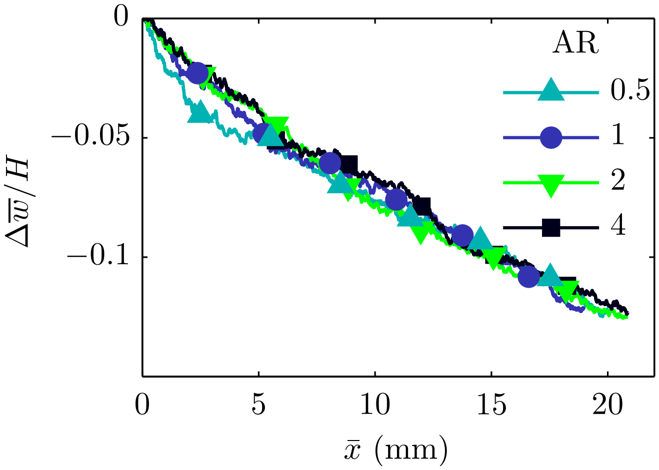

Figure 8: Average relative distance of platelets of various aspect ratio (AR) from the channel wall. The channel height is $H = 40$ μm. The average relative distance of platelets from wall is defined by $\Delta\overline{w}(t) = \overline{w}(t) - \overline{w}(0)$ where $w(t)$ denotes the distance of platelets from wall $w(t) = H/2 - |y(t) - H/2|$. The average relative distance of platelets from wall $\Delta\overline{w}$ is normalized by channel height, H.

100 rigid spheroids are used in each simulation. The initial locations of RBCs and spheroids are identical in all cases.

Figure 8 shows that margination rate is almost independent of the aspect ratio of the marginating particles within the range of parameters studied here. We have previously found that for larger particles with volume $V = 23.5$ μm^3, margination rate slightly increases as aspect ratio decreases [115]. This different behavior suggests that below a certain volume fraction, margination rate is independent of particle aspect ratio. This result is in agreement with the numerical results of Müller et al. [97].

2.5 Conclusion

In this study, we investigated the effects of important flow and particle properties on margination of particles in RBC suspensions. We derived a scaling law for margination length based on the assumption that margination is mainly driven by RESID. Based on this scaling law, margination length increases cubically with channel height H and is independent of shear rate. The results of our DNS of the flow of RBC and marginating particles in straight channels verified the proposed scaling law for margination length. We also showed that rigidity and size both lead to particle margination, with rigidity having a more significant effect compared to size within the range of parameters in this study.

CHAPTER III

A CONTINUUM MODEL FOR PLATELET TRANSPORT IN FLOWING BLOOD BASED ON DIRECT NUMERICAL SIMULATIONS OF CELLULAR BLOOD FLOW

3.1 Introduction

Thrombus growth over ruptured or eroded atherosclerotic lesions can rapidly lead to arterial occlusion. This unpredictable and sudden event makes atherosclerosis a potentially life-threatening disease. Stenosis severity is considered as a major factor for identifying plaque vulnerability, but a large number of occlusive thrombi occur in moderately stenotic lesions [87, 99]. Identifying vulnerable patients is still a major challenge in preventive diagnosis and treatment of patients with atherosclerosis. There is a need for better tools for preventive diagnosis and predicting the outcomes of alternative treatments for this complex disease. Computational models of arterial thrombus formation may be utilized to provide quantitative estimates of thrombosis risk based on patient-specific geometries and individual physiologic data [107, 143]. But current models of arterial thrombus formation have limited practical applicability, since they rely on critical assumptions that limit their validity. Platelet transport to the surface of a growing thrombus may be a rate limiting step in rapid thrombus formation, so accurate estimation of platelet transport to the surface of a growing thrombus may be essential for simulation of arterial thrombus models.

Transport of platelets in blood is greatly affected by the presence of red blood cells (RBCs). Hydrodynamic interactions due to RBC motions in flowing blood results in the fluctuating motion of RBCs and platelets. In suspension of particles in shear flow, particles do not follow straight paths. Particles fluctuate while interacting with neighboring particles and the fluctuations result in a random walk or shear-enhanced diffusion of the particles. RBCs occupy $\sim 40\%$ of the volume of whole blood, and RBC-RBC and RBC-platelet interactions can increase the rate of platelet transport in flowing blood by orders of magnitude compared to Brownian diffusion. The diffusion-like spreading in the platelets motion is referred here as "RBC-enhanced shear-induced diffusion". Computational models of thrombus formation suggest that RBC-enhanced diffusivity of platelets is required for rapid thrombus growth [11].

In addition to the RBC-enhanced diffusivity, in flowing blood, platelets marginate towards vessel walls increasing the concentration of platelets at the near-wall region. Platelet margination was noted as early as 1966 through the indirect observation of higher platelet concentration in small tubes branching from larger tubes that indicated the higher concentration of platelets in a skimming layer [14, 106]. Platelet margination in blood flow has been directly observed *in vivo* in mesenteric arterioles of rabbit [141, 142, 160, 161]. *In vitro* experiments on margination of platelet-sized micro particles in blood flow suggests that platelet margination occurs in the presence of RBCs (i.e., above a threshold average hematocrit of $\phi \sim 0.07$ [41]), and its rate increases with hematocrit [3, 41, 42, 145, 156, 173] and RBC deformability [42]. Computational models of thrombus formation suggest that without near-wall excess (NWE) of platelets thrombus growth is limited, and a nonuniform platelet concentration profile is required for substantial thrombus growth rate [79].

Most models of platelet transport fall into two categories: continuum (phenomenological) models and direct numerical simulations (DNS) of cellular blood flow. Compared to DNS, continuum models are practical for estimating platelet transport in patient-specific models of thrombus formation, because they require less computational time and resources and are easier to implement for complex geometries. But due to the particulate nature of platelet transport in flowing blood, continuum models have difficulty predicting both RBC-enhanced diffusion of platelets and platelet margination consistent with experimental results.

Continuum models assume that platelets behave as a dilute species in blood and the convection-diffusion equation governs the transport of platelet concentration in blood. Typically, the diffusion term is estimated by experimental correlations for the effective diffusivity of solutes in blood given by Keller[64] or Zydney and Colton[175]. To account for the NWE of platelets, nonuniform concentration profiles have been implemented as the inlet boundary condition for platelet concentration [79, 133], but the RBC-enhanced diffusivity diminishes the concentration nonuniformity as the blood flows into the domain [59, 133]. To ameliorate the dissipation of platelet concentration profiles, Sorensen et al. [133] adopted the approach of Strong et al. [135] and estimated the value of effective diffusivity of platelets to obtain the best agreement with the experimental results. Another approach is to augment the platelet concentration in the entire domain such that platelet concentration matches that of the near-wall [61, 163]. This approach may lead to overestimation of platelet flux to the wall.

Phenomenological models have been developed to capture both RBC-enhanced platelet diffusivity and platelet margination. Eckstein and Belgacem [39] introduced a convection-diffusion equation with an additional drift term to account both for the RBC-enhanced diffusivity of platelets and margination of platelets. In this approach, the drift function is estimated from the fully developed concentration profile of platelets. The estimate of the developing length for platelets concentration from this method is in agreement with experimental results of Waters and Eckstein [156]; however, this method requires the knowledge of the fully developed concentration profile for estimating the drift function [39, 169]. Kao[63] modeled platelet margination based on the assumption that platelet margination occurs as RBCs migrate away from the wall towards the core ejecting plasma and platelets outward towards the walls. Kao modeled RBC migration based on the phenomenological model of Phillips et al.[110] for shear-induced migration of particles. Phillips et al. assumed that spatial variations in particle collision frequencies creates shear-induced particle migration. They proposed that particle collision frequency is proportional to particle volume fraction and shear rate. Following a similar approach to Phillips et al., Hund and Antaki [59] introduced a model that incorporates a field potential to drive platelet fluxes. The parameters of the polynomial representing the field potential were calibrated with experimental measurements of platelet concentration profiles in 200 μm channels. This model preserves the nonuniformity of platelet concentration profiles, but the development time estimated from this model appears to be much longer than the experimental results of Waters and Eckstein [156].

With advances in computer hardware and high performance computing, performing the DNS of cellular blood flow in vessels of the order of 100 μm diameter is possible [29, 78]. DNS provides estimates of quantities that are difficult to measure experimentally, and allows performing numerical experiments in idealized situations. Analysis of particle trajectories and velocity fluctuations from the DNS of blood flow has allowed detailed investigation of the diffusive motion of platelets and Lagrangian tracer points under different flow conditions [171, 172]. Numerical experiments of Crowl and Fogelson [33] and Zhao et al. [172] suggest that, in contrast to blood flow in capillaries, volume exclusion due to RBC migration is insufficient for platelet margination in arterioles. The DNS of blood flow in arterial geometries with relevant physiological length scales is currently impractical. However, the above studies show that DNS can help us improve continuum models of platelet transport by providing insight into the mechanism of this phenomena in flowing blood. We follow this approach for modeling platelet transport.

In this study, we have investigated the underlying physics of platelet margination in blood flow by performing DNS of RBC and platelet suspensions between parallel plates. From observations of the DNS solutions of platelet margination, we hypothesize that platelet margination is driven by RBC-enhanced diffusion of platelets at the cell-laden region plus a local free-escape effect at the edge of the cell-laden region. Based on this hypothesis, we introduce a simple continuum model of platelet diffusivity plus a local effect at the edge of the cell-laden region. We compare platelet margination rates from the continuum model and the rates predicted by the DNS. The continuum model estimates of platelet margination in the developing regime are also compared with experimental results in 200 μm[156] and 3 mm diameter channels [164].

3.2 Methods

For performing the DNS of blood flow, we used a coupled lattice-Boltzmann/spectrin-link (LB-SL) method which is briefly described here, for more details see [113, 115]. In this method, a lattice-Boltzmann (LB) solver for the fluid phase (i. e. blood plasma and RBC cytoplasm) is coupled to a coarse-grained SL model for the RBC membranes and a rigid dynamic solver for the platelets. The LB solver is based on the three-dimensional D3Q19 model with a single relaxation time BGK model described in [7].

We consider the flow of RBC and platelet suspensions between two parallel plates with distances of $H = 40,\ 80$, and 160 μm (Table 4). The flow is driven by a constant body force in the axial direction x. The direction normal to the walls is denoted by y with walls located at $y = 0$ and $y = H$. The particle lateral distance from the closest channel wall is $w = H/2- \mid y - H/2 \mid$. Periodic boundary conditions are applied in the flow direction x and the z direction normal to both x and y directions. To lower computation cost, we investigated the effect of domain length L in the flow direction on RBC migration and platelet margination rates. Comparison of margination rates between domains of length $L = 40$ and 80 μm showed negligible differences for channels of height $H = 80$ and 160 μm. Thus, a domain length of $L = 40$ μm was chosen for the channels of height $H = 80$ and 160 μm.

Table 4: DNS parameters. In all cases, the channel depth in the z direction is 40 μm, and the RBC volume fraction is $\phi = 0.20$.

$H(\mu\text{m})$	$L(\mu\text{m})$	RBCs	Platelets	$\dot{\gamma}_w$ (s^{-1})	ϕ_d	Ca
40	80	240	100	503	0.32	0.28
80	40	240	100	242	0.27	0.14
160	40	480	400	100	0.24	0.07

The RBC membrane is resolved by a triangular mesh with 613 nodes. At equilibrium, the RBCs are biconcave shaped with 8 μm in diameter. The ratio of RBC cytoplasm to plasma viscosity is set to the physiological viscosity ratio of $\lambda = 5$. In all simulations, we assume: The RBC membrane bending modulus $\kappa_b = 4.7 \times 10^{-18}$J, the RBC membrane shear modulus $G = 6.3 \times 10^{-6}\text{J/m}^2$, the RBC area constraint coefficient $\kappa_a = 1.7 \times 10^{-5}\text{J/m}^2$, and the RBC volume constraint coefficient $\kappa_v = 50.9$ J/m^3. The above values of G, κ_a, and λ lie within the range of experimentally measured values of RBC mechanical properties [20]. The bending modulus is about an order of magnitude larger compared to the experimental consensus values for κ_b. This relatively larger value for κ_b is needed for stabilizing the biconcave shape of the RBCs at low shear rates [83] . The platelets are modeled as oblate spheroids with a major axis of 2.3 μm and aspect ratio of 2.3. Platelets are modeled as rigid particles. A triangular mesh represents the platelet membrane. A Newtonian solver updates platelet dynamics using the fluid-solid forces on the triangular elements on the platelet surface. Hematocrit, $\phi(y)$, as a function of distance in the cross flow direction y is calculated as the volume fraction of RBCs along the flow direction x at any point y. The average hematocrit value for a channel, $\bar{\phi}$, represents $\bar{\phi} = \int_{y=0}^{y=H} \phi(y)\text{d}y/H$. The average tube hematocrit is $\bar{\phi} = 0.20$ in all simulations. Tube hematocrit, hereafter referred to as hematocrit, is defined by the volume fraction of RBCs in the channel at any instant of time. Discharge hematocrit $\phi_d(y)$ is defined as the RBC volume fraction in blood flowing out of a channel. Due to migration of RBCs to the channel center (Fahraeus effect), the average discharge hematocrit, $\bar{\phi}_d$, is much larger than the average tube hematocrit in small channels. The volume fraction of platelets (0.018-0.037) is chosen higher than physiological values (~ 0.002) to provide more samples for analysis of platelet margination. To place platelets and RBCs, initially, a large number of particles was distributed in the domain with random locations and orientations. Platelets were selected from the pool of particles such that they are distributed evenly in the y direction (but not necessarily in the x and z directions). RBCs were randomly picked from the remaining pool of particles. The simulation parameter details (i.e. the domain size, the number of RBCs and platelets, wall shear rate $\dot{\gamma}_w$, discharge hematocrit ϕ_d, and RBC Capillary number Ca) are given in Table 4. Flow parameters are presented in physical units to emphasize relevance to blood flow data. The wall shear rates $\dot{\gamma}_w$ are based on matching RBC Capillary number, $\mathrm{Ca} = a_{\mathrm{RBC}}\dot{\gamma}_w\mu/G$, where a_{RBC} is the RBC effective radius ($a_{\mathrm{RBC}} = (0.75V_{\mathrm{RBC}}/\pi)^{1/3}$ where V_{RBC} is RBC volume) and μ is plasma viscosity.

3.3 Results

3.3.1 Direct numerical simulations

Fig. 9 shows the trajectories of platelets and RBCs in a channel of height $H = 80$ μm. The simulation domain size is 40 μm with periodic boundary conditions in the flow direction x. Particles leave one side and re-enter from the other side of the domain. In Fig. 9, we are plotting the lateral positions of particles as a function of total average distance traveled along the flow direction. Eventually, platelets accumulate in a region near the wall that coincides with the RBC-free layer. From a kinematic view point, platelet accumulation in the RBC-free layer requires a net lateral flux of platelets towards the walls. One hypothesis for this outward platelet flux is the presence of a “drift” velocity across the channel pushing the platelets to the walls. However, a local effect at the edge of the cell-laden region may also induce a net lateral flux of platelets to the walls. We observe such a local effect at the edge of the RBC-free

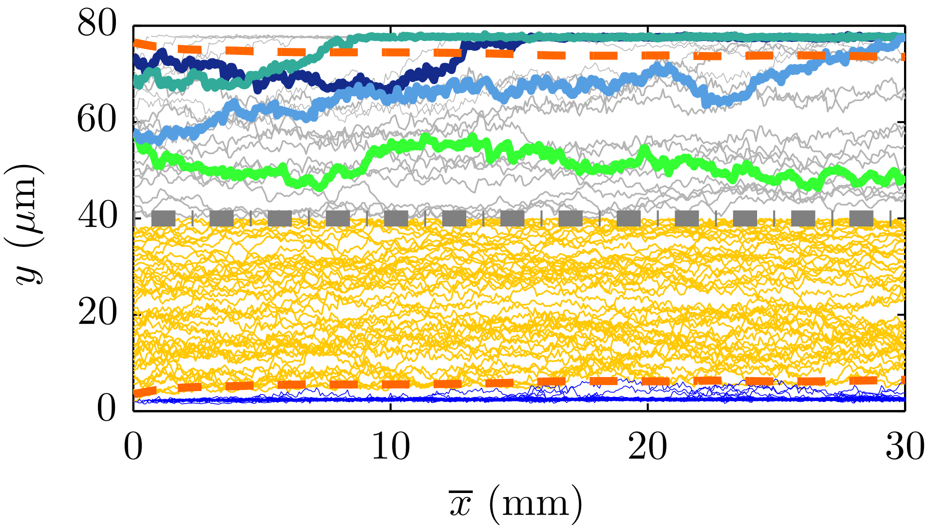

Figure 9: Platelet and RBC trajectories in a channel of height $H = 80$ μm calculated using the DNS model of blood flow. The dashed-dotted line represents the channel center line with walls both on the top and bottom. The top half of the channel shows the trajectories of the platelets as they marginate upwards towards the wall. A few trajectories of the platelet plotted on top are highlighted. The light (yellow online) lines on the bottom half of the channel are RBC trajectories. For clarity, only one tenth of the platelet trajectories on top and the RBC trajectories on bottom are plotted. The dark (blue) lines on the bottom half of the channel are the trajectories of platelets after reaching the RBC-free layer with thickness of $\delta = 3.9$ μm. The dashed (red) lines follow the trajectories of the first layer of RBCs next to the walls.

layer by observing single platelet trajectories. Fig. 9 illustrates that once platelets enter the RBC-free layer, they are unlikely to move back into the main stream of RBCs and most remain trapped near the wall. So, the edge of the RBC-free layer acts as a free-escape boundary for platelets. This free-escape boundary together with RBC-enhanced diffusion of platelets (hereafter referred to as diffusion), are sufficient to create a net drift without imposing an additional drift force.

3.3.2 A continuum model for platelet transport

To test whether platelet margination rate can be accurately modeled by RBC-enhanced shear-induced diffusivity together with a free-escape boundary at the edge of the cell-laden region, average platelet trajectories and platelet concentration profiles from a continuum diffusion model are compared with DNS results. More specifically, the time evolution of platelet concentration is solved by a continuum mass transfer equation in a 1D domain along the y direction in the cell-laden region bounded by a free-escape boundary at the edge of the RBC-free layer:

$$\frac{\partial P(y,t)}{\partial t} = \frac{\partial}{\partial y}\left(D_{yy}\frac{\partial P(y,t)}{\partial y}\right), \quad \delta < y < H - \delta \tag{18}$$

with $P(\delta, t) = P(H - \delta, t) = 0$. Here, P is platelet concentration, $D_{yy}(y)$ is the lateral diffusivity of platelets, and δ is the thickness of the RBC-free layer. The concentration of platelets in the RBC-free layer can be obtained by subtracting the total number of platelets remaining in the cell-laden region from the initial total number of platelets in the domain

$$P_w(t) = \frac{1}{2\delta}\int_{\delta}^{H-\delta}[P(y,0) - P(y,t)]\mathrm{d}y. \tag{19}$$

The diffusion with free-escape boundary (DFEB) model then requires input of a lateral diffusivity, D_{yy} and the RBC-free layer thickness, δ. Note that no additional drift term is added to Eq. 18; the free-escape boundary condition at the edge of the RBC-free layer creates the outward drift of the platelets from the RBC-filled region.

3.3.3 Calculation of RBC-enhanced diffusion of platelets from DNS

The diffusivity of particles is estimated by analyzing single particle trajectories from the DNS model. In flowing blood, the random motion of RBCs and platelets is similar to Brownian motion, and the shear-induced diffusivity of platelets is estimated by assuming that the motion of platelets in blood flow can be estimated as a standard diffusion process. The shear-induced diffusivity can be estimated from mean square displacements of platelets as a function of time (e.g. see [33, 73, 131, 172]). Here, we estimate diffusion coefficient from step sizes and wait times between successive particle collisions from platelet trajectories. Calculating the step size of particle jumps $\Delta y(y)$ and wait times between successive jumps $\tau(y)$ from particle trajectories, the diffusivity

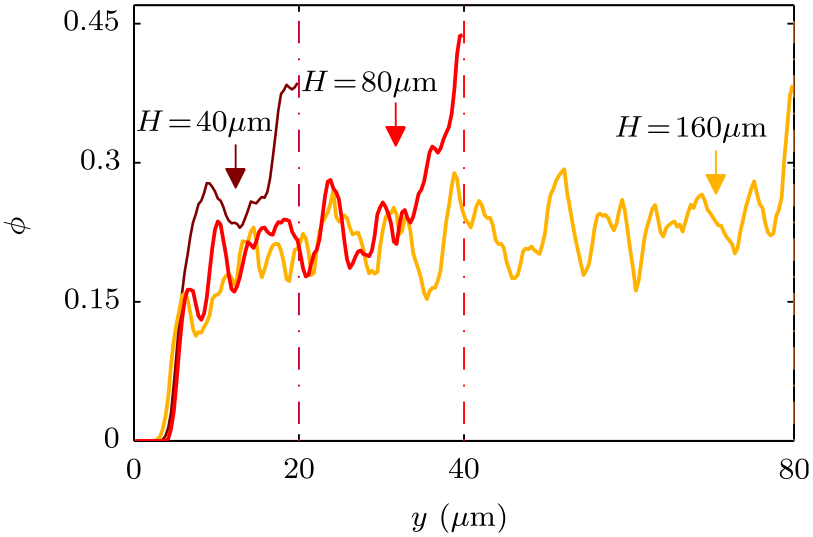

Figure 10: Profiles of hematocrit ϕ at various channel heights H in the cross-channel direction, y. The hematocrit profiles are calculated with $\overline{\phi}(y) = \sum_{i=1}^{n} \phi(t_s + i \times \Delta t, y)/n$, where $\phi(t, y)$ is hematocrit profile estimated by averaging the volume of RBCs along the flow direction x over the channel length L at time t, $\Delta t \sim 1/\dot{\gamma}$ and t_s is the time point at which averaging starts. The time t_s is chosen large enough to ensure that the hematocrit profiles reach a relatively stable configuration. The averaging is performed by setting $n = 5$ to ensure that the averaging of hematocrit profiles is performed over a time scale relevant to the time scale of particle-particle collisions.

in the y direction can be estimated as

$$D_{yy}(y) = \frac{\langle \delta y^2(y) \rangle}{2\langle \tau(y) \rangle}, \tag{20}$$

where $\langle \delta y^2(y) \rangle$ is the time average of variance of the jump step sizes and $\langle \tau(y) \rangle$ is the time average of wait times τ. The calculated values of $\tau(y)$ and $\Delta y(y)$ depend on the time step, Δt, for resolving the particle trajectories. Because our DNS model does not include a stochastic component (e.g. due to Brownian motion), resolving particle trajectories with a time step of the same order as the DNS time step resolves the actual fluctuations of the particles within the accuracy of the DNS model. If the time step for particle trajectories, Δt, is much larger than the actual wait times between jumps, τ, then the estimated $\langle \tau(y) \rangle$ approaches the time step used for resolving the trajectories. Therefore, if particle trajectories are resolved with relatively large time steps, calculating the diffusion coefficient from Eq. 20 is equivalent to calculating it from a linear growth of mean square lateral displacements of particles with time $\langle y^2(t)\rangle = 2tD_{yy}$. We used $\Delta t \sim 1/\dot{\gamma}$ for resolving particle trajectories. The cross-channel profiles of hematocrit show that RBCs form a layered structure (Fig. 10). This configuration is similar to the layered structured observed in suspensions of hard spheres [170] and deformable capsules [139]. This layered structure leads to superdiffusive behavior of hard spheres and deformable capsules near the wall [170, 139]. Platelets may also exhibit anomalous diffusion as they get trapped in RBC layers or rapidly jump through this layered structure. Although there seems to be a complex behavior due to this layered structure of RBCs, we assume platelet motion is governed by a time-averaged standard diffusion for simplification of the DFEB model.

Fig. 11(a) shows the diffusivity of platelets in the cross flow direction calculated from the DNS platelet trajectories for channels of height $H = 40, 80$ and 160 μm normalized by average shear rate $\bar{\dot{\gamma}} = 2\overline{u}/H$. Effective diffusivity of platelets is lowest in the RBC-free region where $\dot{\gamma}(y)$ is highest. The position of the maximum of $D_{yy}(y)$ occurs within $8-13$ μm from the channel wall and slightly shifts away from the wall in the larger channels. Despite the vanishing (time-averaged) shear rate in the channel center, the value of D_{yy} in the channel center is nonzero. This nonzero value is due to the finite size of RBCs and platelets and decreases with H/a.

When D_{yy} is normalized by local shear rate $\dot{\gamma}(y)$ and platelet effective radius a, the data basically collapse onto a single curve except when approaching the channel center where $D_{yy}(y \rightarrow H/2)$ is divided by a vanishing $\dot{\gamma}(y)$ (Fig. 11(b)). This normalized diffusion function first increases sharply in the cell-laden region and then increases with a lower rate as $y \rightarrow H/2$. Shear-induced diffusivity has a functional form of $D_{yy} \sim K\dot{\gamma}a^2$, where K is a nondimensional parameter that is a strong function of hematocrit ϕ and also depend on particle properties such as particle deformability. Thus, the shape of the normalized diffusion function is expected since it is similar to

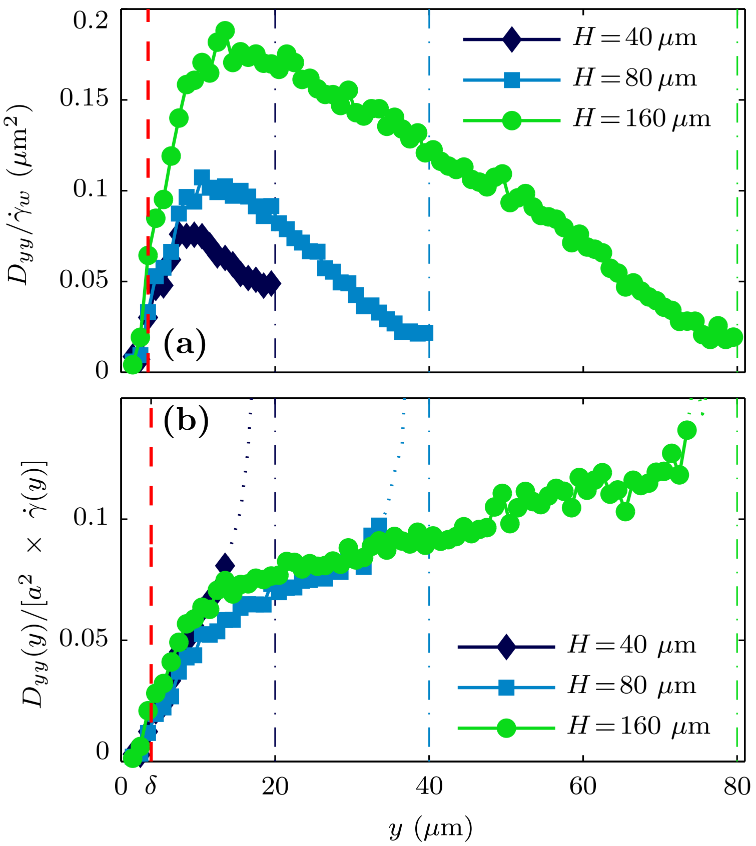

Figure 11: Cross-channel profiles of platelet effective diffusivity D_{yy} calculated from DNS platelet trajectories at various channel heights H. Effective diffusivity is normalized by (a) average shear rate $\overline{\dot{\gamma}}$ and (b) by $a^2 \times \dot{\gamma}(y)$ where a is platelet effective radius and $\dot{\gamma}(y)$ is local shear rate in the cross flow direction, y.

the cross-flow hematocrit profiles, i.e., both increase sharply at the edge of the cell-laden region and then increase with a lower rate as $y \rightarrow H/2$ (Fig. 10). The decrease of $\dot{\gamma}$ towards the channel center also plays a role in the increase of the normalized diffusivity as $y \rightarrow H/2$. While effective diffusivity of rigid spheres in non-colloidal suspensions scales linearly with $\dot{\gamma}$ [81, 103, 131], diffusion scales sublinearly with $\dot{\gamma}$ at Ca < 1 [171, 172].

Direct experimental measurement of diffusion from platelet trajectories is difficult because of the optical properties of blood and the small time and length scales. Experimental values of platelet diffusion in blood are mostly obtained indirectly by analysis of platelet accumulation rates in chambers perfused with blood. Turitto and Weiss [149] used this method to obtain platelet diffusivity including the effects of reaction kinetics of platelet adhesion. They reported diffusion of 22 $\mu\mathrm{m}^2/\mathrm{s}$ at a wall shear rate of $\dot{\gamma}_w = 50\mathrm{s}^{-1}$ ($D/\dot{\gamma}_w = 0.44\ \mu\mathrm{m}^2$), 42 $\mu\mathrm{m}^2/\mathrm{s}$ at $\dot{\gamma}_w = 200\ \mathrm{s}^{-1}$ ($D/\dot{\gamma}_w = 0.21\ \mu\mathrm{m}^2$), and 76 $\mu\mathrm{m}^2/\mathrm{s}$ at $\dot{\gamma}_w = 650\ \mathrm{s}^{-1}$ ($D_{yy}/\dot{\gamma}_w = 0.12\ \mu\mathrm{m}^2$). These values are two to four times larger than our calculated mean platelet diffusivity at $\dot{\gamma}_w = 100,\ 242$ and $503\ \ \mathrm{s}^{-1}$ (i.e., $\overline{D}_{yy}/\dot{\gamma}_w = 0.11,\ 0.061$ and $0.053\ \mu\mathrm{m}^2$ in channels of height $H = 160,\ 80$ and 40 μm, respectively). However, these values were obtained for whole blood, which has higher hematocrit than our numerical simulations that used a hematocrit of $\phi = 0.20$. Recently, Saadatmand et al. [122] measured diffusion by tracking tracer particles in blood flow of hematocrit of 0.20. They obtained diffusion of 1.6 $\mu\mathrm{m}^2/\mathrm{s}$ for 1 μm diameter particles at a flow rate of $\sim 0.033\ \mu\mathrm{L}/\mathrm{min}$ in 50 μm diameter capillary tubes. Assuming $\bar{\dot{\gamma}} \sim 30\ \mathrm{s}^{-1}$, we obtain $D/(\bar{\dot{\gamma}}a^2) \sim 0.21$ which is close to our calculated non-dimensional diffusion values from the DNS particle trajectories (Fig. 11 (b)).

3.3.4 Calculation of the skimming layer thickness from DNS

In addition to D_{yy}, the DFEB model requires the input of the RBC-free layer thickness δ. We estimated δ from the DNS RBC hematocrit profiles after reaching equilibrium such that $\phi(\delta) = 0.005$. We found $\delta \sim 3.5$ and 3.9 μm for channels of height $H = 40$ and 80 μm, respectively. Without aggregating RBCs, most studies suggest that δ increases with $\dot{\gamma}$, if vessel size is fixed [50, 116, 137]. Also, δ increases with vessel size at fixed $\dot{\gamma}$ [48, 50, 66, 116, 137, 167]. Thus, δ should not change significantly if shear rate decreases with channel size such that pseudo-shear rate (i.e. mean flow velocity divided by vessel diameter) remains constant, and RBCs do not aggregate in this flow [67, 116]. Thus, a value of δ that scales with tube diameter should be a reasonable estimate for many channels.

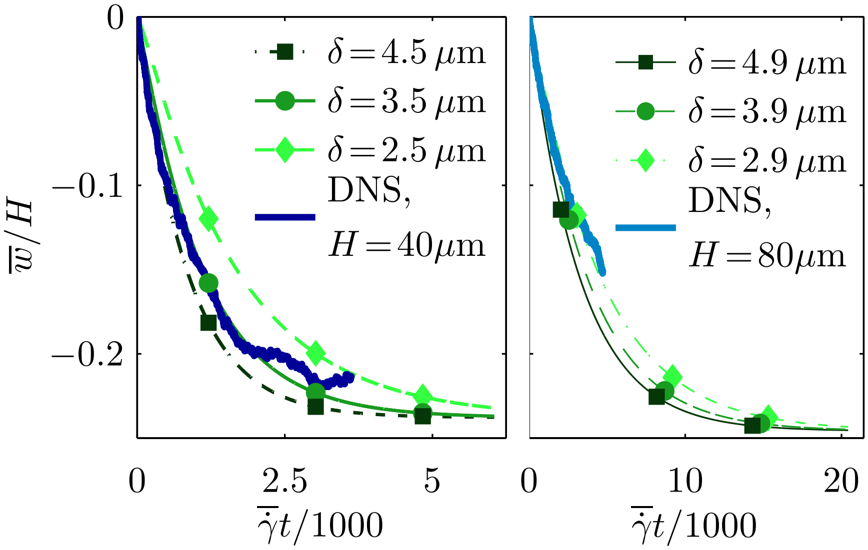

Figure 12: Average relative distance of platelets from the channel wall for two channel heights: $H = 40\ \mu$m (left panel) and 80 μm (right panel). The average relative distance of platelets from wall is defined by $\Delta\overline{w}(t) = \overline{w}(t) - \overline{w}(0)$ where $w(t)$ denotes the distance of platelets from wall $w(t) = H/2 - |y(t) - H/2|$. The average relative distance of platelets from wall $\Delta\overline{w}$ is normalized by channel height, H. The results of the direct numerical simulation (DNS) (thick blue line) are compared with the results of the diffusion with free-escape boundary (DFEB) model with $\delta = 2.9$, 3.9, and 4.9 μm (thin lines).

3.3.5 Comparison of the DFEB results with DNS

To examine whether the DFEB model can recover the margination rates given by the DNS model, Eq. 18 is solved using D_{yy} and δ calculated from the DNS results. The diffusion profiles estimated from the DNS results (Fig. 11(a)) were interpolated by employing Fast Fourier Transform algorithm (using Matlab). We assumed a constant δ value during platelet margination. This assumption is justified by the much shorter time scale for development of the RBC-free layer compared to the platelet margination time scale. Eq. 18 is solved using a finite difference scheme (using Matlab). In addition to the steady state δ values found from the DNS results in the channels of height $H = 40$ and 80 μm (§3.3.4), we compared the DFEB results at $\delta = 3.5 \pm 1\ \mu$m (in channels of height $H = 40\ \mu$m) and $\delta = 3.9 \pm 1\ \mu$m (in channels of size $H = 80\ \mu$m) to study the sensitivity of the DFEB results to the value of δ. The average relative distances of platelets from the wall $\overline{w}$ computed using the DFEB model in channels of height $H =$ 40 and 80 μm are compared with the DNS results in Fig. 12. The rate of platelet margination from the DFEB model equals the outward platelet flux at the edge of the RBC-free layer and so strongly depends on the value of $D_{yy}(\delta)$. This dependence of platelet margination rate on $D_{yy}(\delta)$ together with the large gradient of $D_{yy}(y)$ at the edge of the RBC-free layer (Fig. 11) makes the DFEB model results sensitive to the value of δ.

Fig. 13 shows the time evolution of the platelet concentration profile for a channel of height $H = 80$ μm. The calculated profiles using $\delta = 3.9$ μm is in good agreement with DNS results. In the platelet concentration profiles from both the DNS and the DFEB models, a region with low concentration forms between the center of the

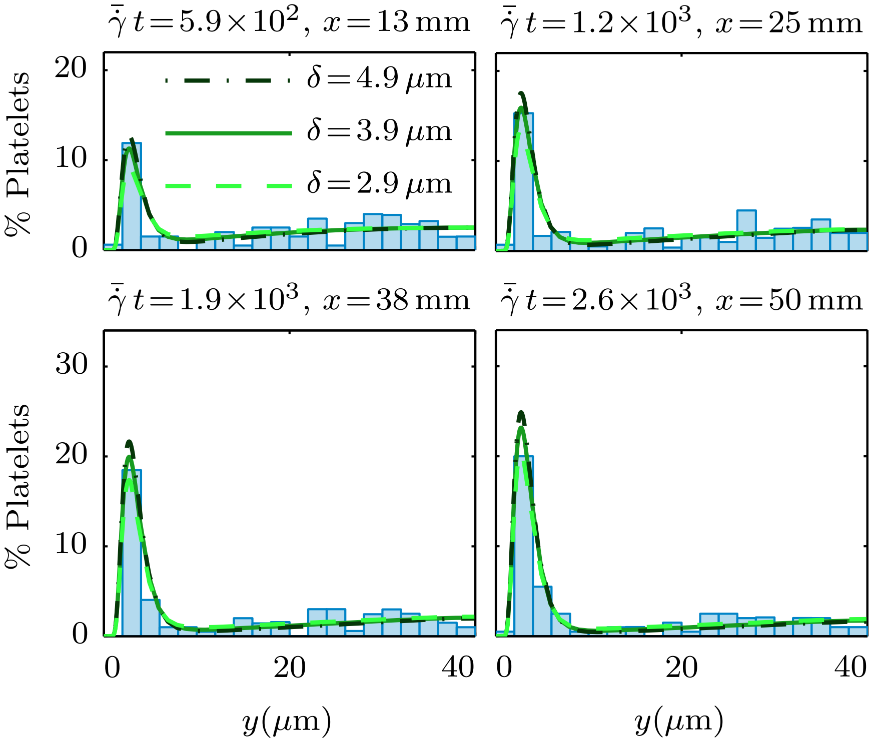

Figure 13: The evolution of platelet concentration profile in the cross flow direction in a channel of height $H = 80$ μm at discharge hematocrit of $\phi_d = 0.27$. The results of the direct numerical simulation (DNS) (histograms) are compared with the results of the diffusion with free-escape boundary (DFEB) model (line plots). The DFEB results are calculated using skimming layer thicknesses of $\delta = 3.9 \pm 1$ μm.

channel and the RBC-free layer. According to the DFEB model, this local dip forms when platelets from this region escape into the RBC-free layer. The concentration gradient resulting from this local dip in platelet concentration further drives the flux of platelets from the channel center towards the walls. Thus, the DFEB captures this subtlety in platelet concentration profile well.

For given values of H and $\dot{\gamma}$, the DFEB model requires the input of D_{yy} and δ to estimate the time evolution of platelet concentration profiles. The $D_{yy}(y)$ for channels of various H can be estimated from the curve obtained in Fig. 11(b). The exact functional form of δ with H and $\dot{\gamma}$ is unknown but may be estimated. The variation in reported values of δ at fixed hematocrits is limited to only a few microns (1-2 μm) within the range of channel sizes considered here [116, 126]. Fig. 12 shows that the predicted average trajectories are less sensitive to the absolute error in the value of δ at larger channels.

3.3.6 Comparison of the DFEB results with experiments

To validate our proposed mechanism for platelet margination, we compared the results of the DFEB model with the experimental results of Waters and Eckstein [156] and Xu and Wootton [164]. To compare the results of the DFEB model with the experimental results of [156] and [164], the diffusion coefficient is set to a constant value. We compared the results of the DFEB model with a constant diffusion coefficient to the results of the DFEB model with a variable profile with a shape similar to the diffusion profiles from DNS. The results of the DFEB model with constant and variable diffusion coefficients are close and the difference between the estimated value of the near-wall platelet concentration from the two models is smaller than the experimental error. Solving the DFEB model with a constant diffusion coefficient is simpler and requires less input parameters (to determine the shape of the profile). We estimated the diffusion coefficient using the experimental correlation by Zydney and Colton [175] for diffusion of deformable suspensions

$$\frac{D_p}{a^2\dot{\gamma}} = k\phi_p(1-\phi_p)^n \tag{21}$$

where $k = 0.15 \pm 0.03$ and $n = 0.8 \pm 0.3$ yields 95% confidence interval curves fitted to experimental results.

Waters and Eckstein [156] obtained developing profiles of concentration of platelet-sized beads in blood using a rapid-capture technique. We considered the experimental case of blood flow with hematocrit of $\phi = 0.30$ at a wall shear rate of $\dot{\gamma}_w = 400\ \ \mathrm{s}^{-1}$ in a 200 μm diameter tube. We estimated the diffusion coefficient using Eq. 21. We set $k = 0.15 \pm 0.03$, $n = 0.8 \mp 0.3$, $\phi = 0.3$ and RBC radius $a_{\mathrm{RBC}} = 2.78$ μm resulting in $D_{rr}/\dot{\gamma}_w = 0.27 \pm 0.08$ μm ^{2}. DFEB is solved using diffusion coefficients of $D_{rr}/\dot{\gamma}_w = 0.27 \pm 0.08$ $\mu\mathrm{m}^2$. The thickness of the skimming layer is set to $\delta = 6$ μm, which approximates the peak widths of the platelet concentration profiles from experiments. The DFEB model estimates of the concentration profiles in the developing regime in good agreement with the experimental results of Waters and Eckstein [156] (Fig. 14).

To determine the applicability of the DFEB model to blood flow in arterial-sized tubes, we compared the predicted values of the DFEB model with the experimental results of Xu and Wootton [164]. Xu and Wootton [164] measured the NWE of platelets in whole porcine blood flowing in 3 mm diameter tubes at wall shear rate of $500\ \ \mathrm{s}^{-1}$. The NWE of platelets was measured by taking local samples through smaller tubes attached to the outer walls of 3 mm diameter tubes. The depth of the sampling region was estimated from the flow rate in the sampling tube relative to the flow rate in the 3 mm diameter tube by using a three dimensional computational fluid dynamics model. We compared the DFEB model to the experimental results of [164] with steady flow. Relative platelet concentration of samples with 20 μm depth were smaller but not significantly different compared to concentration of samples with 50 μm depth. This comparison suggests that the peak width of the platelet concentration profile is larger than 20 μm in 3 mm diameter tubes. We set the skimming layer thickness

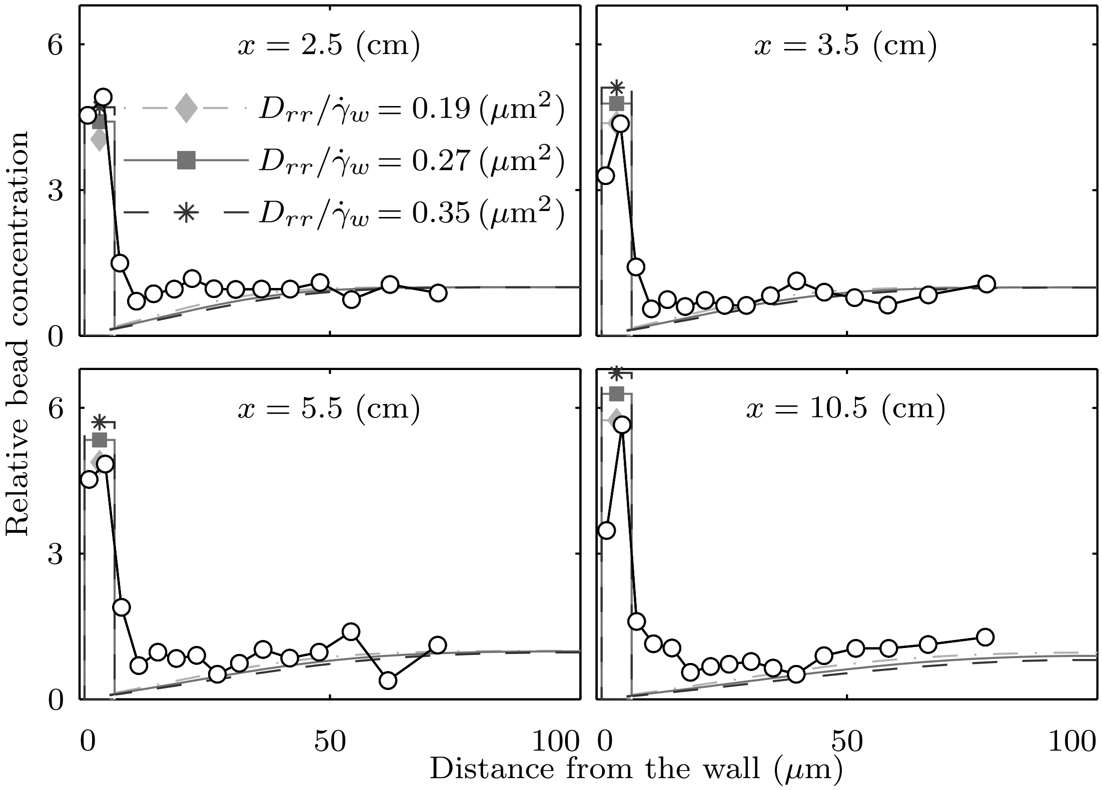

Figure 14: The evolution of bead concentration profile in the cross flow direction in a 200 μm diameter tube at hematocrit of $\phi_d = 0.30$. The results of the diffusion with free-escape boundary (DFEB) model (histograms) are compared with experimental results of Waters and Eckstein [156]. The DFEB results are calculated using skimming layer thicknesses of $\delta = 6$ μm and diffusion coefficient of $D_{rr}/\dot{\gamma}_w = 0.27 \pm 0.08$ μm^2.

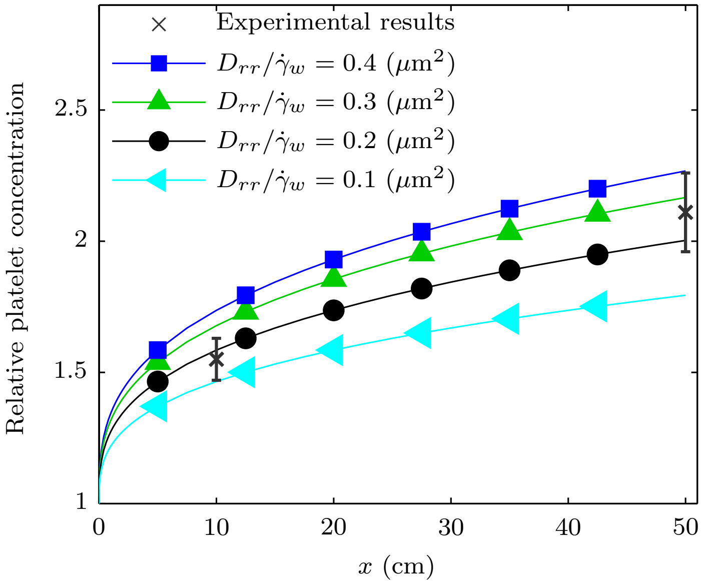

Figure 15: The relative concentration of platelets at the near-wall region in whole blood flowing in 3 mm diameter tubes. The results of the diffusion with free-escape boundary (DFEB) model are compared with experimental results of Xu and Wootton [164]. The DFEB results are calculated using skimming layer thicknesses of $\delta = 50$ μm.

to $\delta = 50$ μm which is relatively consistent with the value of δ set in the 200 μm diameter tubes. The concentration of platelets in the near-wall region relative to the bulk are compared with the DFEB model estimates over a range of diffusion values in Fig 15. The RBC-enhanced shear-induced diffusivity of platelets in porcine blood can be estimated from Eq. 21 by setting $k = 0.15 \pm 0.03$, $n = 0.8 \mp 0.3$, $\phi = 0.5$ and $a_{\text{RBC}} = 2.34$ μm. The radius of porcine RBC, a_{RBC}, is estimated from mean corpuscular volume (MCV) of porcine RBCs using $a_{\text{RBC}} = \left(\frac{3\text{MCV}}{4\pi}\right)^{1/3}$, where MCV is set to 54 fL [159]. Using these values the shear-induced diffusivity of platelets in porcine blood can be estimated by $D_{rr}/\dot{\gamma}_w \sim 0.15 - 0.36$ μm^2. The results of the DFEB with diffusion coefficient within a range of $D_{rr}/\dot{\gamma}_w = 0.1 - 0.4$ μm^2 is almost within the experimental error (Fig. 15).

We applied the DFEB model to blood flow in a 70% stenosed tube. Blood flow rate is $Q = 1$ mL/min in a stenosed tube with a maximum diameter of 3 mm. The DFEB model is solved using a constant diffusion coefficient of $D_{rr}/\dot{\gamma}_w = 0.1$ μm^2.

The skimming layer thickness as a function of distance along the tube is set to $\delta = 0.05R(x)$, where $R(x)$ is the maximum radius of the tube at a given axial coordinate x. The concentration profile at the inlet is obtained from solving DFEB in a straight tube of 5 cm length. The steady state velocity field and the diffusion equation for platelet transport is solved using Comsol 4.4 (COMSOL Inc, MA, USA). The DFEB suggests that the near-wall concentration of platelets increases as blood flows through the stenosed region. The near-wall concentration of platelets downstream of the stenosis is also slightly larger compared to the near-wall concentration at the inlet (Fig. 16). This result is in contrast to the predictions of Bark and Ku [11] who reported dispersion of platelet concentration profile downstream of the stenosis. By extending the model of Hund and Antaki [59], Bark and Ku [11] found that the near-wall platelet concentration reduces at the apex of stenosed tubes.

3.4 Discussion and Conclusion

The irreversible flow of platelets into the RBC-free region can be explained by the low effective diffusivity in this region due to the low local volume fraction of particles (Fig. 11). Thus, the probability of ejection of a platelet from the RBC-free region to the cell-laden region is low due to the infrequent particle collisions. Also, in the RBC-free region, the lift force from the wall on small, stiff platelets is lower than the lift force on RBCs [52]. The lift force from the wall on tank-treading vesicles scales cubically with vesicle size [4]. As rigid platelets may tumble in the RBC-free region, they would experience a much lower lift from the wall compared with tank-treading RBCs [5, 32].

Heterogeneous pair collisions between RBCs and platelets also contribute to the outward motion of platelets into the RBC-free region. In pair collisions between particles of different stiffnesses under shear, the stiffer particle experiences a larger

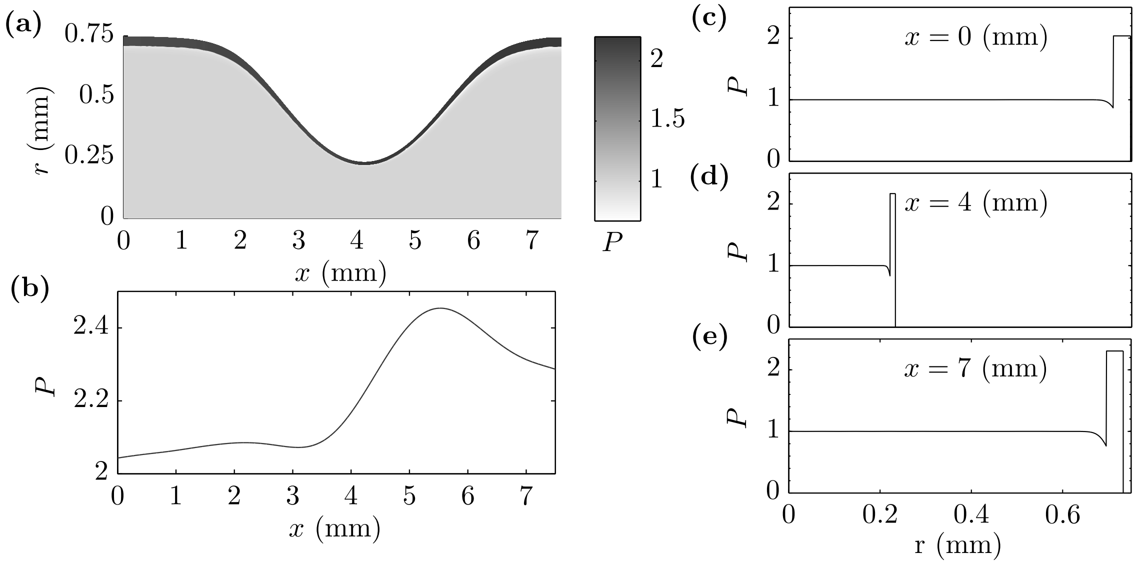

Figure 16: The relative concentration of platelets, P, in whole blood flowing in a 70% stenosis by diameter. The relative concentration profiles are calculated using the diffusion with free-escape boundary (DFEB) model. The left top panel (a) shows the relative platelet concentration across the whole channel. (b) The relative concentration of platelets in the near-wall region as a function of axial coordinate x. The near-wall concentration of platelets increases as blood flows through stenosed section. The right panels show the evolution of platelet concentration profiles (c) at the inlet ($x = 0$ mm), (d) at the apex(($x = 4$ mm), and (e) downstream of the stenosis ($x = 7$ mm).

displacement [72, 74]. In a binary suspension of stiff and floppy particles, the heterogeneity in pair collisions may contribute to the low probability of transition of stiff particles from the near-wall region moving into the channel interior region [72]. Recently, Kumar and Graham [74] have shown that the differences in both migration velocity away from wall and displacements upon heterogeneous pair collisions between stiff and floppy capsules are important in the segregation of binary suspensions of elastic capsules. Both of these mechanisms may dominate particle migration across a large portion of the channel in semi-dilute suspensions flowing in relatively small channels; however, these mechanisms may only affect the dynamics in the near-wall region in the flow of dense suspensions in larger channels.

Crowl and Fogelson [33] performed two-dimensional simulations of cellular blood flow and proposed a local effect leading to platelet margination. Crowl and Fogelson estimated platelet margination using a drift-diffusion equation similar to the approach of Eckstein and Belgacem [39]. With the drift and diffusion functions estimated from platelet trajectories, the drift-diffusion model underestimated the platelet margination rate by their cellular (DNS) blood flow simulations. To recover the results of the DNS cellular flow simulations, an additional drift term localized at the edge of the RBC-free was required. The authors hypothesized that the orientation angle of tank-treading RBCs at the edge of RBC-free layer may influence the motion of platelets at this region leading to a localized drift.

The DFEB model is based on the hypothesis that platelet margination is due to the irreversible flow of platelets into the RBC-free layer. A similar mechanism may also lead to the NWE of large proteins and macromolecules. For smaller sized molecules and particles, the RBC-enhanced shear-induced diffusion is comparable to Brownian diffusion; therefore, the RBC-free layer may not act as a free-escape boundary for such particles.

The DFEB model can predict platelet concentration profiles over a wide range of tube diameters. The DFEB model is similar to the drift-diffusion model of Eckstein and Belgacem [39]; however, the advantage of this model is that it does not rely on *a priori* knowledge of platelet concentration profiles. The diffusion-drift model is sensitive to the drift function form and magnitude, and small changes in the drift term can lead to large changes in the results of such models [33]. Also, the DFEB model can model platelet transport in the developing regime. Experiments suggest that the margination development length is of the same order as the lengths of arteries [156, 164]. Furthermore; angiographic and postmortem studies of coronary arteries have shown that the majority of vulnerable plaques are located in the proximal portions of coronary arteries [27, 153].

The DFEB model can be easily implemented in arbitrary geometries. The variation of the RBC-free layer thickness and RBC dynamics due to flow acceleration through stenotic regions or bifurcated pulsatile secondary flows may affect platelet transport in such regions. Note that we have only validated the DFEB model in straight tubes. The validation of the DFEB model in complex geometries requires further investigation through experimental studies of platelet transport in such geometries.

In conclusion, the DFEB model is developed based on the hypothesis that the dominant mechanism for platelet margination is the RBC-enhanced shear induced diffusion of platelets with a free-escape boundary at the edge of the cell-laden region. With the diffusion coefficient estimated from DNS model, the DFEB model can match the DNS results for platelet margination rate. The DFEB model provides a much simpler method for estimating platelet concentration profiles that is significantly faster computationally compared with the DNS of blood flow. Using diffusion coefficients obtained by experiments the DFEB model can capture the margination levels observed in experiments. Instead of introducing drift, source or flux terms, we impose a free-escape boundary condition at the edge of the skimming layer. This boundary condition is based on our observations of the DNS trajectories. Our proposed model is simpler than previous continuum models proposed for predicting margination and requires fewer inputs, and yet it improves over previous models since its results are in good agreement with experimental results of margination in the transient regime over a wide range of tube sizes. Thus, our proposed model would be useful in modeling complex processes which involve transport of particles in blood.

CHAPTER IV

EFFECT OF RBCS ON RAPID THROMBUS FORMATION UNDER HIGH SHEAR

4.1 Introduction

Upon rupture or erosion of a plaque, a platelet-rich thrombus can rapidly grow and may occlude an artery. An occlusive thrombus is the most common cause of clinical events such as angina, myocardial infarction, ischemic attacks and strokes. Identifying the rate limiting processes in thrombus growth may lead to developing better treatments for cardiovascular disease.

Platelets play an important role in thrombus formation at high shear. Platelet transport to the surface of a growing thrombus is suggested to limit thrombus growth rate at high pathophysiological shear rates [11, 79, 162]. Platelet transport in flowing blood is greatly affected by red blood cells (RBCs). In flowing blood, RBCs enhance the rate of platelet transport to the wall by enhancing platelet effective diffusivity [53, 175]. In addition to effective diffusivity, under arterial flow conditions, RBCs migrate away from the walls, and platelets marginate to the RBC-free layer formed near the walls. RBCs lead to platelet margination or platelet near-wall excess (NWE) [3, 14, 106, 141, 142].

In vitro studies on the rate of platelet adhesion on subendothelium have shown that platelet adhesion is minimal without RBCs and increases with increasing hematocrit [1, 2, 147, 148]. These experimental studies have led to the general view that rapid thrombus formation at high shear requires the presence of RBCs. But recent *in vitro* models of high-shear thrombosis have shown that the rate of platelet adhesion to a thrombogenic surface is slow compared to the thrombus growth rate after a lag time of the order of few minutes [57, 71, 101, 108]. The effect of the RBCs on platelet adhesion during the initial slow phase may differ from their effect on thrombus growth rate during the rapid growth phase.

Based on computational models of thrombus formation [11, 79, 162] and *in vitro* experiments of platelet adhesion on subendothelium [1, 2, 147, 150], we hypothesize that thrombus formation at high shear is limited by platelet transport and therefore requires the presence of RBCs.

Our aim was to investigate the effect of RBCs on rapid thrombus growth at high shear. We used an *in vitro* model for thrombus growth in stenosed vessels. To investigate the effect of upstream margination on rapid thrombus growth, we compared thrombus growth rate in stenoses with an entrance length to those with no entrance length. We also, investigated the effect of RBCs on rapid thrombus growth by comparing growth rate in whole blood (WB) *vs.* platelet-rich plasma (PRP).

4.2 Methods

4.2.1 Blood

Whole porcine blood was obtained from a local abattoir (Holifield Farms, Covington, USA). Blood was collected immediately after electrical stunning and lightly anticoagulated with 3.5 USP units/mL of Heparin. Perfusion experiments were performed within 6 hours of obtaining blood. Prior to experiments, large clots and aggregates were removed from whole blood and platelet rich plasma by filtering with a polypropylene mesh sheet with 149 μm pores (Small Parts, USA).

4.2.2 In vitro thrombus model

We studied thrombus formation with an *in vitro* flow system described by Para and Ku [109]. A syringe pump (KD Scientific Inc, USA) perfused whole blood or platelet-rich plasma through the test section at constant flow rate. The test sections were glass capillaries with hour-glass shaped regions fabricated by a professional glass blower. The degree of diameter stenosis (hereafter stenosis) used in this study ranged from 69%-72%. The maximum inner diameter of the glass capillaries was 1.5 mm. The apex of the stenosis was 5 cm downstream of the inlet of the glass capillary tube except for the cases with no entrance length. To study thrombus formation with no entrance length, the glass capillaries were scored and cut at the apex of the stenosis. The cut capillaries were held directly at the inlet of a 20 mL open-ended syringe barrel (Merit Medical, South Jordan, USA) with a clear cap molded from polydimethylsiloxane (PDMS). To coat the surface of the stenotic region, the glass capillaries were incubated with 0.2 mg/mL collagen (type I) solution overnight. Prior to the experiments, collagen solution was washed by perfusing PBS buffer through the flow system.

WB or PRP flowed at constant rates which yielded initial wall shear rates of $\dot{\gamma}_w = 1500 - 6000\ \mathrm{s}^{-1}$ at the apex of the stenoses. Thrombus growth in porcine blood is fastest at $\dot{\gamma}_w = 6000\ \mathrm{s}^{-1}$ [12] below which thrombus growth is estimated to be transport limited [11]. We selected the above range of wall shear rates to span the transport limited regime of thrombus formation at high shear conditions. Flow rate, Q, was estimated using a modified Poiseuille equation:

$$Q = \frac{\pi}{4K} r_a^3 \dot{\gamma}_w(r_a) \tag{22}$$

where r_a is the stenosis radius at the apex, and K is a nondimensional factor to account for the non-straight geometry of the test section. By computational modeling of the flow in the test section using Comsol 4.4 (COMSOL Inc, MA, USA), we estimated $K \sim 1.3$.

Thrombus formation was monitored using a stereo microscope (Stemi 2000-C, Carl Zeiss Microscopy LLC, Thornwood, NY, USA). Glass capillaries were embedded in glycerol or PDMS to reduce optical distortion due to the round shape of the glass capillaries. Images were captured at a rate of 10 frames per second. Images and pressure data were recorded using LabVIEW (National Instruments Corporation, Austin, TX, USA).

4.2.3 Image processing

To analyze thrombus formation, we developed an image processing program in Matlab (Mathworks Inc., Natick, MA, USA) to detect the edges of the thrombi in the captured images. The algorithm of the image processing program is outlined in figure 4.2.3.1. The green channel of the images captured from WB experiments provided the greatest contrast and was used for calculating image intensities. The image intensity for PRP experiments was calculated using the blue channel of the images. To reduce noise from the variations in light intensity, image processing was performed on averaged images in sets of 5. To find the thrombus edges, a rectangular region of interest (ROI) centered around the apex of the stenosis was selected from the reference image at time $t = 0$. To correct for the small relative motion of the glass capillaries during the experiment, the ROI of an image at $t > 0$ was selected using the location of the maximum of the normalized cross-correlation matrix between the image at t and the reference image at time $t = 0$.

Finding the thrombus edge required contrast enhancement of the images by adjusting image intensities. For more effective contrast enhancement, the area for intensity adjustment was limited to the region inside the glass capillaries. To find this region, the location of the inner edges of the glass capillary was found by converting the intensity image to a binary image and applying a modified Moore-Neighbor tracing algorithm implemented in the Matlab Image Processing Toolbox. The location of the edges of the glass capillaries in the images from PRP experiments was estimated by fitting a smoothing spline to the points with lowest intensity in the images. With the approximated locations of the inner edges of the glass capillaries, the region for intensity adjustment was set to the area inside the glass capillaries. The intensity adjustment was then performed by dividing this region into one-pixel wide bands

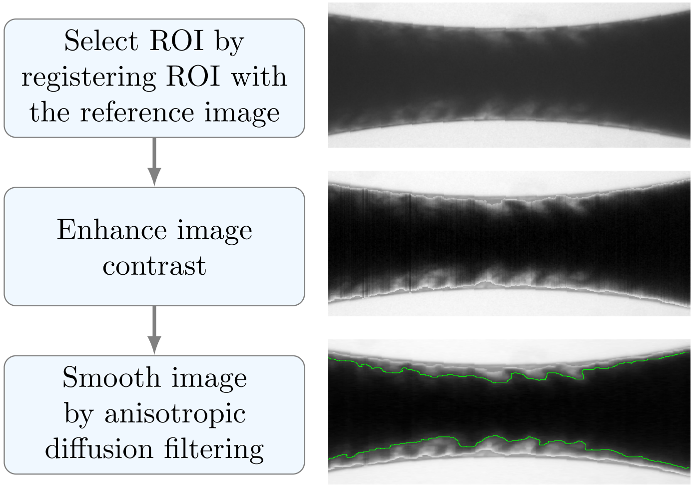

Figure 17: Image processing algorithm

normal to the flow direction. This method resulted in enhanced contrast by using the minimum and maximum intensity values found along each for mapping the intensity values. The enhanced images were smoothed by anisotropic diffusion filtering. This filtering method reduces noise in an image while preserving the edges. We used the Image Edge Enhancing Coherence Filter Toolbox provided by [69, 70] on the Matlab File Exchange website Finally, the edges of the thrombus in the enhanced image were detected with the same method described above for detecting the edges of the glass capillaries from the intensity values of the raw images.

4.2.3.1 Thrombus volume calculation

From the detected edges of the thrombus, the volume of the blood-filled region at time t, $V_B(t)$, can be estimated as

$$V_B(t) = \int_{z=z_i}^{z=z_e} \frac{\pi}{4} D_T(z,t)^2 \mathrm{d}z \tag{23}$$

where $D_T(z,t)$ is the inner diameter of the thrombus at time t at the position z estimated from the detected edges of the thrombus (Figure). The integration is is performed in the flow direction z, (over the interval $z_i < z < z_e$). The volume of the thrombus at time t, $V_T(t)$, can be estimated as $V_T(t) = V_B(0) - V_B(t)$. In glass capillaries with no entrance length, thrombus volume is measured over a 0.7 mm section located 0.1 mm downstream of the inlet. By computational modeling of the flow in the test sections with no entrance length using Comsol 4.4 (COMSOL Inc, MA, USA), we found that within a length of 0.1 mm, the wall shear rate $\dot{\gamma}_w$ develops to the desired value of $\dot{\gamma}_w$ with flow rate Q calculated from Equation 22. In glass capillaries with an entrance length, thrombus volume is defined as the average of volume over 0.7 mm sections upstream and downstream of the apex of the stenosis. We define lag time t_{Lag} as the time when the rate of change of thrombus volume increased to half of its value at the final minute of the experiment. Thrombus formation rate is defined as the mean slope of thrombus volume as a function of time in the rapid growth phase (i.e., from t_{Lag} to the end of the experiment).

4.2.4 Statistical analysis

Statistical analysis was performed by Student's t-test for paired groups. A p value of less than 0.05 was considered to indicate statistical significance.

4.2.5 Histology analysis

Thrombus samples were carefully removed immediately after experiments, and samples were fixed in 10% buffered formalin solution (VWR Scientific, Radnor, PA, USA) for 48 hours. Samples were dehydrated, embedded in paraffin and sectioned (5 μm thick) and stained following Carstair's method to distinguish platelets and RBCs [127].

4.3 Results

4.3.1 Enhanced thrombus growth rate with no entrance length

WB was perfused at initial wall shear rates of $\dot{\gamma}_w = 1500$, 3000 and 6000 s^{-1} in stenoses with and without upstream development. Representative microscopy images of thrombus formation in glass capillaries perfused with WB are shown in Figure 18.

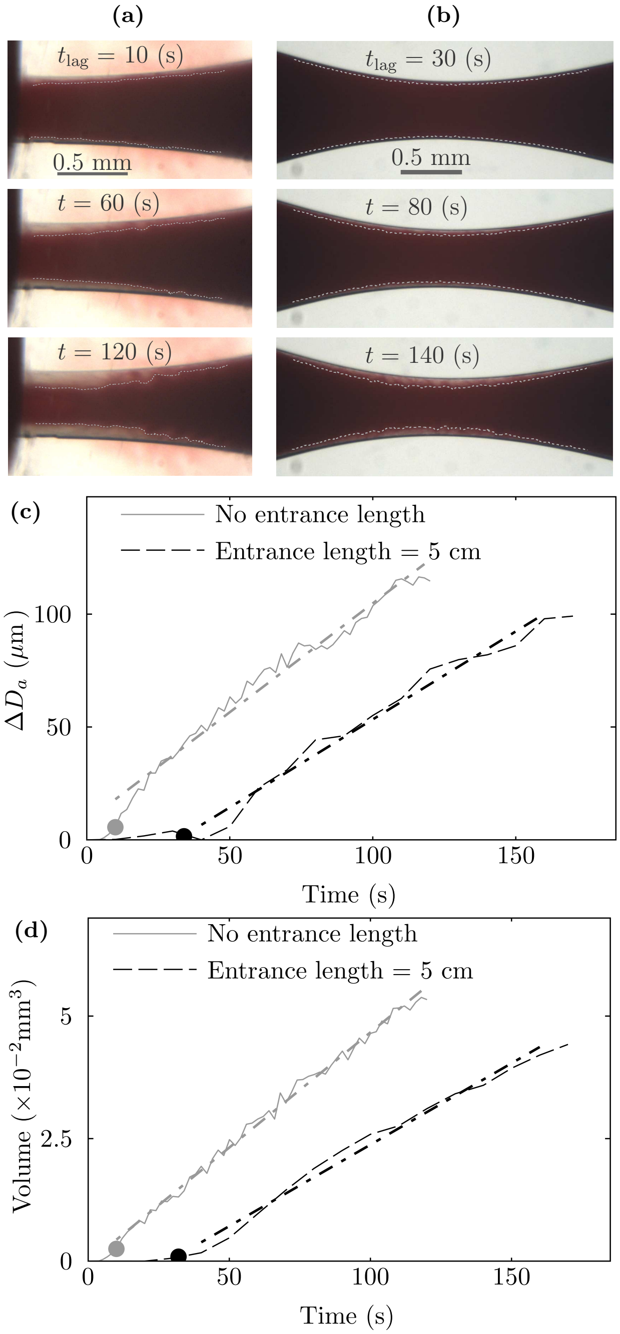

Figure 18: Representative microscopy images of thrombus formation in glass capillaries perfused with whole blood at initial wall shear rate of $\dot{\gamma}_w = 6000\ \text{s}^{-1}$ with (a) no entrance length and (b) with no entrance length. (c) Change of lumen diameter at the apex of the stenosis, $\Delta D_a(t) = D_a(t) - D_a(0)$, as a function of time. (d) Thrombus volume as a function of time for the cases shown in panels (a) and (b). Thrombus volume for the case with no entrance length is measured over a 0.7 mm section located 0.1 mm downstream of the inlet. Thrombus volume values reported for the case with entrance length is the average of volume over 0.7 mm sections upstream and downstream of the apex of the stenosis.

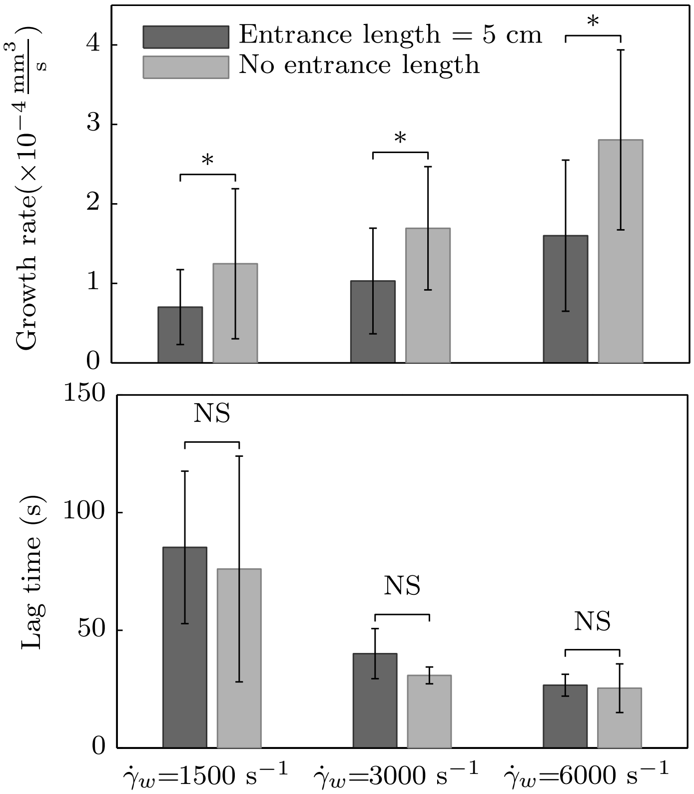

Figure 19: Effect of entrance length on thrombus growth rate (top panel) and lag time (bottom panel). Entrance length had no significant (NS) effect on lag time; however, thrombus grew significantly faster ($* : p < 0.02$) in stenoses with no entrance length. The results indicate that entrance length is not necessary for rapid thrombus formation. The results are shown for $n = 6$ at each condition.

Thrombus formation was slow at the beginning, but entered a rapid formation phase after a short lag time (Figure 18(c)) . Entrance length had no significant effect on lag time; however, thrombus grew significantly faster ($p < 0.02$) in stenoses with no entrance length (Figure 19).

4.3.2 RBCs are not required for rapid platelet accumulation

We studied the effect of RBCs on thrombus growth rate by perfusing WB and PRP at initial wall shear rates of $\dot{\gamma}_w = 2000$, and 6000 s^{-1} in stenoses with and without upstream development. Representative microscopy images of thrombus formation in glass capillaries perfused with WB and PRP are shown in Figure 20. The onset of rapid thrombus growth regime was delayed without the presence of RBCs; however,

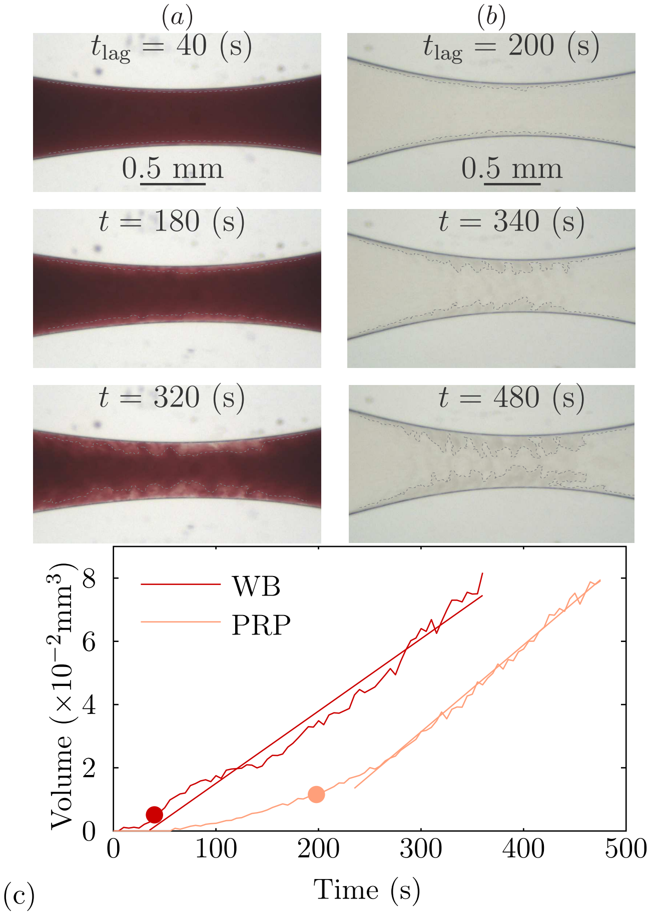

Figure 20: Representative microscopy images of thrombus formation in glass capillaries perfused with (a) whole blood (WB) and (b) platelet-rich plasma (PRP) at initial wall shear rate of $\dot{\gamma}_w = 6000\ \text{s}^{-1}$. (c) Thrombus volume as a function of time for the cases shown in panels (a) and (b). Filled circles represent lag time t_{Lag} for each case.

thrombus started to grow rapidly after a relatively long lag time (Figure 20(c)). In the rapid phase regime, the effect of the absence of RBCs on thrombus growth rate was not significant (NS); however, the absence of RBCs significantly delayed the onset of rapid thrombus growth ($*\, p < 0.02$). The results indicate that RBCs are not necessary for rapid thrombus formation (Figure 21). We performed histology analysis of thrombi formed under WB and PRP. The absence of RBCs does not substantially change the structure and composition of the thrombus (Figure 22).

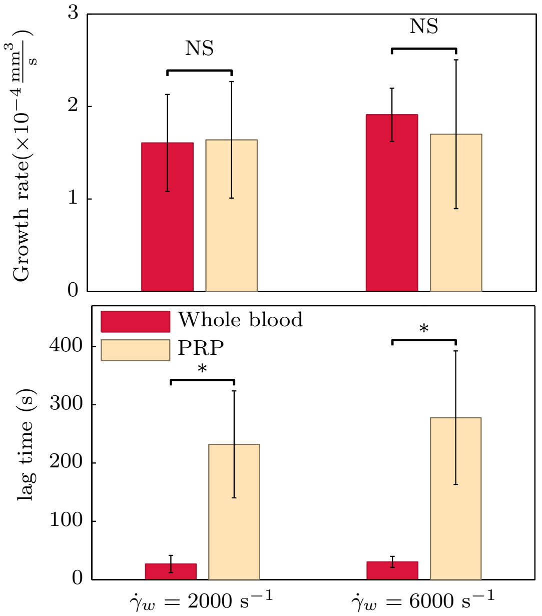

Figure 21: Effect of RBCs on thrombus growth rate (top panel) and lag time (bottom panel). RBCs had no significant (NS) effect on thrombus growth rate in the rapid phase regime; however, the presence of RBCs significantly reduced the onset of rapid thrombus growth ($* : p < 0.001$) in stenoses with no entrance length. The results indicate that entrance length is not necessary for rapid thrombus formation. The results are shown for $n = 6$ at each condition.

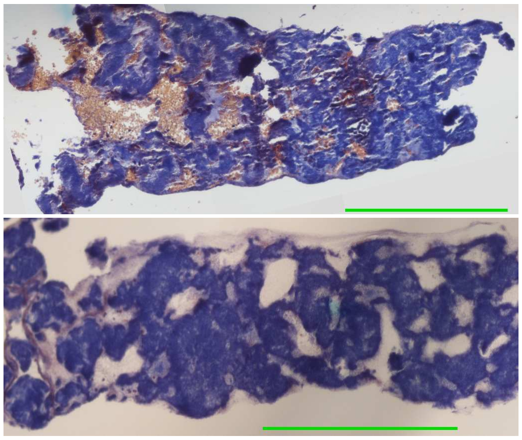

Figure 22: Representative microscopy images of thrombus formed with whole blood (top panel) and platelet-rich plasma (bottom panel) with Carstair's staining. Platelets: gray-blue to navy; fibrin: red; red blood cells: yellow; collagen: bright blue. Scale bars represent a length of 0.5 mm. The absence of RBCs does not substantially change the structure and composition of the thrombus.

4.4 Discussion

The purpose of this study was to study the effect of RBCs on thrombus formation under high shear conditions. RBCs enhance platelet transport rate in flowing blood by enhancing platelet diffusivity and increasing near-wall platelet concentration. We found that thrombus grows faster in stenoses without upstream entrance length. This result indicates that upstream platelet margination is unnecessary for rapid growth of occlusive thrombi at high shear rates. Furthermore, we found that RBCs are not needed for rapid thrombus growth thrombus growth rate, while RBCs only reduce the time for rapid thrombus growth onset.

Previous experimental studies with similar conditions to this study but with short perfusion time, have found a positive correlation between the rate of platelet adhesion on subendothelium and hematocrit [1, 2, 147, 150]. We can find a similar trend in our study, if we compare initial growth rate between WB and PRP (e.g., by defining growth rate as the slope of the a line fitted to the thrombus volume curve from $0 < t < 200\,\mathrm{s}$ in Figure 20(c)). But we found no significant difference between the thrombus growth rate in the rapid growth phase after the initial lag time between WB and PRP. Cadroy and Hanson [21] investigated the effect of hemodilution on thrombus formation on collagen at $\dot{\gamma}_w = 500 - 750\ \mathrm{s}^{-1}$ with long perfusion times. They found a positive correlation between platelet deposition onto collagen after 5 min, but not at later time points (10 - 30 minutes). Ogawa et al. [105] recently showed that, in a microchip-basedflow-chamber system, hemodilution delayed the onset of rapid thrombus formation and increased the the total time for occlusion (defined as the time for pressure to increase to 80 kPa). The longer occlusion time, $t_{\mathrm{occlusion}}$ after hemodilution may be due to the longer lag time, t_{Lag}, but the effect of hemodilution on the time from onset of rapid formation to occlusion, $t_{\mathrm{occlusion}} - t_{\mathrm{Lag}}$, was not reported. Lag time or the total time for occlusion may be more important for treating a patient for major bleeding, the time for occlusion after the onset of rapid thrombus formation, $t_{\text{occlusion}} - t_{\text{lag}}$, may be more important for treating a patient with cardiovascular disease as it may determine response time after initial warning symptoms. Apart from ischemia, bleeding is the most frequent complication in the management of acute coronary syndrome [55]. Thus, it may be important to distinguish how different processes and mechanisms affect t_{Lag} and $t_{\text{occlusion}} - t_{\text{lag}}$, especially for treating cardiovascular patients.

Faster growth of thrombus without entrance length, L, may seem surprising, especially considering the $\approx$ 10-fold increase of near-wall concentration of platelets in tubes of diameter $D = 3$ mm reported by Aarts et al. [3]. But this drastic increase of near-wall concentration is defined relative to that at the core. Yet compared to the bulk concentration, the near-wall platelet concentration is increased by $\approx$ 2-fold. This 2-fold increase of near-wall platelet concentration may not even occur over physiologically relevant lengths. Aarts et al. [3] measured concentration profiles of platelets at $L \approx 55$ cm from the blood container. Xu and Wootton [165] found that near-wall platelet concentration in tubes of $D = 3$ mm perfused with whole porcine blood is doubled in steady flow at $L = 50$ cm from the blood reservoir, but only increased by $\approx$ 1.5-fold at $L = 10$ cm. Coronary angiography of patients with ST-elevated myocardial infarction has shown that most occlusions cluster within the proximal third of major coronary arteries (50% of occlusions in the right coronary arteries occurred within the first 45 mm, 90% of occlusions in the left anterior descending arteries occurred within the first 40 mm, and 50% of occlusions in left circumflex artery occurred within the first 25 mm) [153]. Histological analysis of autopsied human hearts confirms that most ruptured plaques and thin-capped fibroatheroma cluster in the proximal sections of these major coronary arteries [27]. Moreover, margination development length is a strong function of channel size. While the near-wall platelet concentration is approximately doubled in tubes of $D = 3$ mm over $L = 50$ cm, the near-wall concentration of platelet-sized beads is doubled over $L = \lesssim 5$ mm in tube of

$D = 200\mu$m perfused with 30% hematocrit RBC suspension [156]. Zhao et al. [173] reported margination development length of $\lesssim$ 2.5 mm in 100 μm squared channels perfused with 40% hematocrit RBC suspensions. Thus, the near-wall platelet concentration in a stenosis without entrance length may be slightly smaller than that of a stenosed section with entrance length.

Nevertheless, we should see a decrease rather than an increase in thrombus growth rate in stenoses without entrance length if platelet transport limits thrombus growth rate. In addition to platelets, von Willebrand factor (vWF) plays an important role in thrombus formation at high shear rates [118, 121, 119, 120]. Thrombus formation at high shear rates initiates by absorption and immobilization of vWF to exposed collagen fibrils. Globular vWF in plasma bind to collagen types I and III through vWF-A3 domain, and subsequently undergo a conformational change at high shear resulting in elongation and exposure of vWF-A1 domains [124, 31]. Absorption of vWF onto collagen is essential for thrombus formation at high shear, since only bonds between vWF-A1 and platelet glycoprotein receptor GPIbα can form fast enough to capture platelets. Without vWF, platelets cannot directly bind to collagen at $\dot{\gamma} \gtrsim 1000$ s^{-1} [44, 104, 123, 132]. Instead of platelet transport, the availability of vWF-A1 domains may limit thrombus growth rate at high shears. At the inlet of the stenoses without entrance length, the higher shear rates and shear rate gradients may enhance the unfolding of globular vWF in plasma [124] and immobilized vWF on the surface [31] and increase the available A1 domains for platelet capture.

Results of our experiments with whole blood and PRP is consistent with the hypothesis that thrombus growth rate is limited by the availability of vWF-A1 domains instead of platelet transport. We found that the presence of RBCs reduces the onset time of rapid thrombus growth, but, under the same flow conditions, the difference between growth rate with whole blood and PRP was not statistically significant. In the presence of RBCs, platelet transport is orders of magnitude larger compared to transport due to Brownian diffusion. Therefore, if we assume thrombus growth rate is limited by platelet transport to the surface, we cannot explain the comparable thrombus growth rate with PRP and whole blood under the same flow conditions. On the other hand, if we assume that thrombus growth rate is limited by the degree of availability of vWF-A1 domains, we can explain the delayed onset of rapid thrombus growth after a few minutes of perfusion with PRP. Platelets captured and held at the wall may activate after a few minutes of exposure to high shear stress. These activated platelets may release vWF and increase the local concentration of vWF by an order of magnitude [158] due to the high concentration of vWF in platelet α-granules [56]. The increased local concentration of vWF may increase the availability of vWF-A1 domains at the wall.

The absence of RBCs delayed the onset of rapid thrombus growth. In whole blood, RBC-enhanced platelet transport leads to fast release of vWF from activated platelets at the wall. But, perhaps more importantly, RBCs may also enhance the transport of plasma vWF and induce near-wall excess of vWF in whole blood. RBC interactions in flowing blood results in local velocity fluctuations and a random walk or shear-induced diffusion of the particles, $D_{\dot{\gamma}}$. Therefore, in flowing blood the effective diffusion of particles, D_e, is greater than diffusion under stationary conditions, D_{ST}, i.e., $D_e = D_{\dot{\gamma}} + D_{\mathrm{ST}}$. Transport augmentation is defined as $A = D_e/D_{\mathrm{ST}} - 1 = D_{\dot{\gamma}}/D_{\mathrm{ST}}$. Shear-induced diffusivity $D_{\dot{\gamma}}$ depends on hematocrit, RBC size and shear rate but not on particle size; however, stationary diffusion D_{ST} is inversely proportional to particle size. Therefore, under same flow conditions, transport augmentation of blood particles A increases with particle size [23, 65, 154, 175]. In flowing whole blood, the effective diffusivity of platelets is orders of magnitude greater than stationary transport due to Brownian diffusion. Globular vWF in plasma has about the same size of platelet (i.e. $d \approx 2\,\mu\mathrm{m}$ [124]); therefore, vWF transport may also be greatly enhanced in flowing whole blood. The enhanced transport of vWF in whole blood compared to PRP may explain why the absence of RBCs delayed the onset of rapid thrombus growth.

Experiments of Neeves et al. [101] supports our interpretation that vWF transport limits rapid transport formation. Neeves et al. [101] investigated the association of platelet accumulation in microfluidic flow assays within the normal population with VWF plasma level, hematocrit, sex, platelet count, variants of GP6, ITGA2, and GP1BA genes, and experimental conditions including collagen surface density, sodium citrate, and assay time. Among these parameters, vWF plasma level was the strongest determinant of platelet accumulation on collagen type I. They also found weak (not statistically significant) negative correlation between hematocrit and platelet surface coverage. Tomokiyo et al. [146] found that addition of vWF (vWF/factor VIII complex or purified vWF) to platelet-reduced blood (5×10^4 platelets/μL) restores platelet adhesion to a collagen coated surface under flow. Ogawa et al. [105] showed that haemodilution (40% by saline) delayed the onset of rapid thrombus formation in a microfluidic system at shear rate of 1100 s^{-1}, but adding vWF after dilution restored thrombus formation rate to the normal level. Ruggeri [119] measured platelet adhesion to a surface coated with immobilized vWF perfused with whole blood at $\dot{\gamma}_w = 1500\ \text{s}^{-1}$. Platelet adhesion to the vWF coated surface was unaffected after reducing platelet count to 10% (from 325×10^5 to 37×10^4 plateletsμL). Only a further reduction of platelet count to $\approx 2\%$ limited platelet adhesion.

The limitations of this study are as follows. We performed our experiments under steady flow conditions. Our group recently showed that, in our *in vitro* thrombus model, the difference between growth rate and lag time under pulsatile flow and steady flow is not statistically significant [22]. A single-pass flow system with physiologically relevant dimensions requires large volumes of blood; therefore, we used porcine blood instead of human blood. Previous studies suggests that thrombus formation in porcine blood is similar to that of human blood [109]. Lag time in porcine blood is about half of human blood, and growth rate is about twice faster than that of human blood [109]. Smaller porcine RBC size (effective radius of 2.34 μm) compared to human RBCs (effective radius of 2.78 μm) may lower transport augmentation in porcine compared to human blood. We lightly heparinized porcine blood to prevent coagulation. Heparin may reduce thrombin generation and fibrin formation during thrombus growth. In our *in vitro* thrombosis system, we modeled the surface of a ruptured plaque by a smooth rigid surface uniformly coated with collagen. The exposure of subendothelium components may differ from our idealized model. In particular, the increase of vWF concentration at the wall due to the release of vWF from damaged endothelial cells may be larger than the increase of vWF concentration released from activated platelets or (marginated) plasma vWF.

In summary, our study shows that enhanced platelet transport in the presence of RBCs is not necessary for rapid thrombus growth at high shear. RBCs shorten the lag time of rapid thrombus growth. Our results suggests that the availability of vWF-A1 domains may limit thrombus growth rate at high shear. Identifying the rate limiting processes in thrombus growth may help in developing methods for preventing occlusive arterial thrombosis.

CHAPTER V

A PREDICTIVE MODEL FOR THROMBUS FORMATION RATE BASED ON LOCAL SHEAR RATE

5.1 Introduction

Formation of occlusive thrombi upon rupture or erosion of atherosclerotic lesions underlies most cases of myocardial infarction and strokes. This unpredictable and sudden event makes atherosclerosis a potentially life-threatening disease. Prevention of unwanted thrombosis is also one of the greatest challenges in the design of cardiovascular devices [8, 117]. Computational models of thrombus formation based on patient-specific data could aid physicians in determining vulnerability of atherosclerotic lesions. In addition, computational methods for thrombus formation could aid cardiovascular device manufacturers in developing safer devices while reducing development times and costs.

Thrombus formation is a complex process that depends on fluid mechanic conditions, blood thrombogenicity, and surface chemical properties. Several studies have attempted to develop models for predicting thrombogenicity and thrombus formation (see [28, 155, 166] for recent reviews). However, because of the complexities involved in the thrombus formation process, current predictive models for thrombus formation still have limited practical applicability [28]. There is a need for an efficient, validated model for thrombus formation. Such a model should be as simple and efficient as possible to be practical, yet it should be capable of predicting thrombus formation well. In this study we attempt to develop such a model. We extend the study of Bark et al. [12] by obtaining correlations for thrombus growth and lag time based on flow parameters by using an *in vitro* model of thrombosis. We extend a model introduced by Bark [9] to develop a simple model for predicting thrombus formation using the obtained empirical correlations. We then used the model to predict occlusion times in a platelet function analyzer (PFA-100$^{\mathrm{TM}}$), a microfluidic device with rectangular cross sections [85, 86], and a glass capillary stenosis [22].

5.2 Methods

5.2.1 *In vitro* model of thrombus formation under high shear

We studied thrombus growth in porcine blood with an *in vitro* flow system described in [109] and Chapter 4. Briefly, whole porcine blood was obtained from a local abattoir (Holifield Farms, Covington, USA). Blood was collected immediately after electrical stunning and lightly anticoagulated with 3.5 USP units/mL of Heparin. A syringe pump (KD Scientific Inc., USA) perfused whole blood through the test section at constant flow rate. The test sections were glass capillaries with hour-glass shaped regions fabricated by a professional glass blower. The degree of diameter stenosis (hereafter stenosis) ranged from 69-72%. The maximum inner diameter of the glass capillaries was 1.5 mm. Prior to the experiments, the surface of the stenotic region was coated with fibrillar collagen type I (Chronolog Corporation, Havertown, PA). WB flowed at constant rates which yielded initial wall shear rates of $\dot{\gamma}_w = 2000 - 6000\ \mathrm{s}^{-1}$ at the apex of the stenoses.

Thrombus formation was monitored using a stereo microscope (Stemi 2000-C, Carl Zeiss Microscopy LLC, Thornwood, NY, USA). Glass capillaries were embedded in glycerol to reduce optical distortion due to the round shape of the glass capillaries. Images were captured at a rate of 10 frames per second. Images and pressure data were recorded using LabVIEW (National Instruments Corporation, Austin, TX, USA).

5.2.2 Image processing

To analyze thrombus growth, we developed an image processing program in Matlab$^{\circledR}$ (Mathworks Inc., Natick, MA, USA) to detect the edges of the thrombi in the captured

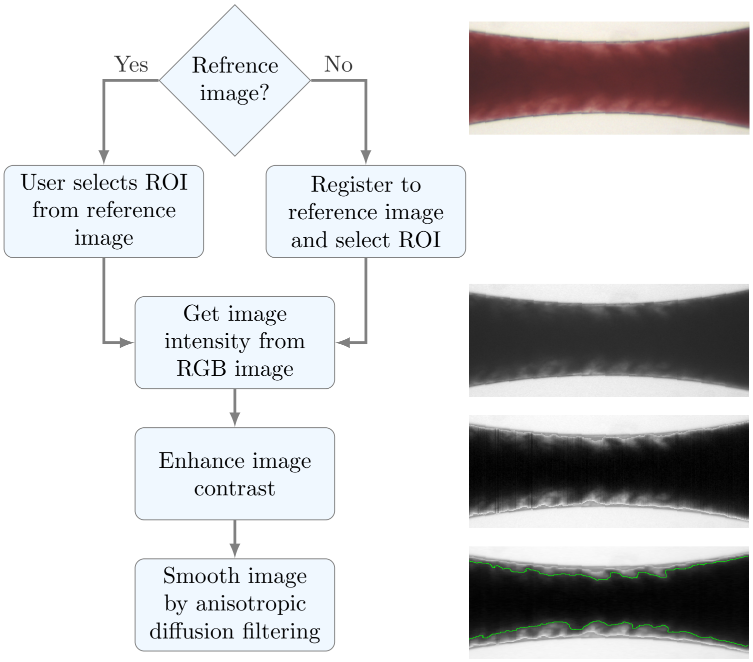

Figure 23: Image processing algorithm

images. The algorithm of the image processing program is outlined in Figure 23. The green channel of the images captured from WB experiments provided the greatest contrast and was used for calculating image intensities. To reduce noise from the variations in light intensity, image processing was performed on averaged images in sets of 5. To find the thrombus edges, a rectangular region of interest (ROI) centered around the apex of the stenosis was selected from the reference image at time $t = 0$. To correct for the small relative motion of the glass capillaries during the experiment, the ROI of an image at $t > 0$ was selected using the location of the maximum of the normalized cross-correlation matrix between the image at t and the reference image at time $t = 0$.

Finding the thrombus edge required contrast enhancement of the images by adjusting image intensities. For more effective contrast enhancement, the area for intensity adjustment was limited to the region inside the glass capillaries. To find this region, the location of the inner edges of the glass capillary was found by converting the intensity image to a binary image and applying a modified Moore-Neighbor tracing algorithm implemented in the Matlab® Image Processing Toolbox. With the approximated locations of the inner edges of the glass capillaries, the region for intensity adjustment was set to the area inside the glass capillaries. The intensity adjustment was then performed by dividing this region into one-pixel wide bands normal to the flow direction. This method resulted in enhanced contrast compared to a global intensity adjustment method, since the minimum and maximum values for mapping the intensity were found along each band inside the blood filled region. The enhanced images were smoothed by anisotropic diffusion filtering. This filtering method reduces noise in an image while preserving the edges. We used the Image Edge Enhancing Coherence Filter Toolbox provided by [69, 70] on the Matlab® File Exchange website Finally, the edges of the thrombus in the enhanced image were detected with the same method described above for detecting the edges of the glass capillaries from the intensity values of the raw images. At each time, t, the inner diameter of the thrombus $D_T(z,t)$, is set to the distance between the detected thrombus edges at the axial location z.

5.2.3 Calculation of local thrombus growth rate and lag time

From the image analysis, we obtained the thrombus edge diameter $D_T(z,t)$ as a function of time, t, along the axial direction, z. Local thrombus growth was obtained by partitioning the thrombus edge by points $z_0 < z_1 < z_2 < \cdots < z_n$, where $\Delta z_i = z_{i+1} - z_i = 100\ \mu\text{m}$ for each partition i, $i \in 1, \ldots, n$. At each time point, the volume of the blood-filled region in partition i, $V_{B,i}(t)$, is given by

$$V_{B,i}(t) = \int_{z=z_i}^{z=z_{i+1}} \frac{\pi}{4} D_T(z,t)^2 \mathrm{d}z. \tag{24}$$

The volume of the thrombus in partition i at time t, $V_{T,i}(t)$, can be estimated as $V_{T,i}(t) = V_{B,i}(0) - V_{B,i}(t)$. The rate of growth, $\dot{R}$, can be estimated as

$$\dot{R} = \frac{\partial R_i(t)}{\partial t} = \frac{1}{A_i(t)} \frac{\partial V_{T,i}(t)}{\partial t} \tag{25}$$

where $A_i(t) = \pi D_T(z_{i+1/2}, t)\Delta z_i$ is the surface area of the thrombus in partition i at time t. We defined lag time $t_{\mathrm{Lag},i}$ as the time when the rate of thrombus growth rate increased to 20% of its value at the final minute of the experiment in each section i.

5.2.4 Calculation of local wall shear rate

To find the local values of wall shear rate at each time point during the experiment, $\dot{\gamma}_w(z, t)$, we solved for the flow field in the region bounded by the thrombus surface at each time point. We assumed that the thrombus forms a rigid non-porous boundary. We assumed that the flow field is quasi-steady and solved the steady incompressible Navier-Stokes equations at each time point. Assuming two-dimensional axisymmetric geometry, the radius of the lumen boundary was set to the distance between the detected thrombus edges. We solved for the flow field computationally using Comsol 4.4 (COMSOL Inc, MA, USA). We used structured quadrilateral elements for meshing the domain. The simulation process was automated in Matlab® environment by employing Comsol LiveLink for Matlab®.

5.2.5 Model for predicting thrombus formation rate

The model we used for predicting thrombus formation is based on the model of Bark [9]. Given thrombus growth as a function of time and wall shear rate, $\dot{R}(t, \dot{\gamma}_w)$, the lumen radius at time t is given by

$$R(t) = \int_0^t \dot{R}(t, \dot{\gamma}_w)\mathrm{d}t + R(t = 0) \tag{26}$$

Solving (26) requires the value of $\dot{\gamma}_w$. The value of $\dot{\gamma}_w$ depends on geometric and flow conditions, and it may vary as thrombus grows. We can approximate $\dot{\gamma}_w$ using the analytical solutions for the fully-developed flow in a channel of constant cross-section, i.e., Poiseuille flow. For Poiseuille flow, in a channel with hydraulic radius of R, we have

$$\dot{\gamma}_w = \frac{4Q}{\pi R^3}, \tag{27}$$

where Q denotes flow rate. In a system maintained at a constant flow rate, we can use (27) to estimate $\dot{\gamma}_w$ required for solving (26).

In a flow system maintained at a constant pressure drop Δp, flow rate may be estimated as $Q = \Delta p/\mathcal{R}$, where $\mathcal{R}$ is the resistance of the flow system. The resistance of the flow system may also vary as thrombus grows. For example, if the components of the flow system are connected in series,

$$\mathcal{R} = \mathcal{R}_t + \mathcal{R}_c \tag{28}$$

where $\mathcal{R}_t$ denotes thrombus resistance, and $\mathcal{R}_c$ denotes the resistance of the remaining components of the flow system. The resistance of thrombus varies as it grows and can be approximated with Poiseuille flow assumption, i.e., $\mathcal{R}_t = \mathcal{R}_t(R) = 8\mu L/(\pi R^4)$, where μ is blood viscosity, and L is the length of the thrombus. So, for a flow system maintained at a constant pressure drop Δp, we can estimate $\dot{\gamma}_w$ required for solving (26) by

$$\dot{\gamma}_w = \frac{4}{\pi R^3}\frac{\Delta p}{\mathcal{R}_t(R) + \mathcal{R}_c}. \tag{29}$$

We solved (26) numerically using a first-order accurate forward Euler scheme:

$$R(t^{i+1}) = \dot{R}(t^i, \dot{\gamma}_w)\Delta t + R(t^i). \tag{30}$$

At each time step, $\dot{\gamma}_w$ was calculated from (27) or (29), and $\dot{R}(t^i, \dot{\gamma}_w)$ was approximated using empirical correlations for $\dot{R}(t, \dot{\gamma}_w)$ obtained in this study and by Bark et al. [12].

5.2.6 Statistical analysis

Nonlinear regression analysis was performed using an iterative nonlinear least squares method implemented in Curve Fitting Toolbox™ of Matlab®. To minimize the effect of outliers, a robust regression method (bisquare weights fitting algorithm) was used. To investigate the correlation of thrombus growth rate, $\dot{R}$, to wall shear rate data from multiple experimental cases, we performed analysis of covariance (ANOCOVA)

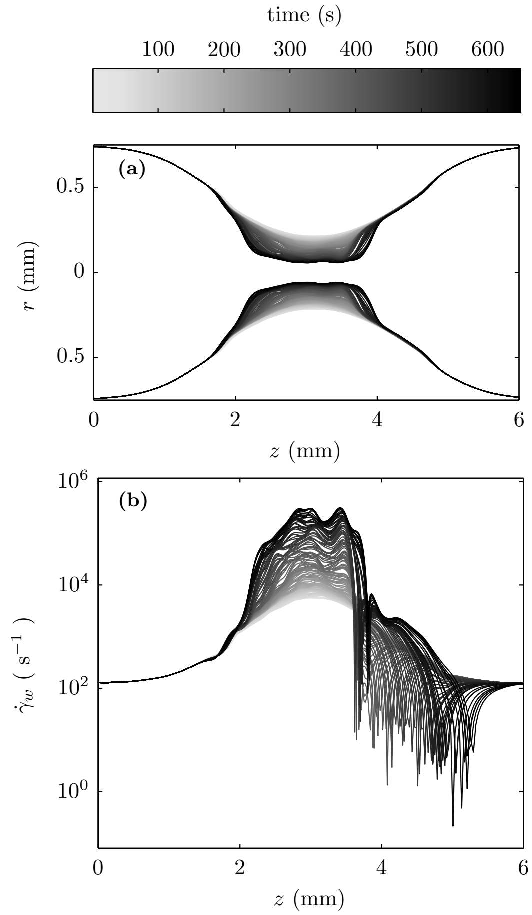

Figure 24: Calculation of local wall shear rate during the thrombus formation. (a) Detected thrombus edges from experimental images show thrombus formation in time. Computed wall shear rate at the edges of the thrombus during the growth time is shown (b).

and fitted parallel lines to the data from each experimental case. The correlation of the local $\dot{R}$, the outcome variable, to the logarithm of local wall shear rate, the predictor variable, was investigated by treating the experimental case as a categorical factor using a dummy variable [12, 17]. A p value of less than 0.05 was considered to indicate statistical significance. Statistical analysis was performed using the Statistics Toolbox$^{\text{TM}}$ of Matlab$^{\circledR}$ software.

5.3 Results

5.3.1 Local wall shear rate during thrombus growth

Representative detected edges of the thrombus in glass capillaries perfused with WB are shown in Figure 24(a). Computed wall shear rates at the edges of the thrombus during the growth time is shown 24(b). Thrombus formation was slow at the beginning, but entered a rapid formation phase after a short lag time. Thrombus growth at the apex of the stenosis narrowed the lumen. At constant flow rate, this narrowing lumen leads to a considerable increase of wall shear rates at the stenosis apex (e.g., from $\dot{\gamma}_w \approx 6 \times 10^3$ to 2.8×10^5 s^{-1} in the case shown in Figure 24). The narrowing of the lumen also leads to flow separation downstream of the apex and the drop of the local wall shear rate in this region.

5.3.2 Thrombus growth as a function of shear rate

Figure 24 suggests a correlation between local growth rate, $\dot{R}$, and local wall shear rate. Following a short lag time, thrombus grew most rapidly at the apex of the stenosis where the maximum wall shear rate occurred Figure 24(b). The fast growth at the apex eventually decelerated as the wall shear rates at the stenosis apex increased by orders of magnitude. At regions further away from the apex, where wall shear rates were lower than those of the apex, thrombus initially grew slowly but accelerated with the increase of the local wall shear rate. This growth pattern results in a relatively uniform thrombus edge towards the end of the experiment, despite the initial focal growth around the apex. The growth pattern observed in Figure 24 suggests that high $\dot{R}$ occurs above a threshold of $\dot{\gamma}_w \approx 1000$ s^{-1}. The observed growth pattern also suggests that $\dot{R}$ is a non-monotonic function of wall shear rate.

The non-monotonic relation between thrombus growth rate and wall shear rate is more evident from the scatter plot of local thrombus growth *vs* local shear rate (Figure 5.3.2). Thrombus growth increases with increasing shear rate up to a shear

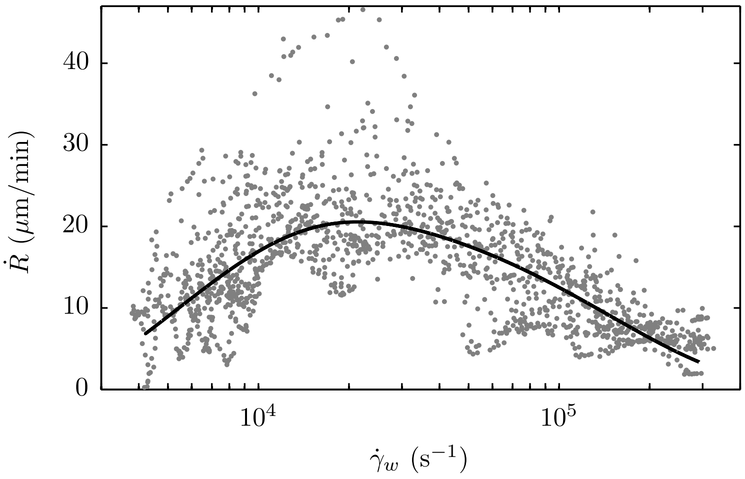

Figure 25: Thrombus growth rate as a function of local shear rate. The scatter data are from analysis of a single experiment after a lag period (shown in Figure 24). The solid line represents a two-term exponential regression curve $\dot{R}(\dot{\gamma}_w) = -36.2 \exp[-1.77 \times 10^{-4}\dot{\gamma}_w] + 24.7 \exp[-6.81 \times 10^{-6}\dot{\gamma}_w]$ (μm/min), $r^2 = 0.60$).

rate of $\dot{\gamma}_w \approx 2 \times 10^4$, and decreases beyond this value. A nonlinear function was fitted to the data using a nonlinear least squares formulation implemented in Curve Fitting Toolbox$^{\text{TM}}$ of Matlab$^{\text{®}}$. Nonlinear regression curves fitted to separate experimental cases ($n = 13$) follow the same trend (Figure 26).

For experimental case i, $\dot{\gamma}^i_{\dot{R}_{\max}}$ denotes the shear rate at which maximum growth rate occurs. The value of $\dot{\gamma}^i_{\dot{R}_{\max}}$ is estimated using the nonlinear regression curve fitted to the data (i.e., by finding the shear rate at which the derivative of the regression curve vanishes). For multiple experiments, $\dot{\gamma}_{\dot{R}_{\max}}$ is the mean of $\dot{\gamma}^i_{\dot{R}_{\max}}$. Similarly, $\dot{R}_{\max}$ is the mean of $\dot{R}^i_{\max}$. In cases that thrombi embolized at shear rates below $\approx 3 \times 10^4$ s^{-1} ($n = 2$), growth rate increases monotonically with shear rate. We excluded these cases for estimating $\dot{\gamma}_{\dot{R}_{\max}}$. As shown in Figure 26, we found the maximum growth rate of $\dot{R}_{\max} \pm \sigma(\dot{R}_{\max}) = 26.8 \pm 5.8$ μm/min at shear rate of $\dot{\gamma}_{\dot{R}_{\max}} \pm \sigma(\dot{\gamma}_{\dot{R}_{\max}}) = 2.5 \times 10^4 \pm 8.4$ s^{-1} ($n = 11$).

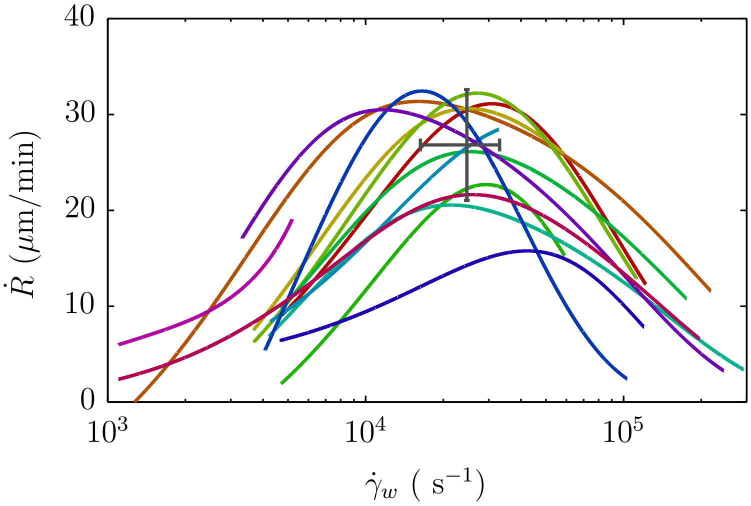

Figure 26: Plot of the nonlinear regression curves fitted to data from separate experiments. Horizontal and vertical error bars show 95% confidence intervals of maximum growth rate $\dot{R}_{\max}$ and the shear rate at which maximum growth rate occurs $\dot{\gamma}_{\dot{R}_{\max}}$.

5.3.3 Lag time correlation with shear rate

Thrombus growth often starts slow and then accelerates to a maximal value in a certain period of time, resulting in a lag time t_{Lag}. The scatter plot of lag time *vs* local shear rate is shown in Figure 27. Lag time is large at low shear rates ($\dot{\gamma}_w < 10^3\ \text{s}^{-1}$) and drops with increasing shear rate. We performed ANOCOVA to investigate the correlation of lag time, t_{Lag}, to wall shear rate. The correlation analysis was performed on logarithm transformed data. The correlation of $\log t_{\text{Lag}}$, the outcome variable, to the logarithm of local wall shear rate, the predictor variable, was investigated by treating the experimental case as a categorical factor using a dummy variable [12, 17]. We found that $\log t_{\text{Lag}}$ correlates negatively with $\log \dot{\gamma}_w$ ($n = 12$, $r = -0.79$, $p < 0.0001$). Using Curve Fitting Toolbox™ of Matlab®, a power-law function was fitted to the data from multiple experiments:

$$t_{\text{Lag}}(\dot{\gamma}_w) = 1.69 \times 10^6 \dot{\gamma}_w^{-1.2} \quad (\text{s}) \tag{31}$$

In comparison to the power-law function found by Bark et al. [12], the lag time function found in this study predicts longer lag at lower shear rates and shorter lag

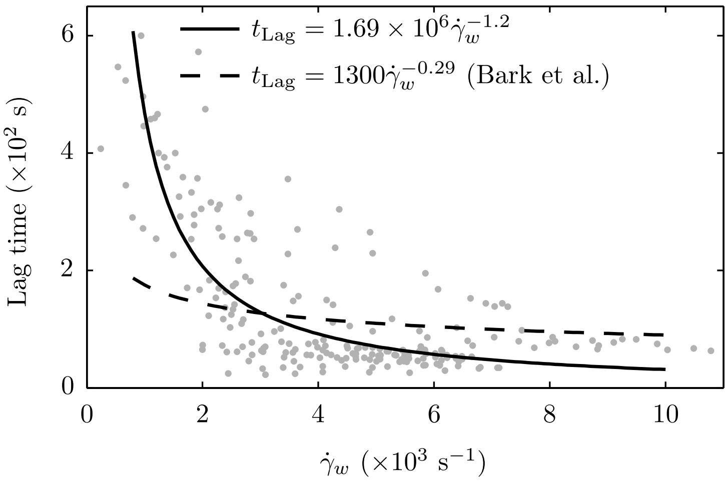

Figure 27: Scatter plot of lag time as a function of local shear rate. The dashed line represents the power-law function fitted to the data. The dark solid line shows the correlation found by Bark et al. [12].

at higher shear rates (Figure 27).

5.3.4 Growth rate correlation with shear rate

We performed ANOCOVA to investigate the correlation of thrombus growth rate after the lag phase, $\dot{R}(t > t_{\text{Lag}})$, to wall shear rate data from multiple experimental cases. At shear rates below $\dot{\gamma}_{\dot{R}_{\max}} + \sigma\left(\dot{\gamma}_{\dot{R}_{\max}}\right)$, thrombus growth correlates positively with $\dot{\gamma}_w$ ($n = 13$, $r = 0.59$, $p < 0.0001$) and at shear rates above $\dot{\gamma}_{\dot{R}_{\max}} - \sigma\left(\dot{\gamma}_{\dot{R}_{\max}}\right)$, thrombus growth correlates negatively with $\dot{\gamma}_w$ ($n = 11$, $r = -0.48$, $p < 0.0001$).

To obtain a functional relationship between $\dot{R}(t > t_{\text{Lag}})$ and $\dot{\gamma}_w$ from data of multiple experiments, an exponential function was fitted to the data. Nonuniform distribution of data of single experimental cases may incorrectly bias the results of analysis of multiple cases if all data were combined and analyzed as if they were from a single experimental case. To avoid this bias, the data were divided into bins based on shear rate (i.e., $\dot{\gamma}_1 = 10^3 < \dot{\gamma}_2 < \cdots < \dot{\gamma}_n = 2 \times 10^5$). Within each bin, the averaged value of data from an experimental case was considered as a single data point for calculating the mean and standard deviation values for multiple cases (Figure 28). Using Curve Fitting Toolbox™ of Matlab®, a two-term exponential function was

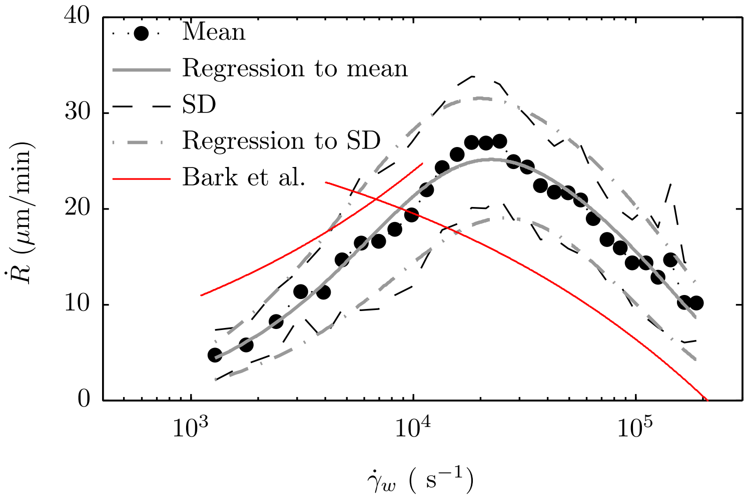

Figure 28: Thrombus radial growth rate $\dot{R}$ plotted as a function of local wall shear rate $\dot{\gamma}_w$. The data were divided into bins based on shear rate, and the averaged value of data from each experimental case was considered as a single data point for calculating the mean and standard deviation (SD) for multiple cases. Exponential functions were fitted to the mean and standard deviation curves. The dark solid lines (red online) show the correlation found by Bark et al. [12].

Table 5: Correlations for thrombus growth rate were found in the form of $\dot{R}\,(t > t_{\mathrm{Lag}}, \dot{\gamma}_w) = ae^{b\dot{\gamma}_w} + ce^{d\dot{\gamma}_w}$. Correlation relations for the mean and the lower and upper confidence limits are denoted by $\dot{R}_M$, $\dot{R}_L$ and $\dot{R}_U$, respectively.

	a (μm/min)	b ($\times 10^{-4}$ s)	c (μm/min)	d ($\times 10^{-6}$ s)
$\dot{R}_M$	-31.3	-1.45	30.7	-6.81
$\dot{R}_L$	-28.3	-1.00	27.4	-10.0
$\dot{R}_U$	-38.2	-1.81	36.6	-5.92

fitted to the mean of growth rate $\dot{R}_M$. The correlations for the confidence limits of growth rate were found by fitting two-term exponential functions to the standard deviation curves. The lower and upper confidence limits of thrombus growth are denoted by $\dot{R}_L$ and $\dot{R}_U$, respectively. The exponential functions are in the form of

$$\dot{R}\,(t > t_{\mathrm{Lag}}, \dot{\gamma}_w) = ae^{b\dot{\gamma}_w} + ce^{d\dot{\gamma}_w}, \tag{32}$$

and the coefficients a, b, c and d for the functions $\dot{R}_M$, $\dot{R}_L$ and $\dot{R}_U$ are listed in Table 5. The correlations are plotted in Figure 28.

With the correlations for growth rate following lag time $\dot{R}(t > t_{\mathrm{Lag}}, \dot{\gamma}_w)$, we can write thrombus growth rate as a function of time and wall shear rate:

$$\dot{R}(t, \dot{\gamma}_w) = \begin{cases} 0 & \text{if } t < t_{\text{Lag}}(\dot{\gamma}_w), \\ ae^{b\dot{\gamma}_w} + ce^{d\dot{\gamma}_w} & \text{if } t > t_{\text{Lag}}(\dot{\gamma}_w), \end{cases} \tag{33}$$

where the constants a, b, c and d are given in Table 5 and $t_{\text{Lag}}(\dot{\gamma}_w)$ is given by (31).

5.3.5 A predictive model for thrombus formation

We can use the correlations we found for growth rate to estimate thrombus formation rate based on geometry and flow conditions in a given system [9]. We used the empirical correlation (33), to solve a simple model (§5.2.5) for predicting thrombus growth. We will used this model for predicting occlusion times in a platelet function analyzer (PFA-100$^{\text{TM}}$), a microfluidic device with rectangular cross sections [85, 86], and a glass capillary stenosis [22].

5.3.5.1 Closure time in PFA-100$^{\text{TM}}$

We used the model described in §5.2.5, to predict thrombus formation in a platelet function analyzer, PFA-100. In this instrument, blood is perfused at constant pressure through a capillary with diameter $D = 200$ μm into a membrane pore with $D = 150$ μm. The membrane is also coated with collagen type I. In addition membranes are coated with platelet antagonists epinephrine bitartrate (Epi) or adenosine 5'-diphosphate (ADP). A constant pressure of 40 kPa, results in the initial wall shear rate of 5000-6000 s^{-1} at the membrane pore. This high shear rate results in thrombus formation and eventually leads to the occlusion of the membrane pore. The time from the start of blood perfusion until the occlusion of the membrane is called closure time (CT).

To model thrombus formation in the PFA-100$^{\text{TM}}$ instrument, we assumed a length of 1 inches for the 200 μm capillary, a membrane thickness of 150 μm, and blood viscosity of $\mu = 3.5$ mPa. With these assumption, we obtained initial wall shear rate

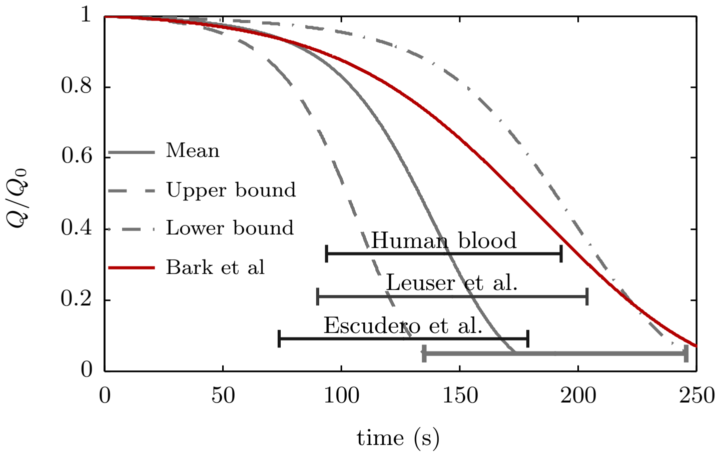

Figure 29: Predicted flow rates and closure times (CTs) for the PFA-100$^{\mathrm{TM}}$ system. In the model, CT was defined as the time when flow rate Q drops to 5% of the flow rate at the beginning of the test Q_0. The predicted range of CT from the model is compared to the experimental ranges of CT for membranes coated by Epi/Collagen obtained with porcine blood (Leuser et al. [82] and Escudero et al. [43]) and human blood [130].

of $\dot{\gamma}_w = 5200$ s^{-1} at the membrane pore. In the model, CT was defined as the time when flow rate Q drops to 5% of the flow rate at the beginning of the test Q_0. We assumed that thrombus forms uniformly at walls of the membrane pore and estimated thrombus growth using (29) and (30). Due to presence of antagonists added to the membrane coating, and the flow through a sudden contraction at the inlet of the pore, we set $t_{\mathrm{Lag}} = 0$ when using (33) for obtaining $\dot{R}(t, \dot{\gamma}_w)$.

Using the empirical correlations in this study we obtained a range of 135-246 s. This range is in agreement with the experimental values of CT for porcine blood on membranes coated by Epi/Collagen (Leuser et al. [82] reported a range of 90-204 s, and Escudero et al. [43] reported a range of 74-179 s). Using the empirical correlation obtained by Bark et al. [12], CT was estimated as 257 s. The predicted CTs are also in agreement with the range of CT for human blood 94-193 s on membranes coated by Epi/Collagen [130] (Figure 29).

5.3.5.2 Occlusion time in microfluidic device of Li et al.

Li et al. designed and fabricated a microfluidic system for simultaneous measurement of thrombus formation in stenotic channels at multiple initial wall shear rates [85, 84, 86]. The flow was driven by a constant pressure difference of 1.4 kPa across all microchannels. Multiple shear rates in identical microchannels were obtained by changing flow resistance downstream of each stenotic channel. The microchannels fabricated in poly-dimethylsiloxane (PDMS) were bonded to microscope glass coverslips via plasma bonding. Prior to the experiments, the channels were coated with collagen.

To model thrombus formation in this microfluidic system, we assumed that thrombus forms in the section of the stenosis with the lowest height. This section has a rectangular cross-section with depth of 300 μm, width of 750 μm and length of 300 μm in the flow direction. Li [84] found that PDMS surfaces absorbed much less collagen than glass surfaces. Therefore, we assumed that thrombus grows only on the glass surface. We estimated thrombus growth using (29) and (30). In (29), $\mathcal{R}_c$ values were set by matching the initial wall shear rate at the stenosis with those of the experiment. We defined occlusion time as the time when Q drops to 5% of Q_0 in each channel.

Li et al. measured the occlusion time in whole porcine blood [85], and in whole human blood [86]. Predicted occlusion times at initial wall shear rates over a range of 1500-13000 s^{-1} are in agreement with the experimental results of [85] and [86] (Figure 30). In comparison to the correlation of Bark et al. [12], the correlations obtained in this study yield a larger variation in occlusion time with initial wall shear rate.

5.3.5.3 Lag time and occlusion in glass capillaries

Casa and Ku [22] studied thrombus formation in stenosed glass capillaries under steady and pulsatile flow conditions. The flow system under steady flow conditions

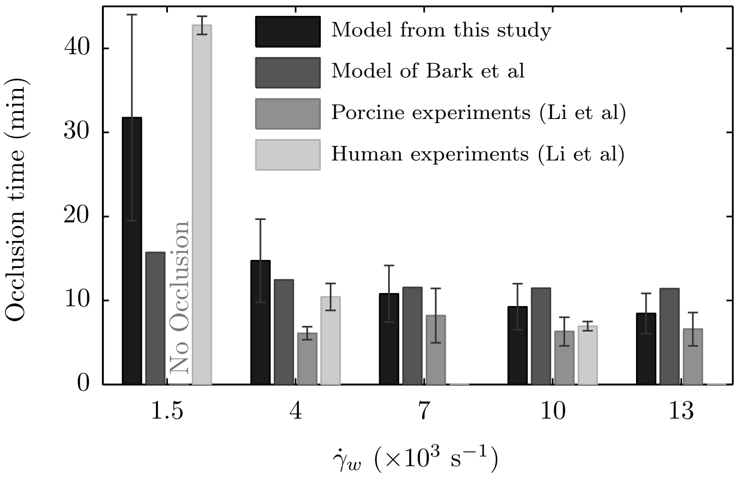

Figure 30: Predicted occlusion times for microfluidic system of Li et al. [85, 84, 86]. The predicted range of occlusion from the model is compared to the experimental ranges of occlusion time in whole porcine blood [85] and in whole human blood [86].

was similar to the one used in this study. Whole porcine blood was perfused in stenosed glass capillaries with stenosis degree of $s = 77$-79% and maximum diameter of $D = 1.5$ mm. Prior to the experiments, the glass capillaries were coated with fibrillar collagen. Flow was driven under constant pressure difference to obtain initial wall shear rates of 3800, 6500 and 16000 s^{-1} at the apex of the stenosed glass capillaries.

To model thrombus formation in glass capillaries, we approximated the initial radius of the glass capillary using a function introduced by Bark and Ku [10]

$$R(z, t = 0) = \frac{D}{2} - \frac{Ds}{800}\left(1 - \cos\left[\pi\left(1 + \frac{2z}{L_s}\right)\right]\right)^2, \tag{34}$$

where L_s denotes the length of the stenosis. In the model, we set $L_s = 4D$, and $s = 78\%$.

We approximated the capillary geometry as a set of thin cylinders connected in series. The stenosis length was partitioned by points $z_0 < z_1 < z_2 < \cdots < z_n$, where $z_0 = 0$, $z_n = L_s$ and $n = 100$. In partition j, the capillary wall was approximated as a cylinder with the length of $\Delta z = z_{j+1} - z_j$, and initial radius of $R_j(t^0) = R(z_j, t = 0)$ calculated from (34). We updated the lumen radius at each time step, using the vectorized form of (30), i.e.,

$$R_j(t^{i+1}) = \dot{R}(t^i, \dot{\gamma}_{w,j})\Delta t + R_j(t^i), \quad j \in 1 \ldots n, \tag{35}$$

where $\dot{\gamma}_{w,j}$ denotes wall shear rate in partition j. The value of $\dot{\gamma}_{w,j}$ was calculated by (29), where the resistance of the stenosis was calculated by summing the resistance of all the cylinders, i.e., $\mathcal{R}_t = \sum_{j=1}^{n} \mathcal{R}_j = (8\mu\Delta z/\pi) \sum_{j=1}^{n} 1/R_j^4$. The values of $\mathcal{R}_c$ and Δp were set by matching the initial wall shear rate at the apex of the stenosis with those of the experiment.

Casa and Ku [22] defined occlusion time as the time when the discharged mass remained constant for at least 2 min. Accordingly, we defined occlusion time as the time when Q drops to below 0.05 mL/min by assuming a measurement precision of 0.1 g. Similarly, we used the same criterion for determining lag time set by Casa and Ku [22], i.e., the time for thrombus volume to reach to 10^6 μm^3.

Figure 31, shows thrombus formation predicted using the correlations from this study (i.e., correlation for $\dot{R}_M$ from Table 5, and (31) for lag time) at shear rate of 16000 s^{-1}. Microscopic images of thrombus formation obtained by Casa and Ku [22] are also shown for comparison. The predicted pattern of thrombus formation is in qualitative agreement with those of the experiments. The thrombus grows focally at the apex of the stenosed glass capillary.

Predicted lag times and occlusion times at initial wall shear rates over a range of 3800-16000 s^{-1} are compared to the experimental results of Casa and Ku [22] (Figure 32). The lag times predicted with the correlations from this study are closer to experimental lag times than those predicted with the correlation of Bark et al. [12]. The occlusion times predicted by the correlations obtained in this study are in better agreement to experimental occlusion times at the higher shear rate of 16000 s^{-1}. The occlusion times predicted by the correlation of [12] are in better agreement to experimental occlusion times at the lower shear rate of 3800 s^{-1}.

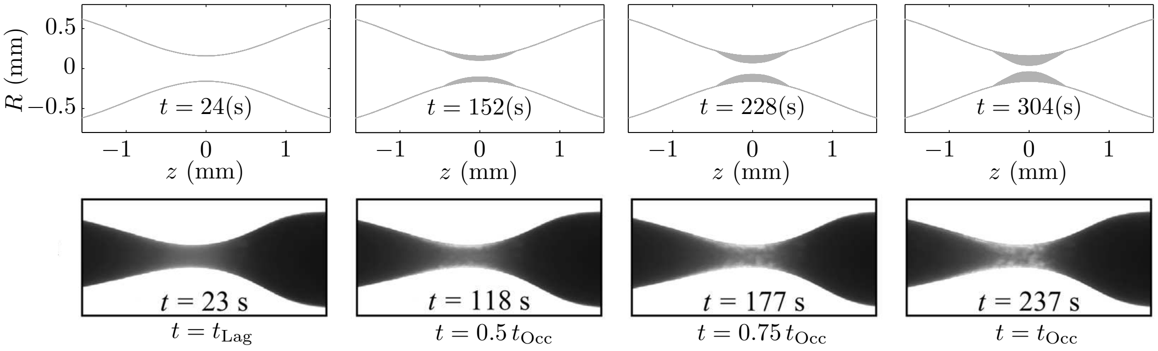

Figure 31: Thrombus formation in glass capillaries at initial wall shear rate of 16000 s^{-1}. Images are obtained at lag time, 50time. Thrombus formation predicted using the correlations obtained in this study are shown on top. Microscopic images of thrombus formation obtained by Casa and Ku [22] are also shown for comparison.

5.4 Discussion and Conclusion

In this work, we extended the study by Bark et al. [12] who obtained empirical correlations for lag time and thrombus growth rate as a function of local shear rate using an *in vitro* thrombus model. We extended the correlations obtained by [12] by analyzing more experimental cases ($n = 11 - 13$), specifically at shear rates above 2×10^4 s^{-1}. We also determined correlations for lower and upper confidence limits for thrombus growth rate. The relationships found here are in qualitative agreement with those found by [12].

In agreement with the results of [12], we found that lag time decreases monotonically with increasing shear rate over a range of 1000-10000 s^{-1}. In comparison to the correlation found by [12], the extended correlation predicts longer lags at lower shear rates and shorter lags at higher shear rates. The shorter lag times at higher shear rates found here, may be due to the difference in the collagen preparations used for coating the surface of the glass capillaries. Fibrillar collagen, used in this study, is more effective than acid-soluble collagen, used by Bark et al. [12], for supporting adhesion of platelets under flow [15, 84].

We found a non-monotonic relation between thrombus growth rate and wall shear rate. This functional relationship is in agreement with the results of [12]. Thrombus

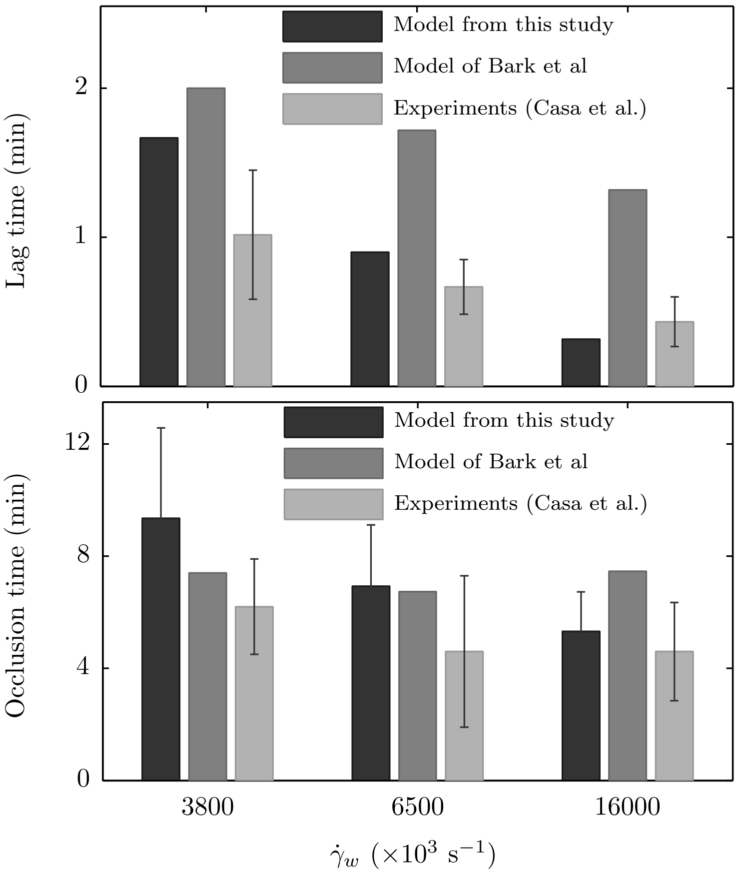

Figure 32: Predicted lag times and occlusion times in stenosed glass capillaries are compared to the experimental ranges of lag time and occlusion time in whole porcine blood [22]

growth increases with increasing shear rate up to a shear rate of $\dot{\gamma}_{\dot{R}_{\max}} = 2.5\times10^4 \pm 8.4$ s^{-1} ($n = 11$), and decreases beyond this value. Bark et al. [12] estimated $\dot{\gamma}_{\dot{R}_{\max}} \approx 6\times10^3$ s^{-1} ($n = 3-4$). In comparison to the correlations found by Bark et al. [12], we found slower growth rates at $\dot{\gamma}_w \lesssim 10^4$ s^{-1} and faster growth rates beyond 10^4 s^{-1}. Our results are in better agreement with results of Ku and Flannery [71] who found that thrombus growth increases with shear rate over a range of $10^4 - 4.2\times10^4$ s^{-1} in porcine blood. Experimental results of Casa and Ku [22] suggests weak (not statistically significant) negative correlation between thrombus growth rate and shear rate over a range of $3.8\times10^3 - 1.6\times10^4$ s^{-1} in porcine blood. The value of $\dot{\gamma}_{\dot{R}_{\max}}$ in human blood may be lower than that of porcine blood. In human blood, occlusion occurs significantly faster at $\dot{\gamma}_w = 10^4\ \mathrm{s}^{-1}$ than at $\dot{\gamma}_w = 4 \times 10^3\ \mathrm{s}^{-1}$ [86]. Barstad et al. [13] found lower thrombus growth rate at $3.2 \times 10^4\ \mathrm{s}^{-1}$ vs $10^4\ \mathrm{s}^{-1}$. These results suggests that $\dot{\gamma}_{\dot{R}_{\max}}$ in human blood may be larger than $10^4\ \mathrm{s}^{-1}$ but lower than that of porcine blood.

We extended the model developed by Bark [9] to utilize thrombus growth correlations for predicting thrombus formation rate based on geometry and flow conditions in a given system. We used the empirical correlations obtained here and by Bark et al. [12] to solve a simple model for predicting thrombus growth. We used the model to predict occlusion times in a platelet function analyzer (PFA-100$^{\mathrm{TM}}$), a microfluidic device with rectangular cross sections [85, 86], and a glass capillary stenosis [22]. Overall, the model results using the correlations developed in this study were in better agreement with the experimental results in comparison to the correlation found by Bark et al. [12]. The better agreement may be due to the larger number of cases considered here.

Comparison of occlusion times obtained for human and porcine blood in the microfluidic device of Li et al. (Figure 30) and those of PFA-100$^{\mathrm{TM}}$ (Figure 29) suggests that the timescale of thrombosis formation in porcine blood resembles that of human blood. Nevertheless, obtaining correlations for lag time and thrombus growth rate in human blood may help in more accurate predictions of thrombus formation for human blood.

The surface coating may significantly affect thrombus lag time and subsequently the rate of thrombus formation. Both Bark et al. and we used collagen for coating the test sections in the experiments for characterizing thrombus lag time and growth. Yet, the difference in the collagen preparation methods for coating the surface of the test sections led to noticeable differences between the correlations found in the two studies. Thrombus lag time on other materials may be significantly different from those on collagen coated surfaces. Further studies are required to to obtain correlations for lag time on other materials. In addition, our correlation for lag time was obtained at initial wall shear rates of $10^3 - 10^4$ s^{-1}. Within this range, we found that lag time monotonically decreases with $\dot{\gamma}_w$. This trend may not extend to much higher shear rates. Further studies are required to extend the correlations for lag time to shear rates beyond 10^4 s^{-1}.

In conclusion, we extended the study of Bark et al. [12] by obtaining correlations for thrombus growth and lag time based on flow parameters by using an *in vitro* model of thrombosis. We then extended a model introduced by Bark [9] to develop a simple model for predicting thrombus formation using the obtained empirical correlations. We used the model for thrombus formation in a platelet function analyzer (PFA-100$^{\mathrm{TM}}$), a microfluidic device with rectangular cross sections [85, 86], and a glass capillary stenosis [22]. We demonstrated the capability of the model in predicting thrombus formation over a wide range of experimental geometries. The agreement between the model results and experimental results demonstrates the applicability of this model for estimating the likelihood of occlusive thrombus formation in patients due to plaque erosion or plaque rupture. In addition, this model may be useful for designing blood-contacting devices to avoid unwanted thrombosis.

CHAPTER VI

CONCLUSION

In this thesis, we studied the effects of hemodynamics on thrombus growth and discovered these findings as follows:

- Using DNS of cellular blood flow, we investigated the effects of important flow and particle properties on margination of particles in RBC suspensions. We derived a scaling law for margination length in blood flow. Based on this scaling law, margination length increases cubically with channel height and is independent of shear rate. Using the DNS of the flow of RBC and marginating particles in straight channels we verified the proposed scaling law for margination length. We also showed that rigidity and size both lead to particle margination, with rigidity having a more significant effect compared to size within the range of parameters in this study.

- We developed a simple continuum model for platelet transport based on the hypothesis that the dominant mechanism for platelet margination is the RBC-enhanced shear-induced diffusion (RESID) of platelets with a free-escape boundary at the edge of the cell-laden region. With the diffusion coefficient estimated from DNS model, the continuum model can match the DNS results for platelet margination rate. This continuum model provides a much simpler method for estimating platelet concentration profiles that is significantly faster computationally compared with the DNS of blood flow. Using diffusion coefficients obtained by experiments the proposed continuum model can capture the margination levels observed in experiments. Our proposed model is simpler than previous continuum models proposed for predicting margination and requires fewer inputs. It also improves over previous models since its results are in good agreement with experimental results of margination in the transient regime over a wide range of tube sizes.

- Studying the flow of whole blood and platelet-rich plasma, we found that rapid thrombus growth at high shears does not require the presence of any red blood cells. Thus, the rate-limiting step for thrombus growth at high shears is not platelet transport by RESID or margination, and large changes in transport of platelets is unlikely to affect thrombosis. the presence of RBCs is not necessary for rapid thrombus growth at high shear. The absence of RBCs increases the lag time of rapid thrombus growth. Instead, our results suggest that the availability of vWF-A1 domains may be rate limiting at high shears.

- We extended the study of Bark et al. [12] by obtaining correlations for thrombus growth and lag time based on flow parameters by using an *in vitro* model of thrombosis. We then extended a model introduced by Bark [9] to develop a simple model for predicting thrombus formation using the obtained empirical correlations. We employed the model for thrombus formation in a platelet function analyzer (PFA-100$^{\text{TM}}$), a microfluidic device with rectangular cross sections [85, 86], and a glass capillary stenosis [22]. We demonstrated the capability of the model in predicting thrombus formation over a wide range of experimental geometries.

6.1 Contributions

The main contributions of this work are as follows:

- Using DNS we have studied important parameters affecting platelet transport in blood flow. Identifying parameters affecting margination can help in design and optimization of devices that employ margination for separation of particles and cells from blood, such as Malaria-infected RBCs [58], leukocytes [128], and circulating cancer cells [140]. Furthermore; identifying particle properties that affect margination are important for design of more effective vascular-targeted nano- and micro-carriers [24, 25, 100, 138, 144].

- We proposed that margination of platelets in flowing blood is due to the RBC-enhanced shear induced diffusion of platelets in the RBC-rich region with a free-escape boundary at the edge of the cell-laden region. A continuum (DFEB) model is developed based on this proposed mechanism for margination. The DFEB model provides a much simpler method for estimating platelet concentration profiles that is significantly faster computationally compared with the DNS of blood flow. Using diffusion coefficients obtained by experiments, the DFEB model can capture the margination levels observed in experiments. Our proposed model is simpler than previous continuum models proposed for predicting margination and requires fewer inputs, and yet it improves over previous models since its results are in good agreement with experimental results of margination in the transient regime over a wide range of tube sizes. Thus, our proposed model would be useful in modeling complex processes which involve transport of particles in blood.

- Results of computational models of thrombus formation [11, 79, 162] and *in vitro* experiments of platelet adhesion on subendothelium [1, 2, 147, 150] have led to the general agreement that the presence of RBCs is necessary for rapid thrombus formation at high shear. Our experimental results indicate that upstream platelet margination is unnecessary for rapid growth of occlusive thrombi at high shear rates. Furthermore, we found that RBCs are not needed for rapid thrombus growth thrombus growth rate, while RBCs only reduce the time for rapid thrombus growth onset. Our results suggests that the availability of vWF-A1 domains may limit thrombus growth rate at high shear. Identifying the rate limiting processes in thrombus growth may help in developing methods for preventing occlusive arterial thrombosis.

Previous experimental studies with similar conditions to this study but with short perfusion time, have found a positive correlation between the rate of platelet adhesion on subendothelium and hematocrit [1, 2, 147, 150]. We can find a similar trend in our study, if we compare initial growth rate between WB and PRP. But we found no significant difference between the thrombus growth rate in the rapid growth phase after the initial lag time between WB and PRP. Lag time, t_{lag}, or the total time for occlusion,$t_{\text{occlusion}}$ may be more important for treating a patient for major bleeding, the time for occlusion after the onset of rapid thrombus formation, $t_{\text{occlusion}} - t_{\text{lag}}$, may be more important for treating a patient with cardiovascular disease as it may determine response time after initial warning symptoms. Apart from ischemia, bleeding is the most frequent complication in the management of acute coronary syndrome [55]. Thus, it may be important to distinguish how different processes and mechanisms affect t_{Lag} and $t_{\text{occlusion}} - t_{\text{lag}}$, especially for treating cardiovascular patients.

- Thrombus formation is a complex process that depends on fluid mechanic conditions, blood thrombogenicity, and surface chemical properties. Several studies have attempted to develop models for predicting thrombogenicity and thrombus formation (see [28, 155, 166] for recent reviews). However, because of the complexities involved in the thrombus formation process, current predictive models for thrombus formation still have limited practical applicability [28]. By extending the study of Bark et al. [12], we developed an efficient model for thrombus formation and validated the model with several experiments. The developed model is simple and efficient, yet it is capable of predicting thrombus formation well. We demonstrated the capability of the model in predicting thrombus formation over a wide range of experimental geometries. The agreement between the model results and experimental results demonstrates the applicability of this model for estimating the likelihood of occlusive thrombus formation in patients due to plaque erosion or plaque rupture. In addition, this model may be useful for designing blood-contacting devices to avoid unwanted thrombosis. This model could aid cardiovascular device manufacturers in developing safer devices while reducing product development times and costs.

6.2 Future directions

In Chapter 2, we studied the effect of hemodynamic parameters on platelet margination in straight channels. Experimental studies on the flow of suspensions of rigid spheres in complex geometries have shown that secondary flows may have significant effects in migration of rigid particles [96, 95, 134]. Physiologically relevant geometries are often far from straight channels. DNS studies in more complex geometries such as stenosed tubes is necessary for understanding the effects of secondary flows on platelet margination.

In Chapter 3, we have only validated the proposed continuum model for platelet transport in straight tubes. The validation of the DFEB model in complex geometries requires further investigation through experimental studies of platelet transport in such geometries.

In addition to platelets, vWF plays an important role in thrombus formation at high shear rates [118, 121, 119, 120]. Thrombus formation at high shear rates initiates by absorption and immobilization of vWF to exposed collagen fibrils. Absorption of vWF onto collagen is essential for thrombus formation at high shear, since only bonds between vWF-A1 domains and platelet glycoprotein receptor GPIbα can form fast enough to capture platelets. At $\dot{\gamma} \gtrsim 1000\ \mathrm{s}^{-1}$, platelets cannot directly bind to collagen without vWF [44, 104, 123, 132]. Instead of platelet transport, the availability of vWF-A1 domains may limit thrombus growth rate at high shears.

As we showed in Chapter 4, the enhanced platelet transport in the presence of RBCs is not necessary for rapid thrombus growth at high shear. Instead, our results suggest that the availability of vWF-A1 domains may limit thrombus growth rate at high shear. The availability of vWF-A1 domains depends on the availability and unfolding of vWF. In chapter 3, we hypothesized that platelet margination is due to the irreversible flow of platelets into the RBC-free layer. A similar mechanism may also lead to the margination and increased concentration of large proteins and macromolecules such as vWF at the wall. This hypothesis could be tested via experimental and DNS studies.

Reducing the transport of plasma vWF to the surface of a growing thrombus may not prevent rapid thrombus growth, even if the availability of vWF-A1 domains is rate limiting for thrombus growth at high shear. Our results suggest that the decreased transport of vWF in the absence of RBCs only delays the onset of rapid thrombus growth. After a lag time of few minutes, activated platelets may release vWF and increase the local concentration of vWF by an order of magnitude [158]. In addition to plasma vWF and vWF released from activated platelets, injured endothelial cells can rapidly secrete vWF by releasing their specialized storage granules called Weibel-Palade bodies [37, 102, 157]. Thus, reducing the transport of plasma vWF to the surface of a growing thrombus may only delay the onset of rapid thrombus growth. Instead, rapid thrombus growth may be prevented by increasing the timescale of vWF unfolding. DNS studies could be used to determine the effect of flow parameters such as shear rate and flow field on vWF unfolding timescale. DNS could also be used to evaluate the effectiveness of increasing the unfolding timescale of vWF in preventing thrombosis.

REFERENCES

[1] P. A. M. M. Aarts, P. A. Bolhuis, K. S. Sakariassen, R. M. Heethaar, and J. J. Sixma. Red blood cell size is important for adherence of blood platelets to artery subendothelium. Blood, 62(1):214–7, July 1983.

[2] P. A. M. M. Aarts, P. Steendijk, J. J. Sixma, and R. M. Heethaar. Fluid shear as a possible mechanism for platelet diffusivity in flowing blood. Journal of biomechanics, 19(10):799–805, January 1986.

[3] P. A. M. M. Aarts, S. A. T. van den Broek, G. W. Prins, et al. Blood platelets are concentrated near the wall and red blood cells, in the center in flowing blood. Arteriosclerosis, 8(6):819–824, 1988.

[4] M. Abkarian and A. Viallat. Dynamics of vesicles in a wall-bounded shear flow. Biophysical Journal, 89(2):1055–66, August 2005.

[5] M. Abkarian and A. Viallat. Vesicles and red blood cells in shear flow. Soft Matter, 4(4):653, 2008.

[6] C. K. Aidun and J. R. Clausen. Lattice-boltzmann method for complex flows. Annual Review of Fluid Mechanics, 42(1):439–472, January 2010.

[7] C. K. Aidun, Y. Lu, and E.-J. Ding. Direct analysis of particulate suspensions with inertia using the discrete boltzmann equation. Journal of Fluid Mechanics, 373:287–311, 1998.

[8] J. F. Antaki, M. R. Ricci, J. E. Verkaik, et al. Pediaflow™ maglev ventricular assist device: A prescriptive design approach. Cardiovascular Engineering and Technology, 1(1):104–121, March 2010.

[9] D. L. Bark. The Hemodynamics During Thrombosis and Impact on Thrombus Growth. Phd dissertation, Georgia Institute of Technology, 2010.

[10] D. L. Bark and D. N. Ku. Wall shear over high degree stenoses pertinent to atherothrombosis. Journal of biomechanics, 43(15):2970–7, November 2010.

[11] D. L. Bark and D. N. Ku. Platelet transport rates and binding kinetics at high shear over a thrombus. Biophysical Journal, 105(2):502–11, July 2013.

[12] D. L. Bark, A. N. Para, and D. N. Ku. Correlation of thrombosis growth rate to pathological wall shear rate during platelet accumulation. Biotechnology and bioengineering, 109(10):2642–50, October 2012.

[13] R. M. Barstad, H. E. Roald, Y. Cui, V. T. Turitto, and K. S. Sakariassen. A perfusion chamber developed to investigate thrombus formation and shear profiles in flowing native human blood at the apex of well- defined stenoses. Arteriosclerosis, Thrombosis, and Vascular Biology, 14(12):1984–1991, December 1994.

[14] M. R. Beck and E. C. Eckstein. Preliminary report on platelet concentration in capillary tube flows of whole blood. Biorheology, 17(5-6):455, 1980.

[15] A. Bernardo, A. L. Bergeron, C. W. Sun, et al. Von Willebrand factor present in fibrillar collagen enhances platelet adhesion to collagen and collagen-induced platelet aggregation. Journal of Thrombosis and Haemostasis, 2(4):660–669, April 2004.

[16] P. Bhatnagar, E. Gross, and M. Krook. A model for collision processes in gases. I. Small amplitude processes in charged and neutral one-component systems. Physical Review, 94(3):511–525, May 1954.

[17] J. M. Bland and D. G. Altman. Statistics notes: Calculating correlation coefficients with repeated observations: Part 1—correlation within subjects. BMJ, 310(6977):446, February 1995.

[18] B. Boneu and F. Fernandez. The role of the hematocrit in bleeding. Transfusion Medicine Reviews, 1(3):182–185, December 1987.

[19] C. Bustamante, Z. Bryant, and S. B. Smith. Ten years of tension: single-molecule dna mechanics. Nature, 421(6921):423–427, January 2003.

[20] H. Byun, T. R. Hillman, J. M. Higgins, et al. Optical measurement of biomechanical properties of individual erythrocytes from a sickle cell patient. Acta biomaterialia, 8(11):4130–8, November 2012.

[21] Y. Cadroy and S. R. Hanson. Effects of red blood cell concentration on hemostasis and thrombus formation in a primate model. Blood, 75(11):2185–93, June 1990.

[22] L. D. C. Casa and D. N. Ku. High shear thrombus formation under pulsatile and steady flow. Cardiovascular Engineering and Technology, February 2014.

[23] W. Cha and R. L. Beissinger. Augmented mass transport of macromolecules in sheared suspensions to surfaces b. bovine serum albumin. Journal of Colloid and Interface Science, 178(1):1–9, March 1996.

[24] P. Charoenphol, S. Mocherla, D. Bouis, et al. Targeting therapeutics to the vascular wall in atherosclerosis–carrier size matters. Atherosclerosis, 217(2): 364–70, August 2011.

[25] P. Charoenphol, P. J. Onyskiw, M. Carrasco-Teja, and O. Eniola-Adefeso. Particle-cell dynamics in human blood flow: implications for vascular-targeted drug delivery. Journal of biomechanics, 45(16):2822–8, November 2012.

[26] S. Chen and G. D. Doolen. Lattice boltzmann method for fluid flows. Annual Review of Fluid Mechanics, 30:329–64, March 1998.

[27] P. K. Cheruvu, A. V. Finn, C. Gardner, et al. Frequency and distribution of thin-cap fibroatheroma and ruptured plaques in human coronary arteries: a pathologic study. Journal of the American College of Cardiology, 50(10):940–9, September 2007.

[28] S. Cito, M. D. Mazzeo, and L. Badimon. A review of macroscopic thrombus modeling methods. Thrombosis research, 131(2):116–24, February 2013.

[29] J. R. Clausen, D. A. Reasor Jr., and C. K. Aidun. Parallel performance of a lattice-boltzmann/finite element cellular blood flow solver on the ibm blue gene/p architecture. Computer Physics Communications, 181(6):1013–1020, June 2010.

[30] J. R. Clausen, D. A. Reasor Jr., and C. K. Aidun. The rheology and microstructure of concentrated non-colloidal suspensions of deformable capsules. Journal of Fluid Mechanics, 685:202–234, September 2011.

[31] T. V. Colace and S. L. Diamond. Direct observation of von Willebrand factor elongation and fiber formation on collagen during acute whole blood exposure to pathological flow. Arteriosclerosis, thrombosis, and vascular biology, 33(1): 105–13, January 2013.

[32] G. Coupier, B. Kaoui, T. Podgorski, and C. Misbah. Noninertial lateral migration of vesicles in bounded poiseuille flow. Physics of Fluids, 20(11):111702, 2008.

[33] L. Crowl and A. L. Fogelson. Analysis of mechanisms for platelet near-wall excess under arterial blood flow conditions. Journal of Fluid Mechanics, 676: 348–375, April 2011.

[34] M. Dao, J. Li, and S. Suresh. Molecularly based analysis of deformation of spectrin network and human erythrocyte. Materials Science and Engineering: C, 26(8):1232–1244, September 2006.

[35] M. J. Davies and A. Thomas. Thrombosis and acute coronary-artery lesions in sudden cardiac ischemic death. The New England journal of medicine, 310(18): 1137–40, May 1984.

[36] M. J. Davies and A. C. Thomas. Review plaque fissuring–the cause of acute myocardial infarction , sudden ischaemic death , and crescendo angina. British heart journal, 53(4):363–73, April 1985.

[37] K. De Ceunynck, S. F. De Meyer, and K. Vanhoorelbeke. Unwinding the von Willebrand factor strings puzzle. Blood, 121(2):270–7, January 2013.

[38] E.-J. Ding and C. K. Aidun. The dynamics and scaling law for particles suspended in shear flow with inertia. Journal of Fluid Mechanics, 423:317–344, November 2000.

[39] E. C. Eckstein and F. Belgacem. Model of platelet transport in flowing blood with drift and diffusion terms. Biophysical Journal, 60(1):53–69, July 1991.

[40] E. C. Eckstein, D. G. Bailey, and A. H. Shapiro. Self-diffusion of particles in shear flow of a suspension. Journal of Fluid Mechanics, 79(1):191–208, April 1977.

[41] E. C. Eckstein, D. L. Bilsker, C. M. Waters, J. S. Kippenhan, and A. W. Tilles. Transport of platelets in flowing blood. Annals of the New York Academy of Sciences, 516:442–52, January 1987.

[42] E. C. Eckstein, A. W. Tilles, and F. J. Millero. Conditions for the occurrence of

large near-wall small excesses of small particles during blood flow. Microvascular research, 36:31–39, 1988.

[43] C. Escudero, M. Santos, J. Buján, et al. Optical aggregometry versus the PFA-100: experimental studies in pigs treated with propofol. Platelets, 12(3):133–7, May 2001.

[44] R. W. Farndale, J. J. Sixma, M. J. Barnes, and P. G. de Groot. The role of collagen in thrombosis and hemostasis. Journal of Thrombosis and Haemostasis, 2(4):561–573, April 2004.

[45] D. A. Fedosov. Multiscale Modeling of Blood Flow and Soft Matter. PhD thesis, Brown University, 2010.

[46] D. A. Fedosov, B. Caswell, and G. Karniadakis. A multiscale red blood cell model with accurate mechanics, rheology, and dynamics. Biophysical Journal, 98(10):2215–25, May 2010.

[47] D. A. Fedosov, B. Caswell, and G. E. Karniadakis. Systematic coarse-graining of spectrin-level red blood cell models. Computer Methods in Applied Mechanics and Engineering, 199(29-32):1937–1948, June 2010.

[48] D. A. Fedosov, B. Caswell, A. S. Popel, and G. E. Karniadakis. Blood flow and cell-free layer in microvessels. Microcirculation, 17(8):615–28, November 2010.

[49] H. H. Firrell and J. C. Lipowsky. Leukocyte margination and deformation in mesenteric venules of rat. American Journal of Physiology - Heart and Circulatory Physiology, 256(6):H1667–H1674, June 1989.

[50] J. B. Freund and M. M. Orescannin. Cellular flow in a small blood vessel. Journal of Fluid Mechanics, 671:466–490, February 2011.

[51] V. Fuster, J. Badimon, J. Chesebro, and J. Fallon. Plaque rupture, thrombosis, and therapeutic implications. Pathophysiology of Haemostasis and Thrombosis, 26(4):269–284, 1996.

[52] T. M. Geislinger, B. Eggart, S. Braunmüller, L. Schmid, and T. Franke. Separation of blood cells using hydrodynamic lift. Applied Physics Letters, 100(18): 183701, 2012.

[53] H. L. Goldsmith and J. C. Marlow. Flow behavior of erythrocytes. ii. particle motions in concentrated suspensions of ghost cells. Journal of Colloid and Interface Science, 71(2):383–407, 1979.

[54] H. L. Goldsmith and S. Spain. Margination of leukocytes in blood flow through small tubes. Microvascular Research, 27(2):204–222, March 1984.

[55] C. W. Hamm, J.-P. Bassand, S. Agewall, et al. Esc guidelines for the management of acute coronary syndromes in patients presenting without persistent st-segment elevation: The task force for the management of acute coronary syndromes (acs) in patients presenting without persistent st-segment elevatio. European heart journal, 32(23):2999–3054, December 2011.

[56] P. Harrison and E. Martin Cramer. Platelet α-granules. Blood Reviews, 7(1): 52–62, March 1993.

[57] K. Hosokawa, T. Ohnishi, T. Kondo, et al. A novel automated microchip flow-chamber system to quantitatively evaluate thrombus formation and antithrombotic agents under blood flow conditions. Journal of thrombosis and haemostasis, 9(10):2029–37, October 2011.

[58] H. W. Hou, A. A. S. Bhagat, A. G. L. Chong, et al. Deformability based cell margination–a simple microfluidic design for malaria-infected erythrocyte separation. Lab on a chip, 10(19):2605–13, October 2010.

[59] S. J. Hund and J. F. Antaki. An extended convection diffusion model for red blood cell-enhanced transport of thrombocytes and leukocytes. Physics in medicine and biology, 54(20):6415–35, October 2009.

[60] D. M. Husband, L. a. Mondy, E. Ganani, and a. L. Graham. Direct measurements of shear-induced particle migration in suspensions of bimodal spheres. Rheologica Acta, 33(3):185–192, 1994.

[61] A. Jordan, T. David, S. Homer-Vanniasinkam, A. Graham, and P. Walker. The effects of margination and red cell augmented platelet diffusivity on platelet adhesion in complex flow. Biorheology, 41(5):641–53, January 2004.

[62] M. V. Kameneva, Z. J. Wu, A. Uraysh, et al. Blood soluble drag-reducing polymers prevent lethality from hemorrhagic shock in acute animal experiments. Biorheology, 41(1):53–64, January 2004.

[63] S.-H. Kao. Platelet transport and surface reactions in mural thrombosis. PhD thesis, Rice University, 2000.

[64] K. H. Keller. Effect of fluid shear on mass transport in flowing blood. Federation proceedings, 30(5):1591–9, 1971.

[65] D. Kim and R. L. Beissinger. Augmented mass transport of macromolecules in sheared suspensions to surfaces. Journal of Colloid and Interface Science, 159 (1):9–20, August 1993.

[66] S. Kim, R. L. Kong, A. S. Popel, et al. Temporal and spatial variations of cell-free layer width in arterioles. American journal of physiology. Heart and circulatory physiology, 293(3):H1526–35, September 2007.

[67] S. Kim, P. K. Ong, O. Yalcin, M. Intaglietta, and P. C. Johnson. The cell-free layer in microvascular blood flow. Biorheology, 46(3):181–9, January 2009.

[68] G. P. Krishnan, S. Beimfohr, and D. T. Leighton. Shear-induced radial segregation in bidisperse suspensions. Journal of Fluid Mechanics, 321(-1):371, April 2006.

[69] D. Kroon and C. H. Slump. Coherence filtering to enhance the mandibular canal in cone-beam ct data. Annual Symposium of the IEEE-EMBS Benelux Chapter 2009, pages 41–44, 2009.

[70] D.-J. Kroon, C. H. Slump, and T. J. J. Maal. Diffusion scheme on cone-beam ct. pages 221–228, 2010.

[71] D. N. Ku and C. J. Flannery. Development of a flow-through system to create occluding thrombus. Biorheology, 44(4):273–84, January 2007.

[72] A. Kumar and M. D. Graham. Segregation by membrane rigidity in flowing binary suspensions of elastic capsules. Physical Review E, 84(6):066316, December 2011.

[73] A. Kumar and M. D. Graham. Margination and segregation in confined flows of blood and other multicomponent suspensions. Soft Matter, 8(41):10536, 2012.

[74] A. Kumar and M. D. Graham. Mechanism of margination in confined flows of blood and other multicomponent suspensions. Physical Review Letters, 109 (10):108102, September 2012.

[75] A. Kumar, R. G. Henríquez Rivera, and M. D. Graham. Flow-induced segregation in confined multicomponent suspensions: effects of particle size and rigidity. Journal of Fluid Mechanics, 738:423–462, December 2014.

[76] A. J. C. Ladd. Numerical simulations of particulate suspensions via a discretized boltzmann equation. part 2. numerical results. Journal of Fluid Mechanics, 271: 311–339, 1994.

[77] A. J. C. Ladd. Numerical simulations of particulate suspensions via a discretized boltzmann equation. part 1. theoretical foundation. Journal of Fluid Mechanics, 271:285–309, April 1994.

[78] H. Lei, D. A. Fedosov, B. Caswell, and G. E. Karniadakis. Blood flow in small tubes: quantifying the transition to the non-continuum regime. Journal of Fluid Mechanics, 722:214–239, March 2013.

[79] K. Leiderman and A. L. Fogelson. Grow with the flow: a spatial-temporal model of platelet deposition and blood coagulation under flow. Mathematical Medicine and Biology, 28(1):47–84, March 2011.

[80] D. Leighton and A. Acrivos. Viscous resuspension. Chemical Engineering Science, 41(6):1377–1384, January 1986.

[81] D. Leighton and A. Acrivos. The shear-induced migration of particles in concentrated suspensions. Journal of Fluid Mechanics, 181:415–439, April 1987.

[82] C. Leuser, S. Schlottmann, R. Siekmann, et al. Use of the platelet function analyser PFA-100™ in juvenile pigs. Comparative Clinical Pathology, 21(5): 761–767, January 2011.

[83] J. Li, M. Dao, C. T. Lim, and S. Suresh. Spectrin-level modeling of the cytoskeleton and optical tweezers stretching of the erythrocyte. Biophysical Journal, 88(5):3707–19, May 2005.

[84] M. Li. Microfluidic system for thrombosis under multiple shear rates and platelet therapies. PhD thesis, Georgia Institute of Technology, 2013.

[85] M. Li, D. N. Ku, and C. R. Forest. Microfluidic system for simultaneous optical measurement of platelet aggregation at multiple shear rates in whole blood. Lab on a chip, 12(7):1355–62, April 2012.

[86] M. Li, N. A. Hotaling, D. N. Ku, and C. R. Forest. Microfluidic thrombosis under multiple shear rates and antiplatelet therapy doses. PloS one, 9(1):e82493, January 2014.

[87] P. Libby and P. Theroux. Pathophysiology of coronary artery disease. Circulation, 111(25):3481–8, June 2005.

[88] J. Lidmar, L. Mirny, and D. Nelson. Virus shapes and buckling transitions in spherical shells. Physical Review E, 68(5):051910, November 2003.

[89] M. K. Lyon and L. G. Leal. An experimental study of the motion of concentrated suspensions in two-dimensional channel flow . part 2 . bidisperse systems. Journal of Fluid Mechanics, 363:57–77, 1998.

[90] R. M. MacMeccan, J. R. Clausen, G. P. Neitzel, and C. K. Aidun. Simulating deformable particle suspensions using a coupled lattice-boltzmann and finite-element method. Journal of Fluid Mechanics, 618:13–39, December 2009.

[91] J. F. Marko and E. D. Siggia. Stretching dna. Macromolecules, 28(26):8759–8770, December 1995.

[92] M. Mehrabadi, D. N. Ku, and C. K. Aidun. A continuum model for platelet transport in flowing blood based on direct numerical simulations of cellular blood flow. Annals of Biomedical Engineering, October 2014.

[93] H. Mohammadigoushki and J. J. Feng. Size-differentiated lateral migration of bubbles in couette flow of two-dimensional foam. Physical Review Letters, 109 (8):084502, August 2012.

[94] H. Mohammadigoushki and J. J. Feng. Size segregation in sheared two-dimensional polydisperse foam. Langmuir : the ACS journal of surfaces and colloids, 29(5):1370–8, February 2013.

[95] J. F. Morris. A review of microstructure in concentrated suspensions and its implications for rheology and bulk flow. Rheologica Acta, 48(8):909–923, March 2009.

[96] J. F. Morris and F. Boulay. Curvilinear flows of noncolloidal suspensions: The role of normal stresses. Journal of Rheology, 43(5):1213, 1999.

[97] K. Müller, D. a. Fedosov, and G. Gompper. Margination of micro- and nano-particles in blood flow and its effect on drug delivery. Scientific reports, 4:4871, January 2014.

[98] L. L. Munn and M. M. Dupin. Blood cell interactions and segregation in flow. Annals of biomedical engineering, 36(4):534–44, April 2008.

[99] M. Naghavi, P. Libby, E. Falk, et al. From vulnerable plaque to vulnerable patient: a call for new definitions and risk assessment strategies: Part i. Circulation, 108(14):1664–72, October 2003.

[100] K. Namdee, A. J. Thompson, P. Charoenphol, and O. Eniola-Adefeso. Margination propensity of vascular-targeted spheres from blood flow in a microfluidic model of human microvessels. Langmuir, 29(8):2530–5, February 2013.

[101] K. B. Neeves, A. a. Onasoga, R. R. Hansen, et al. Sources of variability in platelet accumulation on type 1 fibrillar collagen in microfluidic flow assays. PloS one, 8(1):e54680, January 2013.

[102] T. Nightingale and D. Cutler. The secretion of von Willebrand factor from endothelial cells; an increasingly complicated story. Journal of thrombosis and haemostasis, 11 Suppl 1:192–201, June 2013.

[103] P. R. Nott and J. F. Brady. Pressure-driven flow of suspensions: simulation and theory. Journal of Fluid Mechanics, 275:157–199, 1994.

[104] B. P. Nuyttens, T. Thijs, H. Deckmyn, and K. Broos. Platelet adhesion to collagen. Thrombosis Research, 127:S26–S29, January 2011.

[105] S. Ogawa, T. Ohnishi, K. Hosokawa, et al. Haemodilution-induced changes in coagulation and effects of haemostatic components under flow conditions. British journal of anaesthesia, 111(6):1013–23, December 2013.

[106] A. A. Palmer. Platelet and leucocyte skimming. In Fourth European Conference on Microcirculation, pages 300–303, Cambridge, England, 1966.

[107] M. A. Panteleev, N. M. Ananyeva, F. I. Ataullakhanov, and E. L. Saenko. Mathematical models of blood coagulation and platelet adhesion: clinical applications. Current Pharmaceutical Design, 13(14):1457–67, January 2007.

[108] A. Para, D. Bark, A. Lin, and D. Ku. Rapid platelet accumulation leading to thrombotic occlusion. Annals of biomedical engineering, 39(7):1961–71, July 2011.

[109] A. N. Para and D. N. Ku. A low-volume, single pass in-vitro system of high shear thrombosis in a stenosis. Thrombosis research, 131(5):418–24, May 2013.

[110] R. J. Phillips, R. C. Armstrong, R. a. Brown, A. L. Graham, and J. R. Abbott. A constitutive equation for concentrated suspensions that accounts for shear-induced particle migration. Physics of Fluids A: Fluid Dynamics, 4(1):30, 1992.

[111] I. V. Pivkin and G. E. Karniadakis. Accurate coarse-grained modeling of red blood cells. Physical Review Letters, 101(11):118105, September 2008.

[112] P. Pranay, R. G. Henríquez-Rivera, M. D. Graham, and R. G. Henriquez-Rivera. Depletion layer formation in suspensions of elastic capsules in newtonian and viscoelastic fluids. Physics of Fluids, 24(6):061902, 2012.

[113] D. A. Reasor Jr, J. R. Clausen, and C. K. Aidun. Coupling the lattice-boltzmann and spectrin-link methods for the direct numerical simulation of cellular blood flow. International Journal for Numerical Methods in Fluids, 68 (6):767–781, February 2012.

[114] D. A. Reasor Jr, J. R. Clausen, and C. K. Aidun. Rheological characterization of cellular blood in shear. Journal of Fluid Mechanics, 726:497–516, June 2013.

[115] D. A. Reasor Jr., M. Mehrabadi, D. N. Ku, and C. K. Aidun. Determination of critical parameters in platelet margination. Annals of biomedical engineering, 41(2):238–249, September 2013.

[116] W. Reinke, P. Gaehtgens, and P. C. Johnson. Blood viscosity in small tubes: effect of shear rate, aggregation, and sedimentation. American Journal of Physiology - Heart and Circulatory Physiology, 253(3):H540–H547, 1987.

[117] J. W. Rowley, A. V. Finn, P. a. French, et al. Cardiovascular devices and platelet interactions: understanding the role of injury, flow, and cellular responses. Circulation. Cardiovascular interventions, 5(2):296–304, April 2012.

[118] Z. M. Ruggeri. The role of von Willebrand factor in thrombus formation. Thromb Research, 120 Suppl:S5–9, January 2007.

[119] Z. M. Ruggeri. Platelet adhesion under flow. Microcirculation, 16(1):58–83, January 2009.

[120] Z. M. Ruggeri and S. P. Jackson. Platelet thrombus formation in flowing blood. In A. D. Michelson, editor, Platelets. 2013.

[121] Z. M. Ruggeri and G. L. Mendolicchio. Adhesion mechanisms in platelet function. Circulation research, 100(12):1673–85, June 2007.

[122] M. Saadatmand, T. Ishikawa, N. Matsuki, et al. Fluid particle diffusion through high-hematocrit blood flow within a capillary tube. Journal of biomechanics, 44(1):170–5, January 2011.

[123] B. Savage, F. Almus-Jacobs, and Z. M. Ruggeri. Specific synergy of multiple substrate-receptor interactions in platelet thrombus formation under flow. Cell, 94(5):657–66, September 1998.

[124] S. W. Schneider, S. Nuschele, A. Wixforth, et al. Shear-induced unfolding triggers adhesion of von Willebrand factor fibers. Proceedings of the National Academy of Sciences of the United States of America, 104(19):7899–903, May 2007.

[125] D. Semwogerere and E. R. Weeks. Shear-induced particle migration in binary colloidal suspensions. Physics of Fluids, 20(4):043306, 2008.

[126] M. Sharan and A. S. Popel. A two-phase model for flow of blood in narrow tubes with increased effective viscosity near the wall. Biorheology, 38(5-6): 415–28, January 2001.

[127] D. C. Sheehan and B. B. Hrapchak. Theory and practice of histotechnology. Mosby, St. Louis, second edi edition, 1980.

[128] S. S. Shevkoplyas, T. Yoshida, L. L. Munn, and M. W. Bitensky. Biomimetic autoseparation of leukocytes from whole blood in a microfluidic device. Analytical chemistry, 77(3):933–7, February 2005.

[129] J. Shin, J. E. Edelberg, and M. K. Hong. Vulnerable atherosclerotic plaque: clinical implications. Current vascular pharmacology, 1(2):183–204, June 2003.

[130] Siemens. PFA-100 ® system: Getting started guide, 2008.

[131] A. Sierou and J. F. Brady. Shear-induced self-diffusion in non-colloidal suspensions. Journal of Fluid Mechanics, 506(April 2004):285–314, May 2004.

[132] J. J. Sixma, G. H. van Zanten, E. G. Huizinga, et al. Platelet adhesion to collagen: an update. Thrombosis and haemostasis, 78(1):434–8, July 1997.

[133] E. N. Sorensen, G. W. Burgreen, W. R. Wagner, and J. F. Antaki. Computational simulation of platelet deposition and activation: I. model development and properties. Annals of biomedical engineering, 27(4):436–48, 1999.

[134] J. J. Stickel and R. L. Powell. Fluid mechanics and rheology of dense suspensions. Annual Review of Fluid Mechanics, 37(1):129–149, January 2005.

[135] A. B. Strong, G. D. Stubley, G. Chang, and D. R. Absolom. Theoretical and experimental analysis of cellular adhesion to polymer surfaces. Journal of biomedical materials research, 21(8):1039–55, August 1987.

[136] S. Succi. The Lattice Boltzmann Equation for Fluid Dynamics and Beyond. Oxford University Press, Oxford, 2001.

[137] Y. Suzuki, N. Tateishi, M. Soutani, and N. Maeda. Deformation of erythrocytes in microvessels and glass capillaries: Effects of erythrocyte deformability. Microcirculation, 3(1):49–57, January 1996.

[138] J. Tan, A. Thomas, and Y. Liu. Influence of red blood cells on nanoparticle targeted delivery in microcirculation. Soft matter, 8:1934–1946, December 2012.

[139] M. H.-Y. Tan, D.-V. Le, and K.-H. Chiam. Hydrodynamic diffusion of a suspension of elastic capsules in bounded simple shear flow. Soft Matter, 8(7): 2243–2251, 2012.

[140] T. Tanaka, T. Ishikawa, K. Numayama-Tsuruta, et al. Inertial migration of

cancer cells in blood flow in microchannels. Biomedical microdevices, September 2011.

[141] G. J. Tangelder, D. W. Slaaf, H. C. Tierlinck, R. Alewijnse, and R. S. Reneman. Localization within a thin optical section of fluorescent blood platelets flowing in a microvessel. Microvascular research, 23(2):214–30, March 1982.

[142] G. J. Tangelder, H. C. Teirlinck, D. W. Slaaf, and R. S. Reneman. Distribution of blood platelets flowing in arterioles. American Journal of Physiology - Heart and Circulatory Physiology, 248(3):H318–H323, March 1985.

[143] C. A. Taylor and J. D. Humphrey. Open problems in computational vascular biomechanics: Hemodynamics and arterial wall mechanics. Computer methods in applied mechanics and engineering, 198(45-46):3514–3523, September 2009.

[144] A. J. Thompson, E. M. Mastria, and O. Eniola-Adefeso. The margination propensity of ellipsoidal micro/nanoparticles to the endothelium in human blood flow. Biomaterials, 34(23):5863–71, July 2013.

[145] A. W. Tilles and E. C. Eckstein. The near-wall excess of platelet-sized particles in blood flow: its dependence on hematocrit and wall shear rate. Microvascular research, 33(2):211–23, March 1987.

[146] K. Tomokiyo, Y. Kamikubo, T. Hanada, et al. Von Willebrand factor accelerates platelet adhesion and thrombus formation on a collagen surface in platelet-reduced blood under flow conditions. Blood, 105(3):1078–84, February 2005.

[147] V. T. Turitto and H. R. Baumgartner. Platelet interaction with subendothelium in a perfusion system: Physical role of red blood cells. Microvascular Research, 9(3):335–344, May 1975.

[148] V. T. Turitto and H. J. Weiss. Red blood cells: their dual role in thrombus formation. Science, 207(4430):541–543, 1980.

[149] V. T. Turitto and H. J. Weiss. Platelet and red cell involvement in mural thrombogensis. Annals of the New York Academy of Sciences, 416:363–376, December 1983.

[150] V. T. Turitto, H. J. Weiss, and H. R. Baumgartner. The effect of shear rate on platelet interaction with subendothelium exposed to citrated human blood. Microvascular Research, 19(3):352–365, May 1980.

[151] K. Vahidkhah, S. L. Diamond, and P. Bagchi. Platelet dynamics in three-dimensional simulation of whole blood. Biophysical Journal, 106(11):2529–2540, June 2014.

[152] R. Virmani, A. P. Burke, A. Farb, and F. D. Kolodgie. Pathology of the vulnerable plaque. Journal of the American College of Cardiology, 47(8 Suppl): C13–8, April 2006.

[153] J. C. Wang, S.-L. T. Normand, L. Mauri, and R. E. Kuntz. Coronary artery spatial distribution of acute myocardial infarction occlusions. Circulation, 110 (3):278–84, July 2004.

[154] N.-H. L. Wang and K. Keller. Augmented transport of extracellular solutes in concentrated erythrocyte suspensions in couette flow. Journal of Colloid and Interface Science, 103(1):210–225, January 1985.

[155] W. Wang and M. R. King. Multiscale modeling of platelet adhesion and thrombus growth. Annals of biomedical engineering, 40(11):2345–54, November 2012.

[156] C. M. Waters and E. C. Eckstein. Concentration profiles of platelet-sized latex

beads for conditions relevant to hollow-fiber hemodialyzers. Artificial Organs, 14(1):7–13, 1990.

[157] E. R. Weibel. New cytoplasmic components in arterial endothelia. The Journal of Cell Biology, 23(1):101–112, October 1964.

[158] P. J. Wellings and D. N. Ku. Mechanisms of platelet capture under very high shear. Cardiovascular Engineering and Technology, 3(2):161–170, March 2012.

[159] U. Windberger, A. Bartholovitsch, R. Plasenzotti, K. J. Korak, and G. Heinze. Whole blood viscosity , plasma viscosity and erythrocyte aggregation in nine mammalian species : reference values and comparison of data. Experimental Physiology, 88(3):431–440, May 2003.

[160] B. Woldhuis, G. J. Tangelder, D. W. Slaaf, and R. S. Reneman. Concentration profile of blood platelets differs in arterioles and venules. American Journal of Physiology - Heart and Circulatory Physiology, 262(4):H1217–23, April 1992.

[161] B. Woldhuis, G. J. Tangelder, D. W. Slaaf, and R. S. Reneman. Influence of dextrans on platelet distribution in arterioles and venules. Pflügers Archiv, 425 (3-4):191–198, November 1993.

[162] D. M. Wootton and D. N. Ku. Fluid mechanics of vascular systems, diseases, and thrombosis. Annual review of biomedical engineering, 1:299–329, January 1999.

[163] D. M. Wootton, C. P. Markou, S. R. Hanson, and D. N. Ku. A mechanistic model of acute platelet accumulation in thrombogenic stenoses. Annals of Biomedical Engineering, 29(4):321–329, April 2001.

[164] C. Xu and D. M. Wootton. Platelet near-wall excess in porcine whole blood in

artery-sized tubes under steady and pulsatile flow conditions. Biorheology, 41 (2):113–25, January 2004.

[165] C. Xu and D. M. Wootton. Platelet near-wall excess in porcine whole blood in artery-sized tubes under steady and pulsatile flow conditions. Biorheology, 41 (2):113–25, January 2004.

[166] Z. Xu, M. Kamocka, M. Alber, and E. D. Rosen. Computational approaches to studying thrombus development. Arteriosclerosis, Thrombosis, and Vascular Biology, 31(3):500–505, March 2011.

[167] S. Yamaguchi, T. Yamakawa, and H. Niimi. Cell-free plasma layer in cerebral microvessels. Biorheology, 29(2-3):251, 1992.

[168] C. Yeh and E. C. Eckstein. Transient lateral transport of platelet-sized particles in flowing blood suspensions. Biophysical Journal, 66(5):1706–16, May 1994.

[169] C. Yeh, A. C. Calvez, and E. C. Eckstein. An estimated shape function for drift in a platelet-transport model. Biophysical journal, 67(3):1252–9, September 1994.

[170] K. Yeo and M. R. Maxey. Anomalous diffusion of wall-bounded non-colloidal suspensions in a steady shear flow. Europhysics Letters, 92(2):24008, October 2010.

[171] H. Zhao and E. S. G. Shaqfeh. Shear-induced platelet margination in a microchannel. Physical Review E, 83(6):061924, June 2011.

[172] H. Zhao, E. S. G. Shaqfeh, and V. Narsimhan. Shear-induced particle migration and margination in a cellular suspension. Physics of Fluids, 24(1):011902, 2012.

[173] R. Zhao, M. V. Kameneva, and J. F. Antaki. Investigation of platelet margination phenomena at elevated shear stress. Biorheology, 44(3):161–77, January 2007.

[174] R. Zhao, M. V. Kameneva, and J. F. Antaki. Investigation of platelet margination phenomena at elevated shear stress. Biorheology, 44(3):161–77, 2007.

[175] A. L. Zydney and C. K. Colton. Augmented solute transport in the shear flow of a concentrated suspension. Physicochemical hydrodynamics, 10(1):77–96, 1988.